
Supplementary information

Quantum-size-tuned heterostructures enable efficient and stable inverted perovskite solar cells

In the format provided by the
authors and unedited

¹ Supplementary materials for
² Quantum-size-tuned heterostructures enable efficient
³ and stable inverted perovskite solar cells

⁴ *Hao Chen,^{1,2,†} Sam Teale,^{1,†} Bin Chen,^{1,†} Yi Hou,^{1,4,†} Luke Grater,¹ Tong Zhu,¹ Koen
⁵ Bertens,¹ So Min Park,^{1,3} Harindi R. Atapattu,³ Yajun Gao,⁶ Mingyang Wei,¹ Andrew K.
⁶ Johnston,¹ Qilin Zhou,² Kaimin Xu,² Danni Yu,² Congcong Han,² Teng Cui,⁵ Eui Hyuk Jung,¹
⁷ Chun Zhou,¹ Wenjia Zhou,² Andrew H. Proppe,¹ Sjoerd Hoogland,¹ Frédéric Laquai,⁶ Tobin
⁸ Filleter,⁵ Kenneth R. Graham,³ Zhijun Ning,^{2*} Edward H. Sargent^{1*}*

⁹ ¹ The Edward S. Rogers Department of Electrical and Computer Engineering, University of Toronto,
¹⁰ Toronto, Ontario, Canada, M5S 3G4

¹¹ ² School of Physical Science and Technology, Shanghai Tech University, Shanghai 201210, China

¹² ³ Department of Chemistry, University of Kentucky, Lexington, Kentucky 40506, United States

¹³ ⁴ Present address: Department of Chemical and Biomolecular Engineering, National University of
¹⁴ Singapore, 4 Engineering Drive 4, 117585 Singapore

¹⁵ ⁵ Department of Mechanical and Industrial Engineering, 5 King's College Road, Toronto, ON M5S
¹⁶ 3G8, Canada

¹⁷ ⁶ KAUST Solar Center, Physical Sciences and Engineering Division (PSE), Materials Science and
¹⁸ Engineering Program (MSE), King Abdullah University of Science and Technology (KAUST),
¹⁹ Thuwal, Kingdom of Saudi Arabia

²⁰

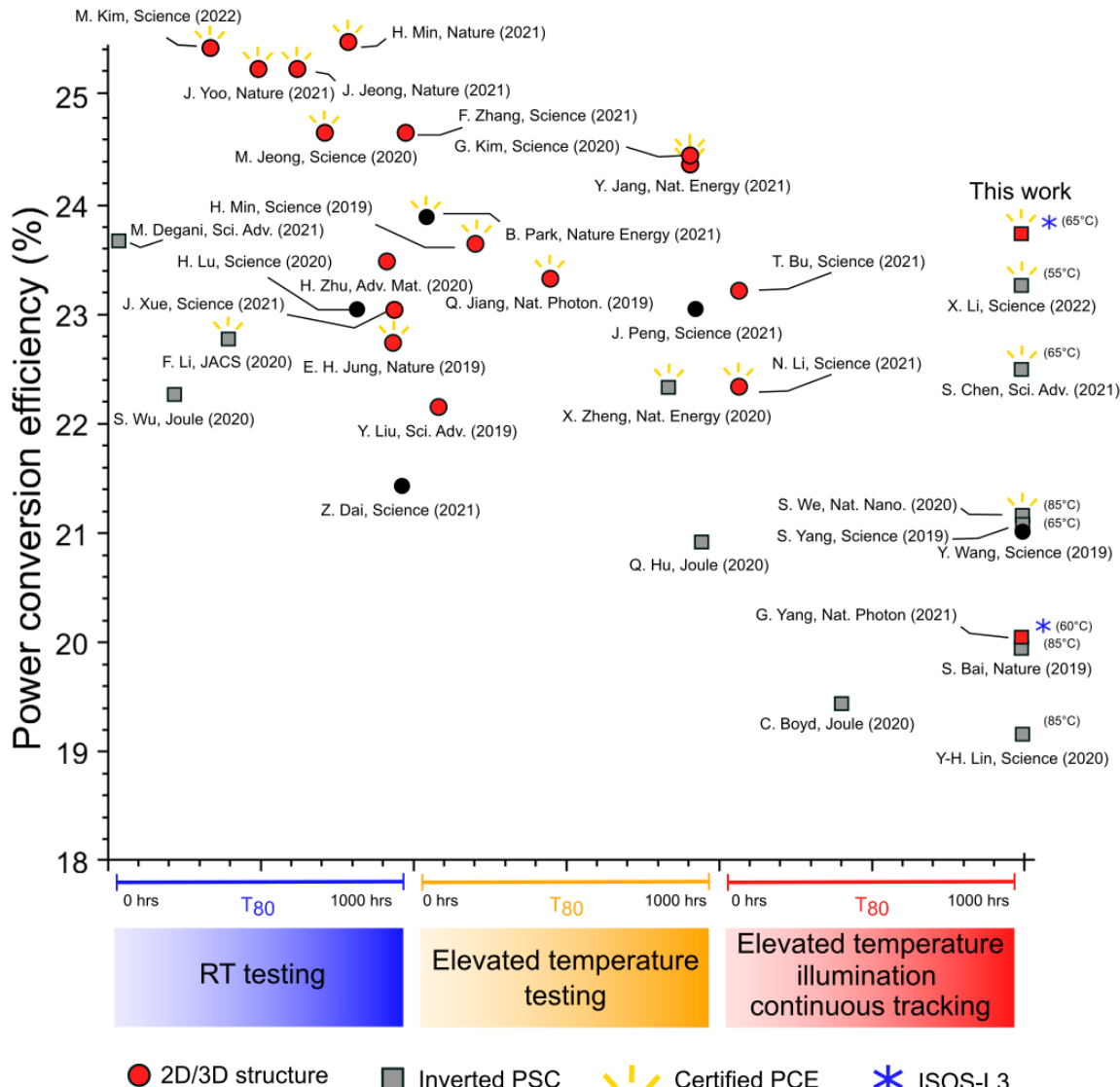
²¹ *Correspondence to: ted.sargent@utoronto.ca, ningzhj@shanghaitech.edu.cn

²²

²³ †These authors contributed equally

24

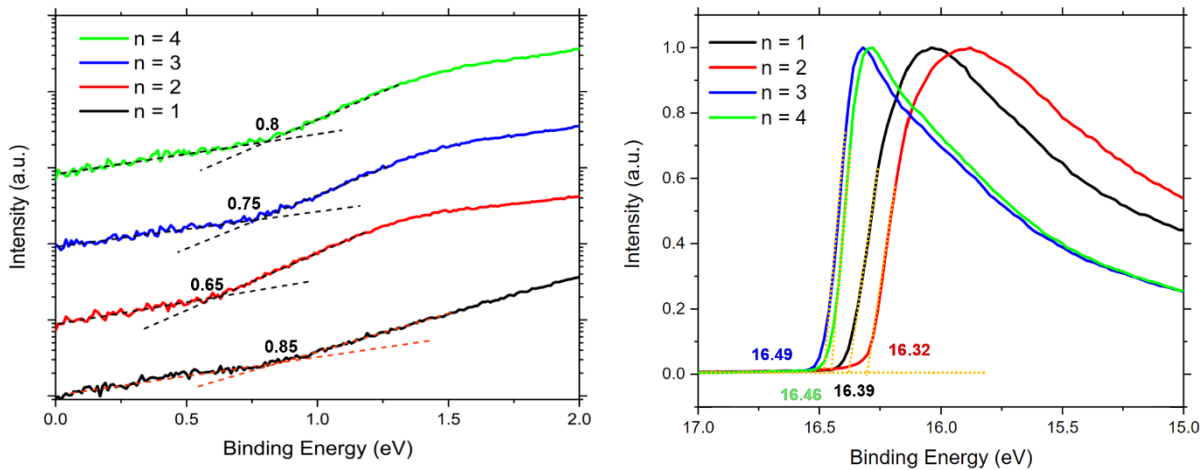
25



26

27 **Figure S1 | Summary of PSC efficiency/stability** A comparison of device efficiency and stability from
 28 many high-profile perovskite solar cell papers from 2019 onwards. This summary demonstrates that the
 29 majority of high performing NIP PSCs use a 2D/3D heterostructure. It also showcases the stability
 30 advantages of PIN solar cells. In this work we sought to use both of these for excellent stability and
 31 efficiency. All references can be found in Table 7.

32



33 **Figure S2 | UPS spectra for $\langle n \rangle = 1, 2, 3$ and 4 films.** Films were fabricated by spin coating precursor
34 ratios of $\text{PEA}_2\text{MA}_{n-1}\text{Pb}_n\text{I}_{3n+1}$

35

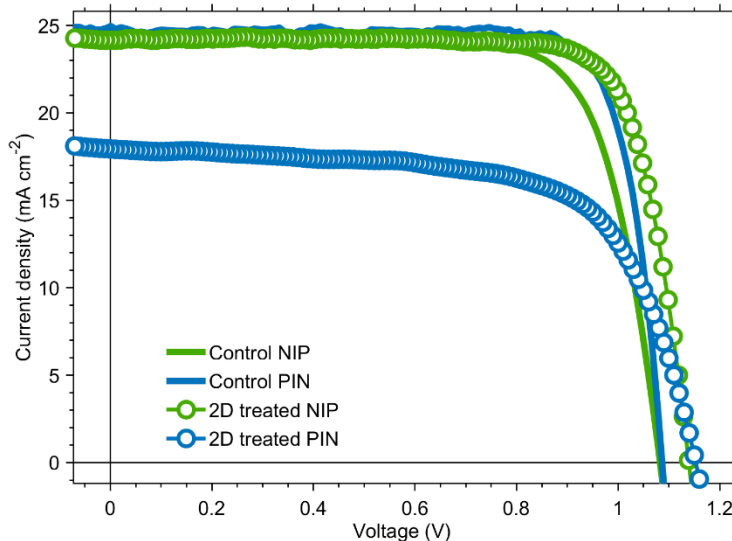
	WF	VB	CB	Optical Bandgap (eV)
$n = 1$	4.81	5.61	3.23	2.38
$n = 2$	4.88	5.53	3.37	2.16
$n = 3$	4.71	5.46	3.44	2.02
$n = 4$	4.74	5.54	3.63	1.91

36
37 **Table S1 | Calculated band alignment values** from a linear fitting of Fig. S2a (semi-log plot) and
38 Fig. S2b (linear plot). These values were combined with the optical bandgap found from TA spectra
39 to calculate the band alignment of $\langle n \rangle = 1, 2, 3$ and 4 films.

40

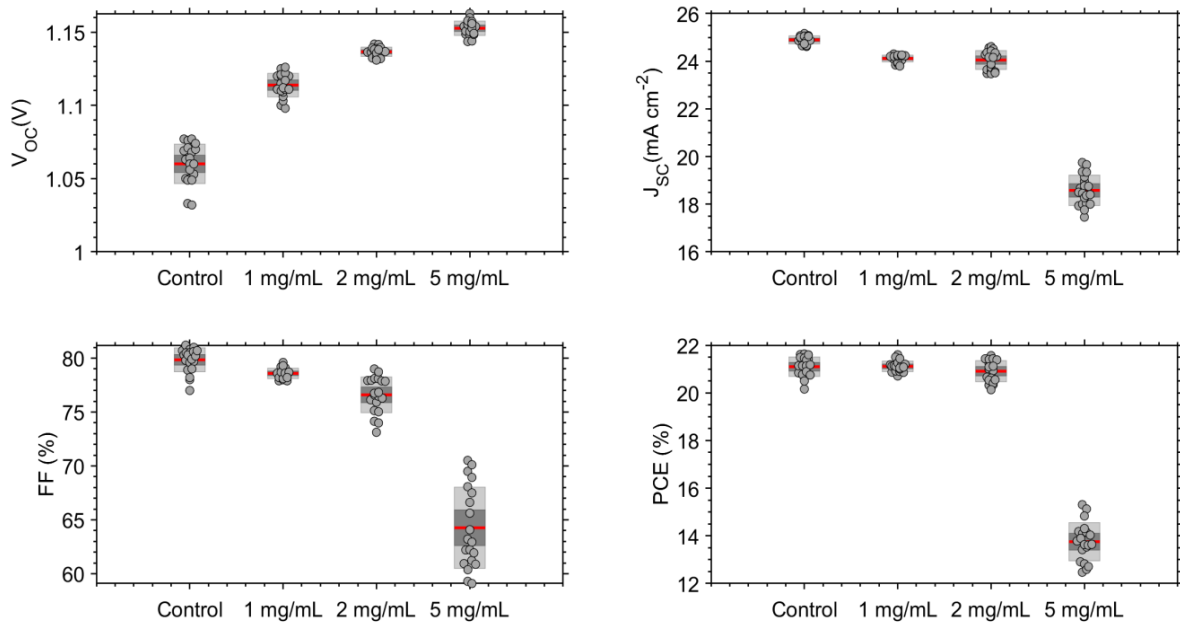
41 **Supplementary Text 1 | Reduced performance of the standard 2D treatment in PIN**

42 As mentioned in the main manuscript, it has been reported that standard 2D treatments do not produce
43 improved performance in PIN devices as they do in NIP. We confirmed this ourselves by fabricating
44 PIN (NiO_x /3D-perovskite/2D/ C_{60} /ALD-SnO₂/Ag) and NIP (SnO_2 /3D-perovskite/2D/Spiro-
45 OMeTAD/Au) devices. The resultant current-voltage (J - V) curves (Fig. S3) show improved open circuit
46 voltage (V_{OC}) for both architectures, indicating well-passivated surfaces.^{1,2} Despite both devices using
47 the same 5 mg/mL PEAi in isopropanol (IPA) surface treatment, the inverted devices have reduced
48 short circuit current (J_{SC}) and fill factor (FF), indicating a transport barrier within the cell. Reducing
49 the concentration of PEAi does curtail losses; but the treatment does not dramatically improve
50 performance compared to controls as it does for NIP solar cells (Fig. S4).



51 **Figure S3 | J-V curves from PIN and NIP devices** using a 5 mg mL⁻¹L PEAi 2D treatment. The NIP
52 device is improved by the treatment, the PIN device is significantly inhibited, with losses in current
53 and fill factor.

54



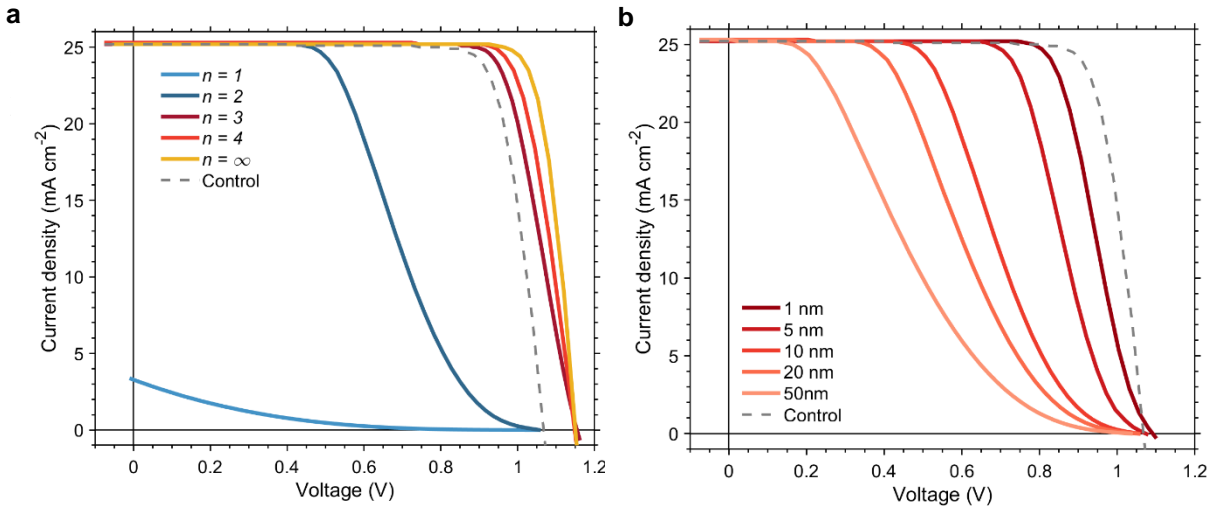
55
56
57 **Figure S4 | Performance statistics for Control films and films treated with 1, 2 and 5 mg mL⁻¹**
58 **PEAI in IPA solutions.** 20 Devices of each type were fabricated and tested for statistical analysis.
59

60 **Supplementary Text 2 | Simulations of 2D/3D heterojunctions in PIN**

61 Using the band alignment calculated from quasi-2D films, we simulated inverted devices with 10 nm n
 62 = 1, 2, 3 or 4 2D interlayers in SCAPS-1D (Fig. S5a).³ When we assumed that passivated surfaces see
 63 a reduction in defect density,^{1,4} we found that devices with a $n = 1$ interlayer suffered from significant
 64 losses to J_{SC} and FF , devices with $n = 2$ suffered losses to FF , and devices utilising $n > 2$ were improved
 65 compared to controls. We also found that efficiency is dependent on interlayer thickness with thinner
 66 layers demonstrating improved FF (Fig. S5b), this may explain the reasonable performance of 1 mg
 67 mL⁻¹ 2D treated devices (higher V_{OC} but slightly lower FF and J_{SC} than controls). A comprehensive
 68 breakdown of the simulation parameters and justification for their use is found below.

69

70



71

72 **Figure S5 | Simulated J-V curves.** Curves simulated using (a) 10 nm thick perovskite layer between
 73 perovskite and ETL with the band alignment calculated in Table 1 for each n value. The $n = \infty$
 74 simulation (added to give an idea of the ideal case) corresponds to a version of the cell in which the
 75 2D layer has the same exactly band alignment as the 3D (b) varying thickness of $n = 2$ perovskite.
 76 Clearly both the quasi-2D interlayer species and thickness are important factors. Parameters for
 77 simulation were taken from band alignment in Table 2. Other physical properties for 3D perovskite
 78 and RDPs used the same value. Full simulation parameters can be found in Table 4.

79

80

81

Parameter	Material			
	SnO_2	2D perovskite	3D perovskite	NiO_x
Thickness (nm)	50	1-20	600	50
Bandgap (eV)	3.9 ⁵	2.38 – 1.91	1.55	3 ⁶
Electron Affinity (eV)	4.2 ⁵	3.23 – 3.63	3.9 ⁷	2.2 ⁶
Dielectric permittivity (relative)	7.1 ⁸	24.1	24.1 ⁹	11.9 ¹⁰
Conduction band effective density of states (cm⁻³)	2.2E18 ¹¹	7.9E17	7.9E17 ¹²	2.5E18 ¹³
Valence band effective density of states (cm⁻³)	1E18	1E18	1E18 ¹²	1.8E18 ¹³
Electron mobility (cm²/Vs)	2.4E2 ¹⁴	2.2E0	2.2E1 ¹⁵	1E-3
Hole mobility (cm²/Vs)	1E2	2.2E0	2.2E1	1E-3
Shallow uniform acceptor density, N_A (cm⁻³)	0	1E15	1E15	1E19 ¹⁶
Shallow uniform donor density, N_A (cm⁻³)	1E21 ¹⁷	0	0	0
Defect type	-	Neutral	Neutral	Neutral
Capture cross section (electrons) (cm⁻³)	-	1E-13	1E-13	1E-15
Capture cross section (holes) (cm⁻³)	-	1E-13	1E-13	1E-15
Energetic distribution	-	Single	Single	Single
Energy level (eV)	-	0.5	0.5	0.5
Total defect density (cm⁻³)	-	1E14	1E14	1E14

89

90 Table S2 | Material parameters used for simulation in SCAPS-1D

91

92 **Discussion of simulation parameters**

93 **Thickness:** Thicknesses were chosen to reflect our device architecture

94 **Bandgap:** The bandgaps of SnO_2 and NiO_x were taken from ⁵ and ⁶ respectively. The bandgaps of 3D
95 and 2D perovskites were taken from our photo-electron spectroscopy results (Table S1 and S2
96 respectively).

97 **Electron affinity:** The electron affinities of SnO_2 and NiO_x were taken from ⁵ and ⁶ respectively. The
98 electron affinities of different 2D perovskite species were taken from our photo-electron spectroscopy
99 results (Table S2). For 3D perovskite, we used the same value used in similar simulations in ¹,
100 referenced from ⁷ which is almost identical to the value derived from photo-electron measurements
101 (Table S1).

102 **Dielectric permittivity:** The dielectric permittivity of SnO_2 , 3D perovskite and NiO_x were taken
103 from ⁸⁻¹⁰ respectively. 2D perovskite was taken to be the same as 3D perovskite due to a lack reliable
104 literature. The same assumption was made when simulating solar cells in ¹, and a similar value for 2D
105 perovskite was used in SCAPS simulations in ¹⁸.

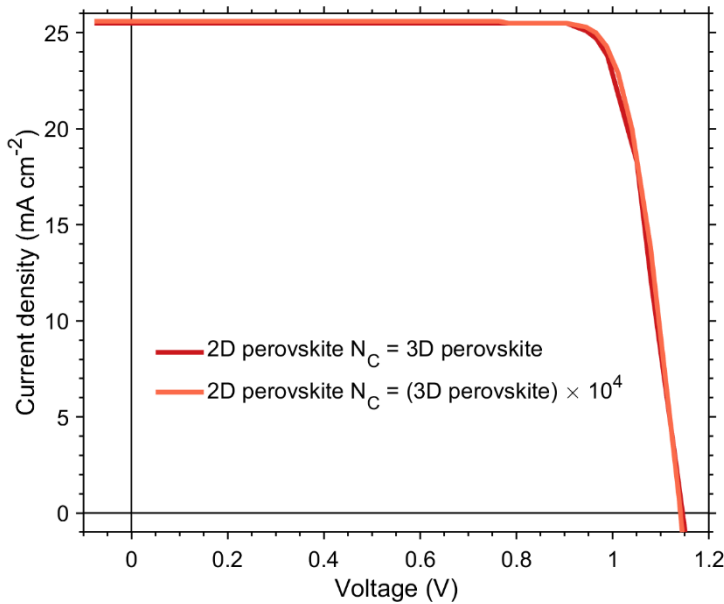
106 **Conduction/valence band effective density of states:** The effective density of states for the
107 conduction and valence bands (N_C and N_V respectively) were calculated using standard equations:

$$108 \quad N_C = 2 \left(\frac{2\pi m_e^* k T}{h^2} \right)^{\frac{3}{2}}$$

$$109 \quad N_V = 2 \left(\frac{2\pi m_h^* k T}{h^2} \right)^{\frac{3}{2}}$$

110 where k is Boltzmann's constant, T is temperature and h is Planck's constant. The effective masses of
111 electrons and holes (m_e^* and m_h^* respectively) were found in the literature. For SnO_2 , the value for
112 electrons was taken from ¹¹ and for holes it was assumed to be the same as the absorber, an
113 assumption used previously in ¹⁹. For perovskite, values from ¹² were used. For NiO_x , values from ¹³
114 were used. For 2D materials these equations are no longer valid. However, previous SCAPS

115 simulations of RDPs have used the same N_C and N_V as 3D perovskite;^{1,20} we do the same here. The
116 justification for this approximation is that increasing the N_C by several orders of magnitude makes
117 little difference to simulation results (Fig. S6).



118

119 **Figure S6 | Simulated J-V curves comparing the conduction band effective density of states in**
120 **the quasi-2D perovskite layer.** Curves simulated using 10 nm thick quasi-2D layer using the band
121 alignment from Table S1.

122 **Electron/hole mobilities:** Mobilities for NiO_x are the same as used for the HTL layers in¹⁹. The
123 electron mobility of SnO_2 is taken from¹⁴, the lower hole mobility is used for convenience.
124 Mobilities for 3D perovskite are taken from¹⁵. For 2D perovskite this is reduced by an order of
125 magnitude as RDPs are known to have lower mobilities than their bulk counterparts.

126 **Donor/acceptor densities:** Our UPS results suggest that 3D and 2D perovskite are both lightly p-type
127 so have a low acceptor concentration of $1\text{E}15 \text{ cm}^{-3}$. The hole concentration of NiO_x was taken from¹⁶.
128 The electron concentration of SnO_2 was taken from¹⁴.

129 **Bulk defects:** Parameters concerning bulk defects were generated using the SCAPS standard settings
130 which reflect real-world materials.³

Parameter	Interface			
	SnO ₂ / 2D perovskite	2D perovskite/ 3D perovskite	3D perovskite/ NiO _x	SnO ₂ / 3D Perovskite
Defect type	Neutral	Neutral	Neutral	Neutral
Capture cross section (electrons) (cm ⁻³)	1E-16	1E-16	1E-16	1E-16
Capture cross section (holes) (cm ⁻³)	1E-16	1E-16	1E-16	1E-16
Energetic distribution	Single	Single	Single	Single
Energy level (eV)	0.5	0.5	0.5	0.5
Total defect density (cm ⁻²)	1E14	10E14	1E13	1E16

131

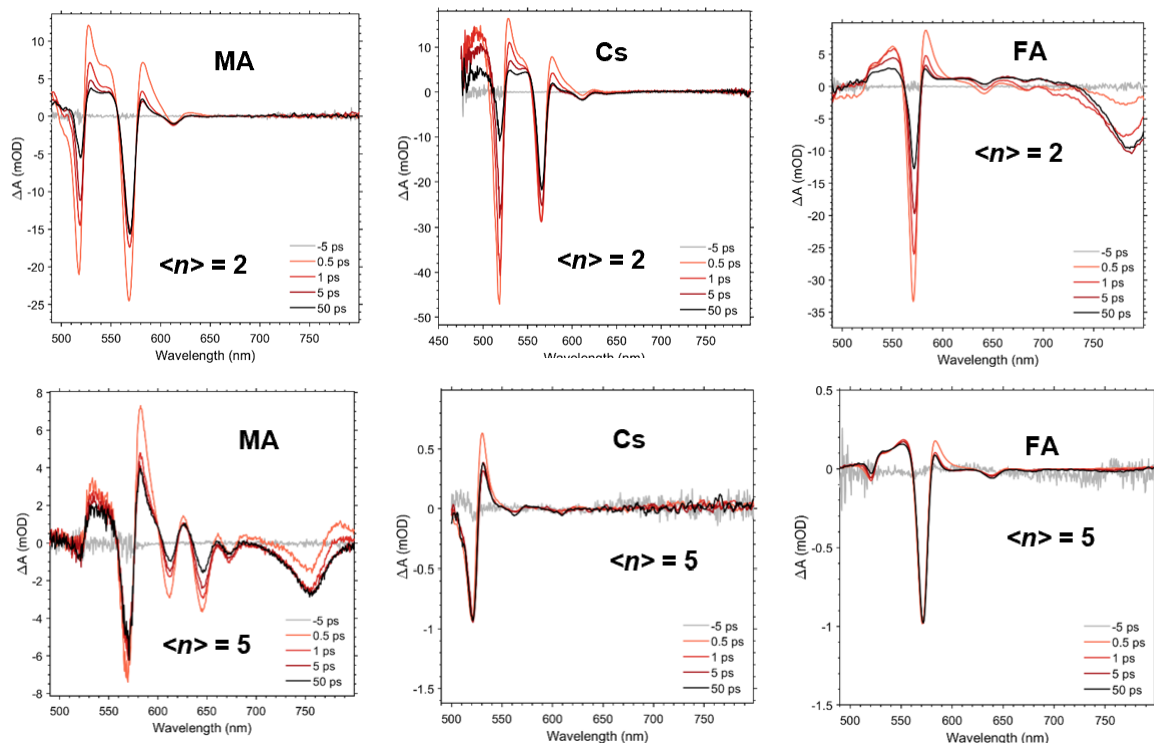
132 **Table S3 | Interface parameters** used for simulation in SCAPS-1D

133 **Interface defects:** Parameters concerning defects were generated using the SCAPS standard settings
 134 which reflect real-world materials. The total defect density (cm⁻³) for the perovskite/ETL interface
 135 was increased from the 1E10 generated by SCAPS to 1E+16 based on ⁴. This was reduced to 1E14
 136 based on results from well passivated surfaces in the same paper. For the perovskite HTL interface
 137 1E13 was used, again using values from ⁴.

138

139 **Supplementary Text 3 | Designing quasi-2D heterostructures**

140 As mentioned in the main manuscript, several avenues were explored towards producing 2D/3D
 141 heterostructures containing wider QWs ($n \geq 3$). At first, we attempted to add 3D perovskite components
 142 directly into the 2D ligands solution, but this was not possible, due to low solubility of PbI_2 in commonly
 143 used solvents (IPA, CF, Butanol). Bulk RDP films were prepared from stoichiometric precursors
 144 containing 2D perovskite ligands, PbI_2 and common 3D perovskite cations (MA, FA or Cs), and found
 145 that only bulk RDP films using MA produced large amounts of $n \geq 3$ RDPs (Fig. S7).



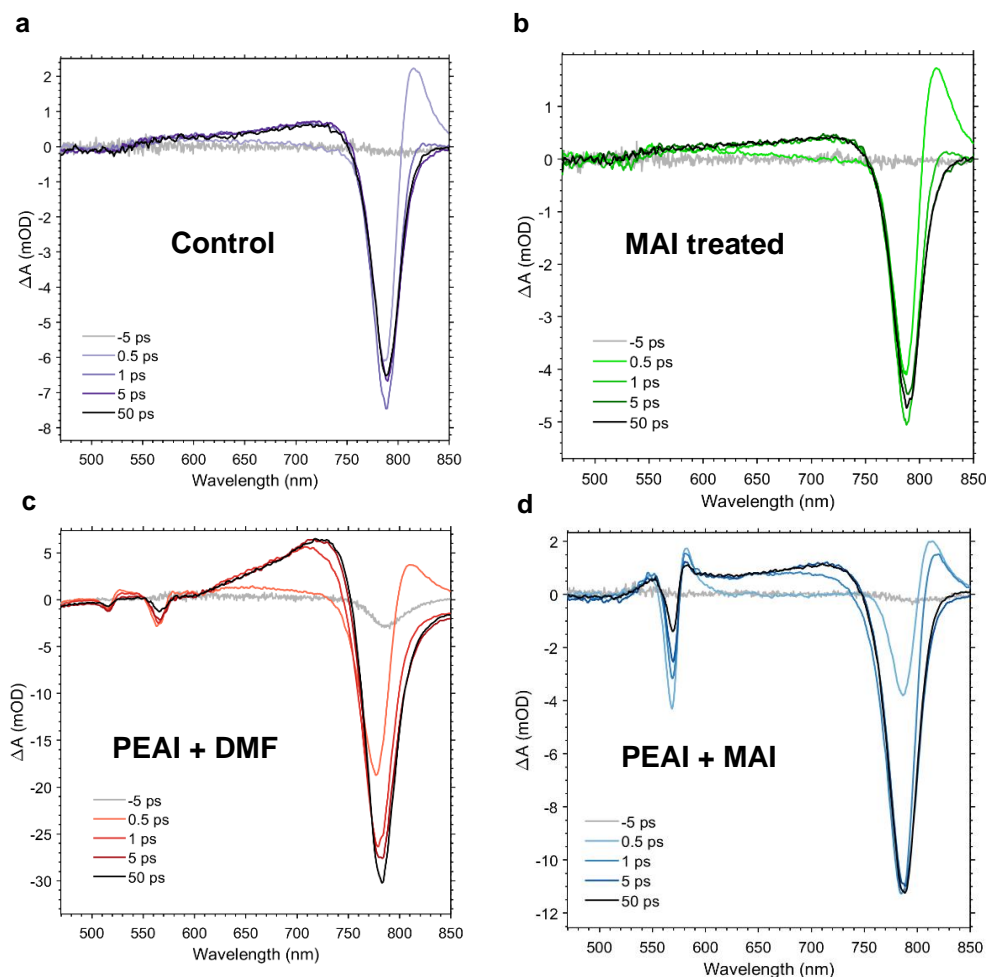
146 **Figure S7 |** Transient absorption spectra of films of $<\!n\!> = 2$ and $<\!n\!> = 5$ RDP where the additional A-
 147 site cation is either MA, Cs or FA. We used peaks from these spectra to extract the absorption
 148 wavelengths in Table S4. Note that for $<\!n\!> = 5$ FA and Cs based quasi-2D perovskites there is little
 149 absorption from the $n > 2$, this could be due to the phase instability of FAPbI_3 and CsPbI_3 .

150

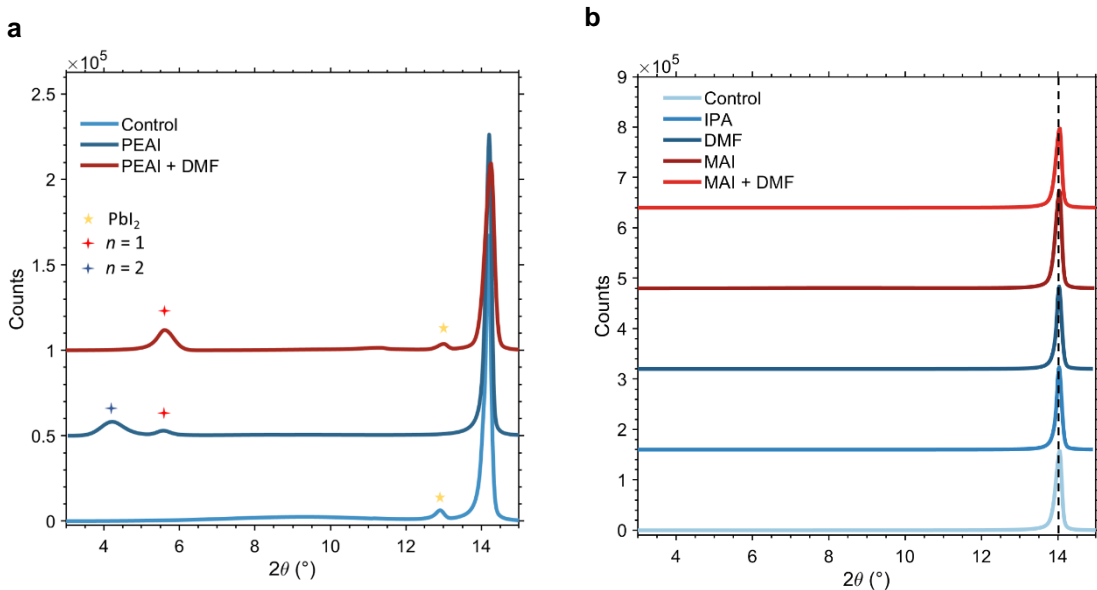
151 Using MAI as a sole additive with PEAI in our 2D treatment reduced the formation of $n = 1$ in 2D
 152 treated films but did not produce $n \geq 3$ (Fig. S8d). Only when DMF was added to this treatment did we
 153 produce wider RDPs. When using PEAI and DMF (no MAI in the IPA solution) we found no obvious
 154 change in the TA signal compared to using PEAI alone (Fig. S8). However, XRD suggested that more
 155 PbI_2 was formed using this treatment (Fig. S9a), hence we used a very small amount of DMF (1:200 by

156 vol. to IPA) to ensure that we did not dissolve large amounts of 3D perovskite, as this would not be
157 beneficial to devices. We also used XRD to check the effect of using any combination of MAI/DMF to
158 treat the perovskite surface, with no obvious changes (Fig. S9b).

159 We thought to vary the MAI content to induce wider RDPs to grow, but found that this induced disorder
160 into the heterostructure with a broadening of existing peaks rather than the formation of wider RDPs
161 (Fig S10). Ultimately, we found that using DMF (1:200 by vol. to IPA) and adding MAI (1:2 by wgt.
162 to the 2D ligands in solution) produced our most valuable results. However, considering different ligand
163 species this is a large sample space, and one we have not exhausted. Further studies may optimise this
164 for better performance.

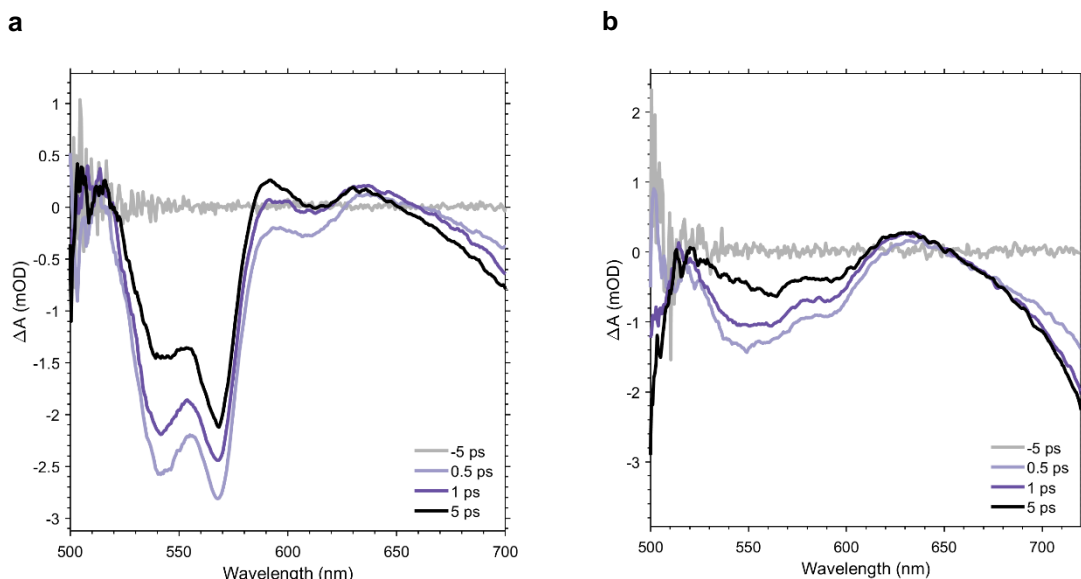


165 **Figure S8 | Transient absorption spectra of 3D $\text{Cs}_{0.05}\text{MA}_{0.1}\text{FA}_{0.85}\text{PbI}_3$ perovskite treated with**
166 **different surface treatments.** (a) Control, (b) 1 mg mL^{-1} MAI in IPA, (c) 1 mg mL^{-1} PEAI in 200:1
167 IPA:DMF solution, (d) 1 mg mL^{-1} PEAI + 0.5 mg mL^{-1} MAI in IPA solution.



168 **Figure S9 | XRD patterns of 3D perovskite films treated with different solutions.** (a) Comparison
169 of an untreated film with PEA1 treated films with and without DMF. 5 $\mu\text{L mL}^{-1}$ of DMF was used, along
170 with 1 mg mL^{-1} of PEA1. It appears that introducing DMF results increased $n = 1$ formation however
171 this is not strongly substantiated by TA spectra (Fig. S8). PbI_2 is also still visible in the PEA1 + DMF
172 treated film implying that with the addition of DMF, the 3D perovskite is dissolved forming PbI_2 on the
173 film surface. (b) Control surface treatments.

174



175 **Figure S10 | TA of heterostructures using increased MAI content.** 3D perovskite films treated
176 with the quasi-2D treatment using (a) 1:1 and (b) 2:1 MAI to PEA1 by wt.

177

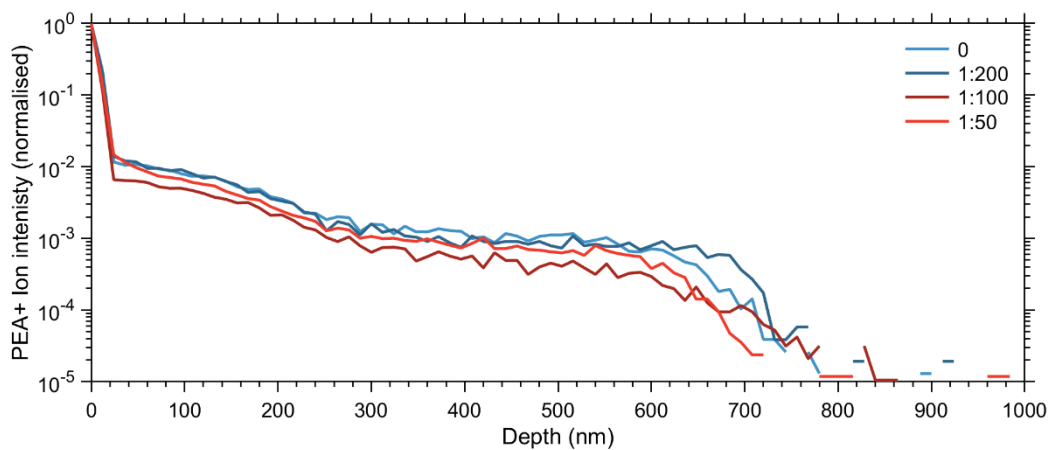
Cation	Absorption wavelength (nm)				
	$n = 1$	$n = 2$	$n = 3$	$n = 4$	$n = 5$
MA	518	570	611	649	682
FA	520	572	-	642	685
Cs	520	565	611	-	-
2D treatment	517	564	605	-	-
quasi-2D treatment (PEA)	-	575	625	665	697

178

179 **Table S4 |** Absorption peaks for different cations and surface treatments transcribed from TA data.
180 Note that the peaks for the 2D and quasi-2D treatments do not exactly align with any individual cation
181 suggesting that the 2D layer is formed form a mixed species.

182

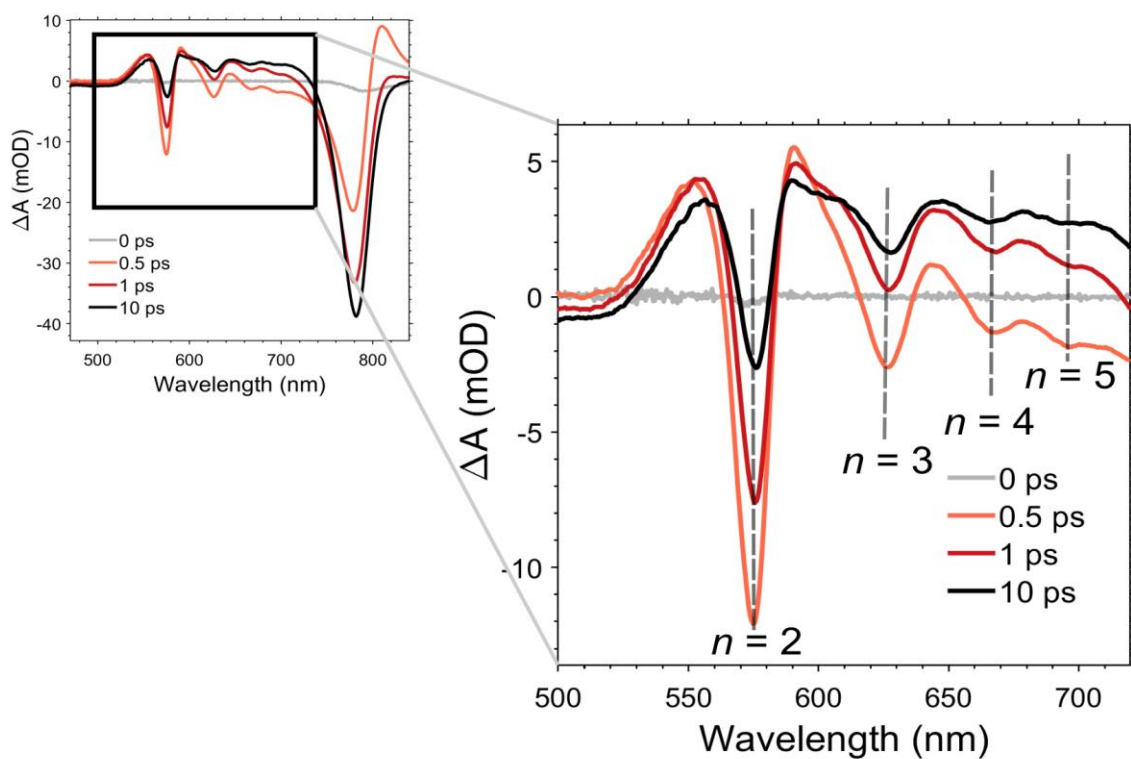
183



184 **Figure S11 | Time of flight second ion mass spectroscopy (ToF-SIMS) of PEA+ ions in**
185 **perovskite films treated with PEAI in solution with different DMF:IPA concentrations.** Across
186 this range (5 μ L DMF in 1 mL IPA to 20 μ L in 1 mL IPA) there is no obvious change in penetration
187 depth for the PEA ligand.

188

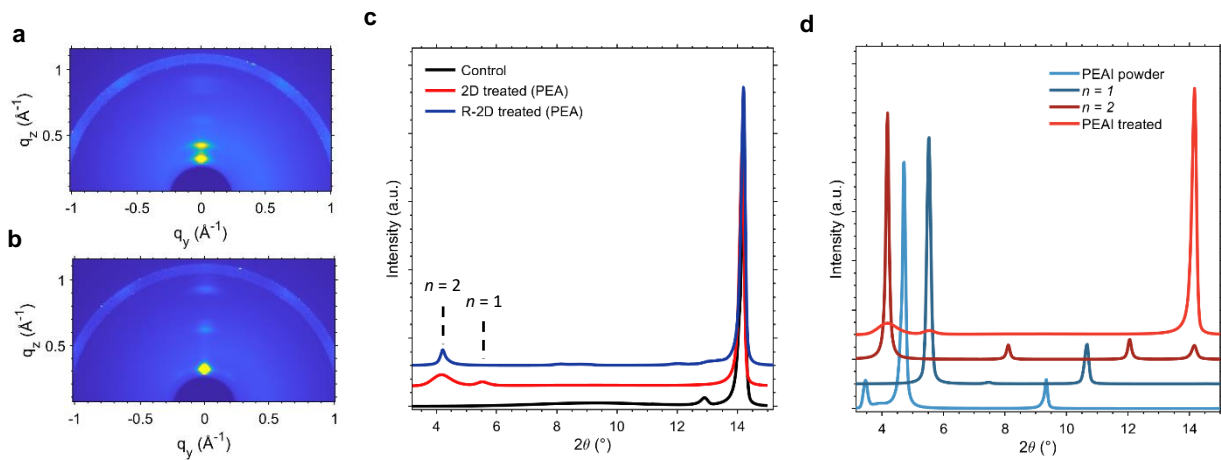
189



190

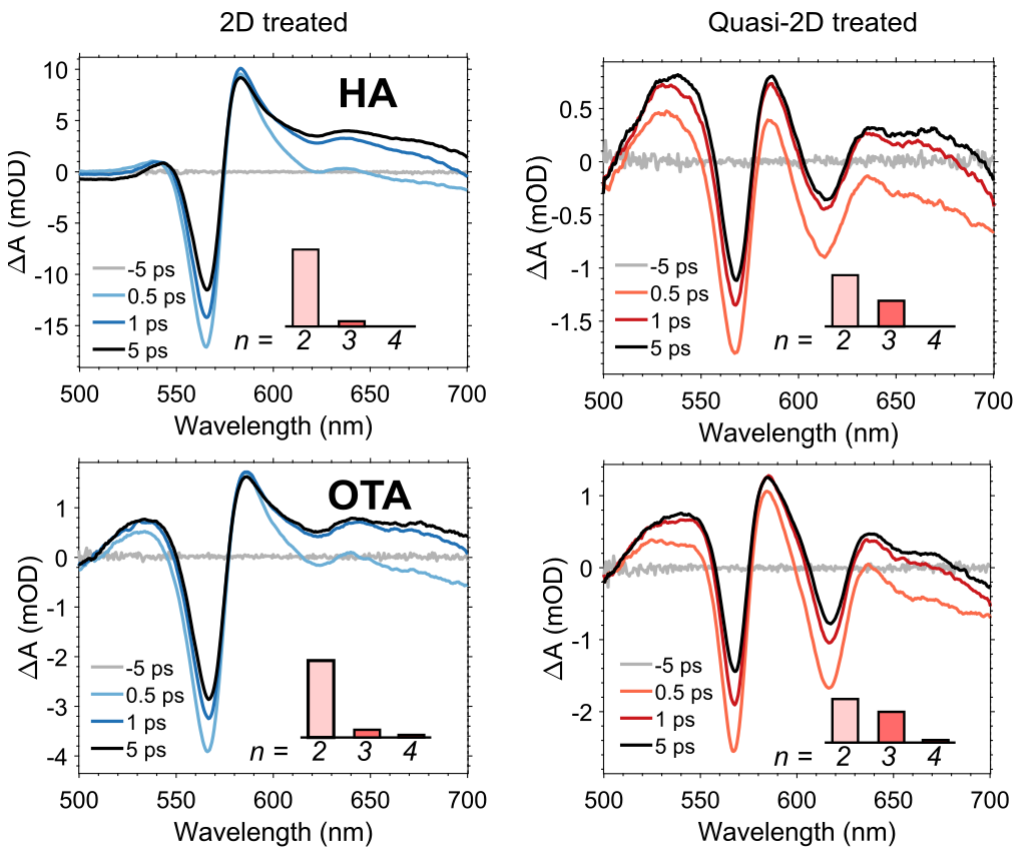
191 **Figure S12 | Full TA spectrum** taken of a PEA treated quasi-2D film. Note that the 3D bleach is
 192 considerably more absorptive than the 2D, such that we have neglected to include these in Fig. 2.

193

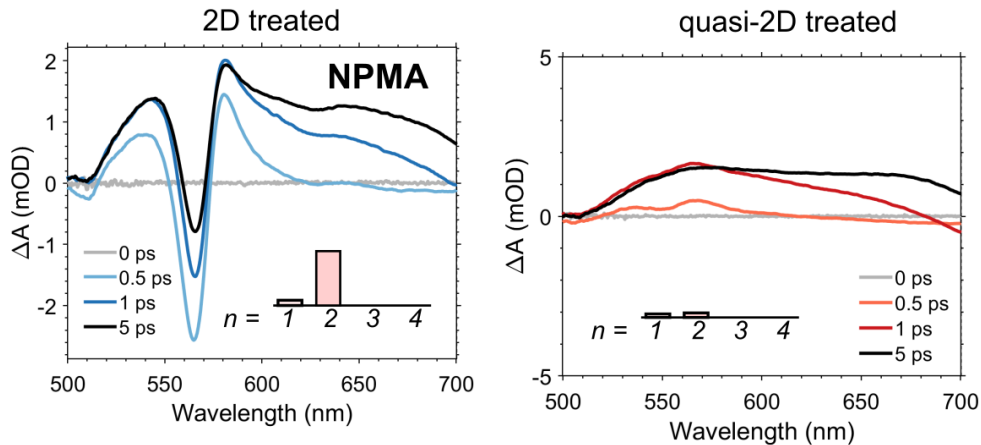


194 **Figure S13 | GIWAXS and XRD results for 2D and quasi-2D treated films using PEA.** (a,b)
195 GIWAXS results of 2D and quasi-2D treated films, respectively. Films were arranged at a small angle
196 (0.3°) relative to the incoming x-ray beam so that the surface of the film is probed rather than the bulk.
197 High intensity spots at $q \sim 0.4 \text{ \AA}^{-1}$ and 0.3 \AA^{-1} for the standard 2D treated film, but only one spot at $q \sim$
198 0.3 \AA^{-1} for the quasi-2D treated film indicate the loss of $n = 1$ RDPs in the quasi-2D treated film.
199 These spots are arranged along the q_z axis, indicating that the RDPs are oriented horizontally with
200 respect to the substrate. (c) XRD results from the same films indicate that only a small proportion of
201 the film has been converted to 2D. To ensure that unreacted PEA1 salt was not mistaken for RDPs, we
202 compared the 2D treated sample with the salt $n = 1$ and $\langle n \rangle = 2$ films in (d). Clearly, we can see that
203 the PEA1 salt is distinct from the peaks formed from either $n = 1$ or $n = 2$ $\text{PEA}_2\text{MA}_{n-1}\text{Pb}_{2n}\text{I}_{3n+1}$

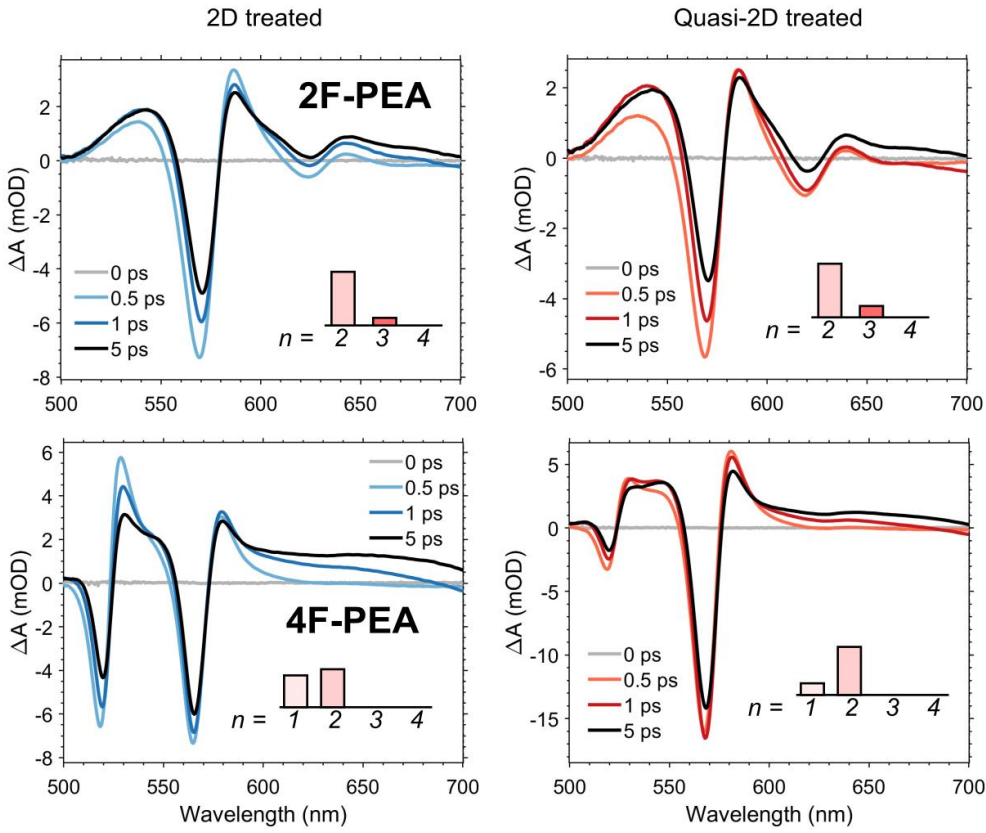
204



205 **Figure S14 | TA spectra of films treated with HA and OTA ligands.** The inset bar charts represent
206 the relative absorption from each RDP species.

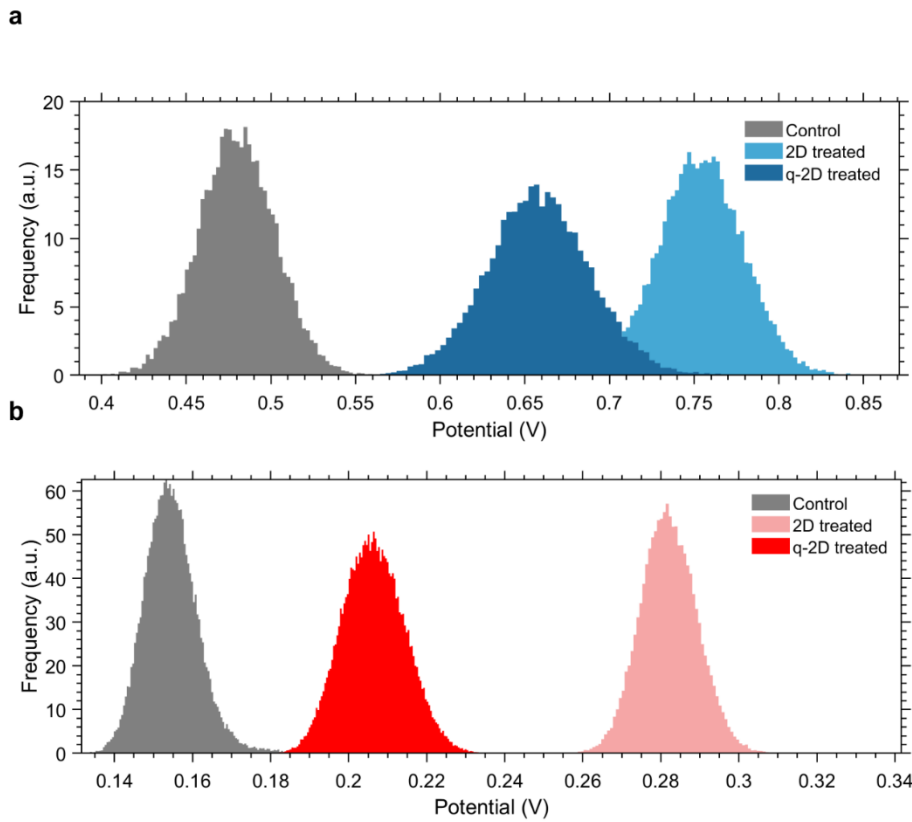


207 **Figure S15 | TA spectra of films treated with NPMA ligands.** The inset bar charts represent the
208 relative absorption from each RDP species. RDPs struggled to form during the quasi-2D treatment.



209 **Figure S16 | TA spectra of films treated with 2F-PEA and 4F-PEA ligands.** The inset bar charts
 210 represent the relative absorption from each RDP species.

211

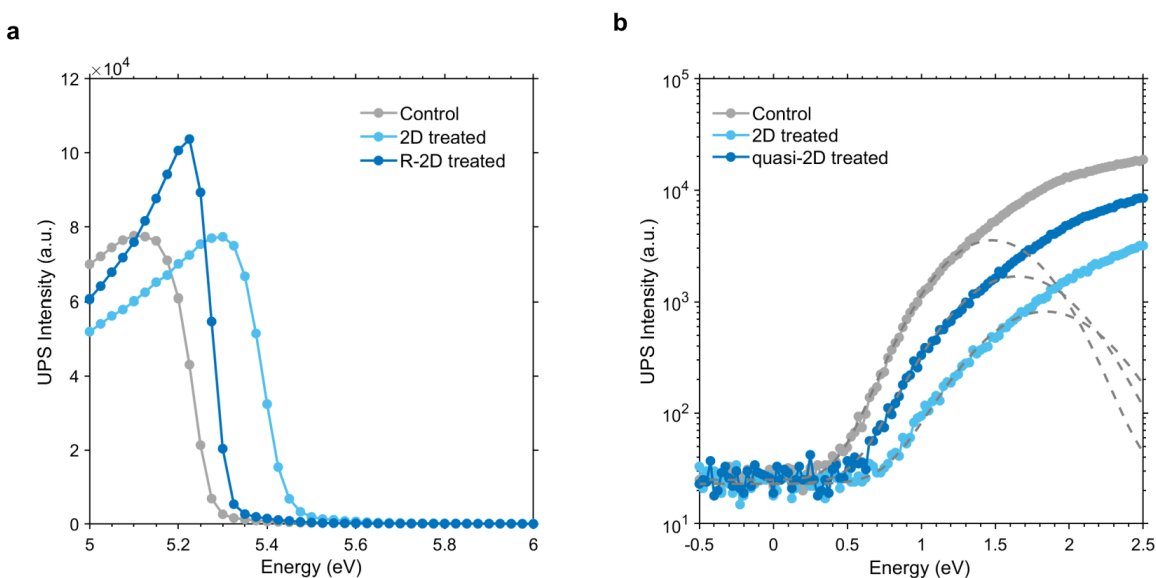


212 **Figure S17 | Potential profiles from Kelvin probe measurements** (a) PEA treated films, (b) 3F-PEA
 213 treated films. The overall shift in potential between (a) and (b) is assumed to be due to changing the
 214 KPFM tip as measurements were made on separate occasions with different probes.

215

216 **Supplementary Text 4 | UPS and IPES measurements**

217 As mentioned in the main manuscript, we used ultraviolet photon spectroscopy (UPS) and inverse
 218 photoelectron spectroscopy (IPES) to directly measure the valence band and conduction band of our
 219 film surfaces. The combined UPS and IPES measurements reported in Figures 3, S18 and Table S5
 220 were collected with photon and electron energies lower than those of typical UPS and IPES
 221 systems (10.2 eV photon for UPS and less than 5 eV electrons for IPES), which has been shown to
 222 minimize sample damage.^{21,22} All ionization energy (IE) and electron affinity (EA) values are
 223 assigned based on a Gaussian fit to the UPS and IPES onset region performed on a logarithmic scale.
 224 Following work by Endres, *et al.*,²³ 2.9σ is subtracted from, or added to, the Gaussian peak location to
 225 determine the IE of EA, respectively, where σ is the width of the Gaussian (FWHM = 2.35σ).
 226 The spectra from combined UPS/IPES measurements on control and PEA-based 2D and quasi-2D
 227 samples are found in Fig. S18, the results are summarised in Table S5.



228

229 **Figure S18 | UPS spectra** showing the secondary electron cut-off region (a) and the valence band onset
 230 region (b) with the fittings to a Gaussian function shown in (b) with dashed lines. The x-axis energy
 231 scale is with respect to the Fermi energy ($E_F = 0$) for untreated, 2D treated and quasi-2D treated films.

232

	WF	VB χ_0	VB σ	VBM (IE)	CB χ_0	CB σ	CBM (EA)	Bandgap (eV)
Control	4.92	1.47	0.31	5.49	3.08	0.29	3.93	1.56
2D (PEA) treated	4.76	1.84	0.37	5.53	2.50	0.35	3.51	2.02
quasi-2D (PEA) treated	4.88	1.65	0.35	5.51	2.90	0.31	3.79	1.71

233 **Table S5 | Fitting parameters and calculated band alignment values** from Gaussian fitting of
 234 combined UPS/IPES measurement from control and treated films.

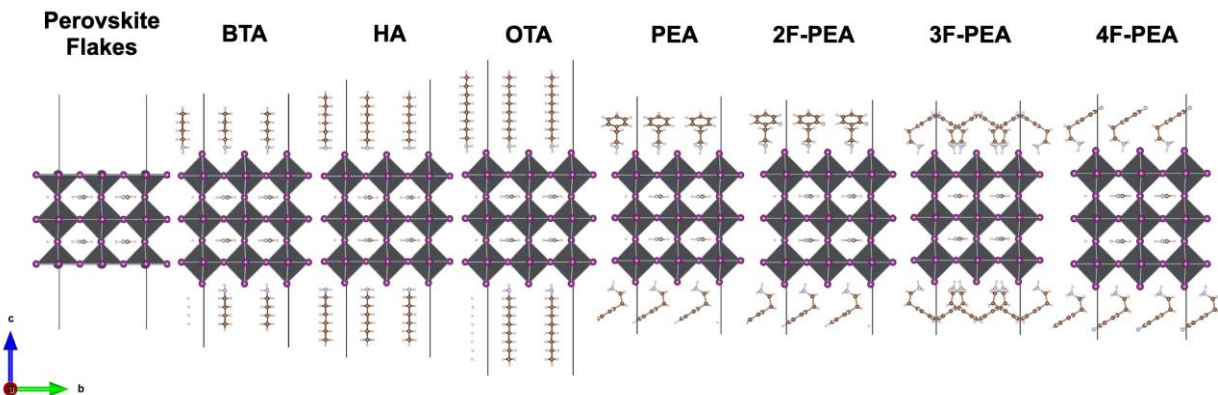
235

236 **Supplementary text 5 | Density Functional Theory Calculations for RDP width selectivity**

237 DFT calculations were performed using the FHI-aims²⁴⁻²⁶ all-electron code. The default numerical
 238 settings, referred to as “light” in FHI-aims were used. Local minimum-energy geometries of the Born-
 239 Oppenheimer surface were obtained with residual total energy gradients below 1×10^{-2} eV Å⁻¹ for
 240 atomic positions using the PBE-GGA functional²⁷ within the vdW correction following the
 241 Tkatchenko-Scheffler method²⁸ (PBE+TS). A unified k-point grid $2 \times 2 \times 1$ was used to sample the
 242 Brillouin zone that corresponds to the slab shown in Figure S19.

243

244



245

246 **Figure S19 | Idealized crystal structure of $n = 3$ perovskite flakes ($FA_{n-1}Pb_nI_{3n-1}$) and 2D**
 247 **perovskite flakes ($L_2FA_{n-1}Pb_nI_{3n+1}$, $L = BTA, HA, OTA, PEA, 2F-PEA, 3F-PEA, 4F-PEA$).** The
 248 specific arrangements of each ligand were built according to their experimentally defined crystal
 249 structure; for BTA, HA, and OTA the BTA structural base was used from.²⁹ The structures of PEA,
 250 2F-PEA, 3F-PEA, 4F-PEA are based on reference.³⁰ The c-direction for all the slabs was set to 100
 251 Å.

252

253 To explore the underlying mechanisms which control RDP formation, the formation process of a
 254 2D/3D heterostructure was divided into three intermediate steps:

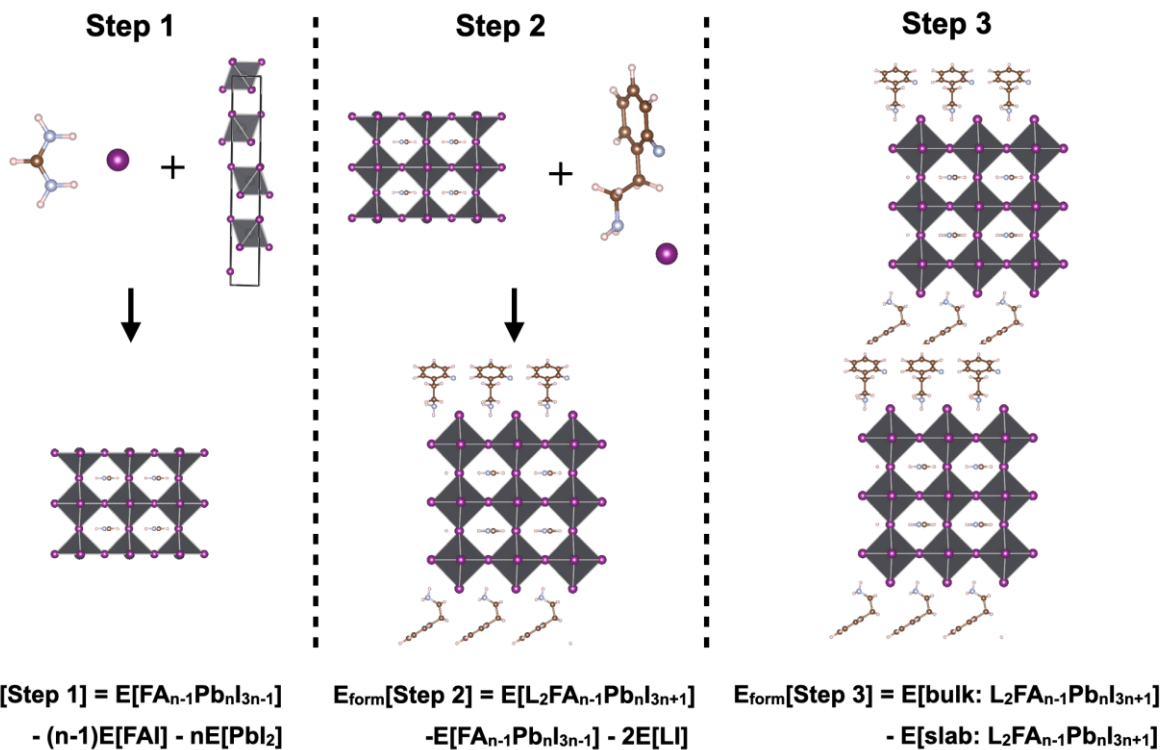
- 255 1. Dissolved PbI_2 and FAI at the surface will firstly form perovskite flakes, $(FA)_{n-1}Pb_nI_{3n-1}$.
- 256 2. The products of Step 1) will then be selected by different ligands (from the corresponding
 257 iodine salt, LI) to form 2D perovskites flakes, $L_2(FA)_{n-1}Pb_nI_{3n+1}$
- 258 3. Those 2D perovskites flakes will stack in the z-direction according to van der Waals
 259 interactions to form bulk 2D perovskites.

260

261 We thus calculated the corresponding formation energies (the definitions are shown in Figure S20) of
 262 each step by density functional theory. Considering that step 3) should be the same regardless of n for
 263 a given ligand L, it was ignored. However, we acknowledge that this step may be an important driving
 264 force for the lower n 2D perovskites such as $n = 1$.

265

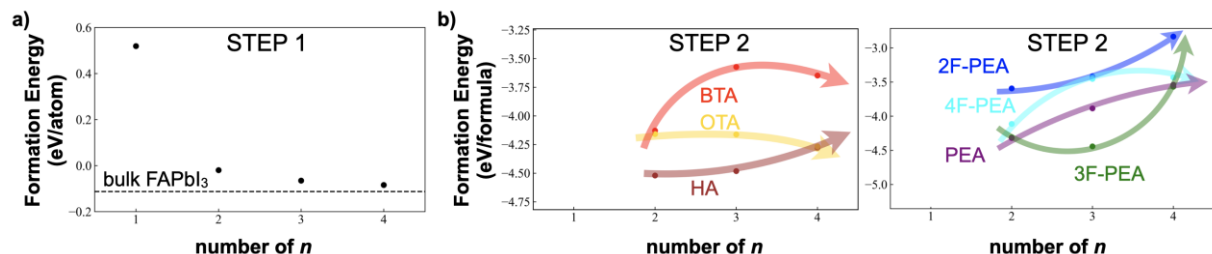
266



267

268 **Figure S20** | Schematic plots about the formation energy definition of three intermediate steps in the
269 formation of 2D perovskite.

270



271

272 **Figure S21** | The PBE+TS calculated formation energy of a) step 1 and b) step 2 for different RDP
273 widths ($n = 1, 2, 3, 4$) and different ligands ($L = \text{BTA}, \text{HA}, \text{OTA}, \text{PEA}, 2\text{F-PEA}, 3\text{F-PEA}, 4\text{F-PEA}$).
274 In a), the formation energy of bulk FAPbI₃ is shown as a black dashed line.

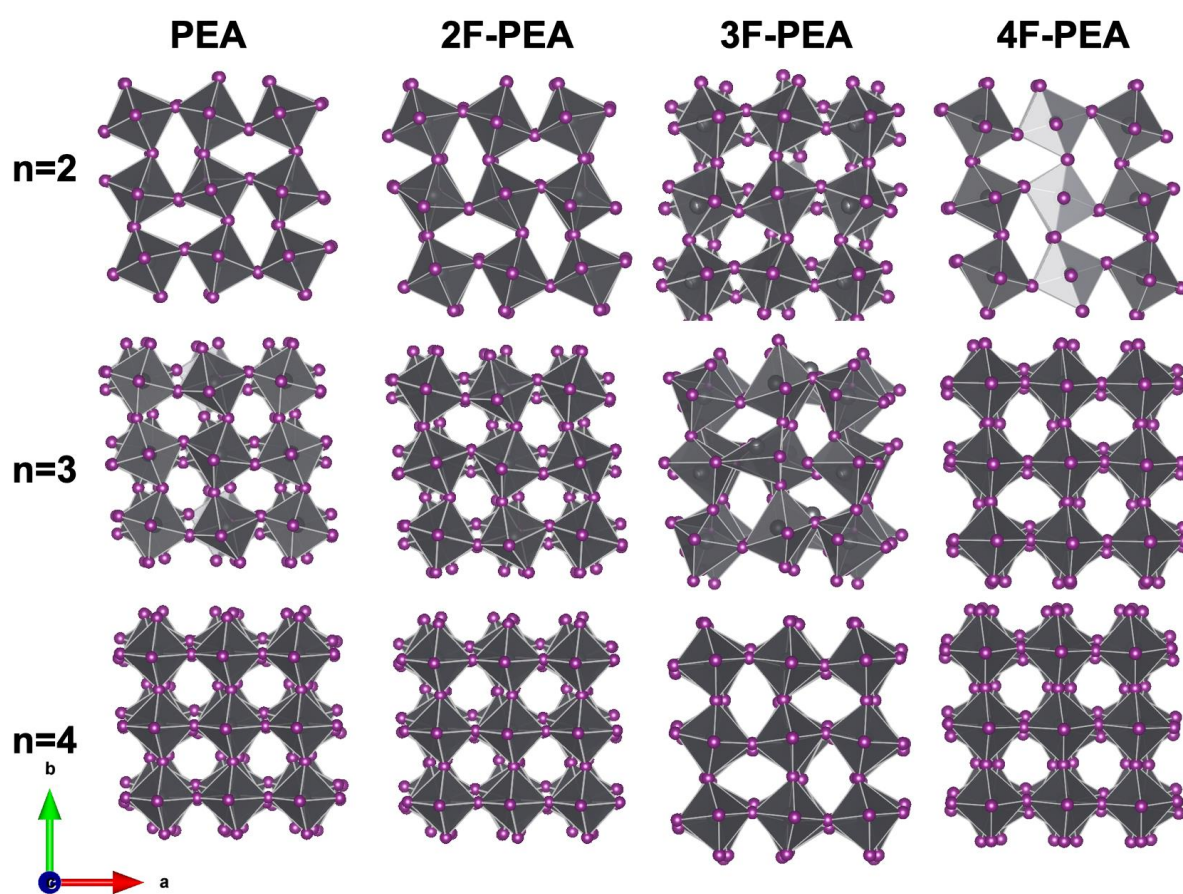
275

276 The formation energies were calculated by PBE+TS for different RDP widths ($n = 1, 2, 3, 4$) and
277 different ligands ($L = \text{BTA}, \text{HA}, \text{OTA}, \text{PEA}, 2\text{F-PEA}, 3\text{F-PEA}, 4\text{F-PEA}$) are shown in Figure S21.
278 The corresponding PBE+TS relaxed PbI₂ octahedral for different RDP widths ($n = 2, 3, 4$) and ligands
279 ($L = \text{PEA}, 2\text{F-PEA}, 3\text{F-PEA}, 4\text{F-PEA}$) are shown in Figure S22. Step 1) is independent of ligand and
280 only depends on the amount of dissolved PbI₂ and FAI in the surface region. From calculated
281 PBE+TS formation energies, we find that $n = 1$ flakes are not easily formed compared to wider
282 RDPs ($n = 2, 3, 4$). As a result, if we have enough PbI₂, and FAI dissolved from the surface 3D
283 perovskite (which is the case in our Quasi-2D treatment), the $n = 1$ perovskites flakes will not form
284 and we will not detect $n = 1$ 2D perovskite, which is consistent within experimental results.

285

286 For step 2), we find that different ligands show different selection behaviour for different RDP widths.
287 With the exception of the 3F-PEA ligands, all the ligands display the same uphill trend: as n increases,
288 the formation energy becomes larger. This agrees with the observation that the $n = 2$ peak is the major
289 species found for all ligands apart from 3F-PEA (BTA, HA, OTA, PEA, 2F-PEA, 4F-PEA) as the
290 formation energy for $n = 2$ is consistently lowest (most stable). Considering only chain length (BTA,
291 HA, OTA), we find that as the chain becomes longer, the difference between the formation energy of
292 $n = 2$, and $n = 3$ becomes smaller. This explains why we observe stronger absorption from $n = 3$ as
293 chain length increases for ligands (BTA, HA, OTA). However, as $n = 2$ still has the lowest formation
294 energy (most stable), the dominant signal remains $n = 2$ in the quasi-2D treatment. For 3F-PEA,
295 however, we find that $n = 3$ has the lowest formation energy (most stable) compared to $n = 2$ or 4.
296 This is consistent with our experimental finding that the $n = 3$ becomes dominant using the quasi-2D
297 treatment.

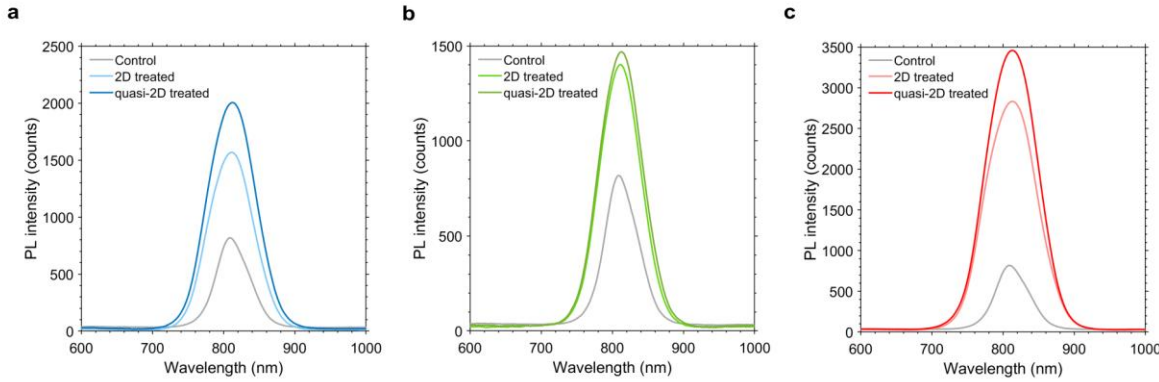
298



299

300 **Figure S22 | The PBE+TS relaxed slab structures** (only the PbI_2 octahedral are shown) for different
301 RDP widths ($n = 2, 3, 4$) and ligands ($L = \text{PEA}, \text{2F-PEA}, \text{3F-PEA}, \text{4F-PEA}$).

302



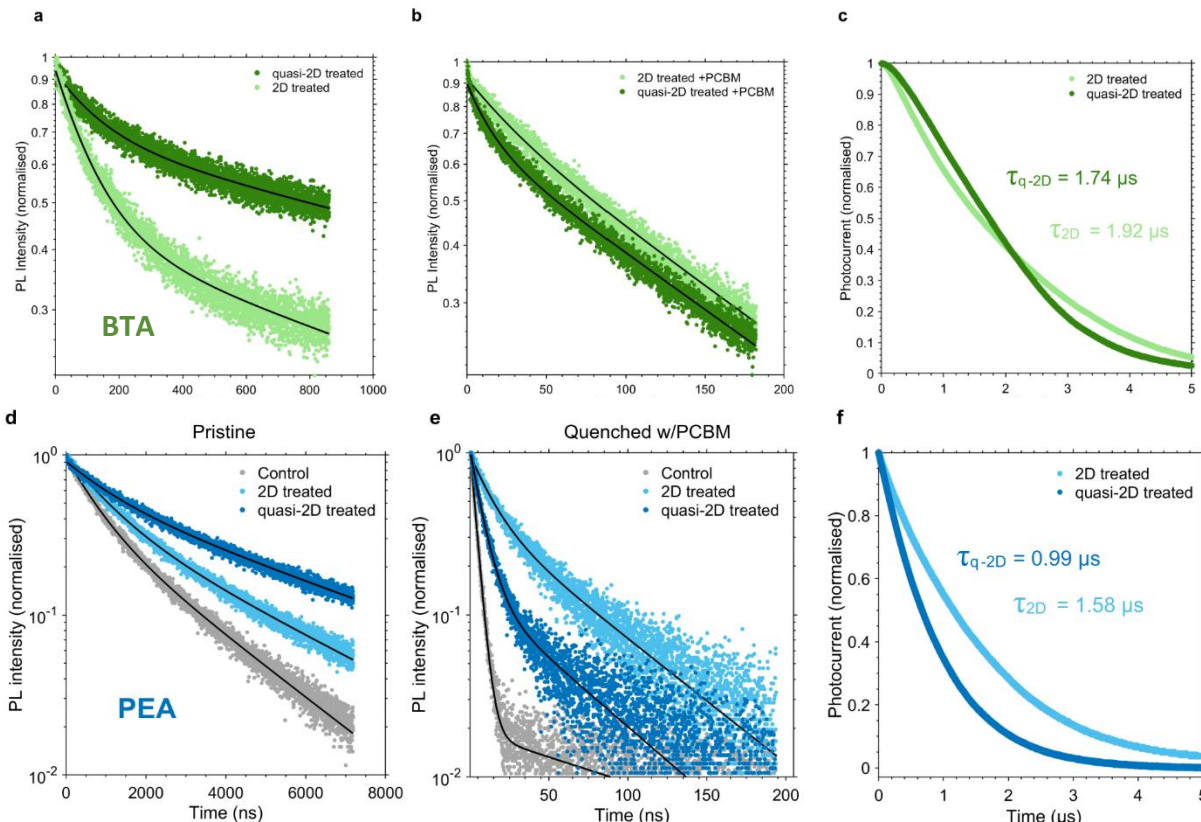
303

Figure S23 | Steady-state PL measurements of Control, 2D treated and quasi-2D treated films for
(a) PEA, (b) BTA and (c) 3F-PEA

Ligand	Treatment	PLQY
Control	None	0.67
BTA	2D	1.44
	Quasi-2D	1.58
PEA	2D	1.73
	Quasi-2D	2.33
3F-PEA	2D	3.30
	Quasi-2D	3.91

306

Table S6 | Calculated PLQY values for each treatment



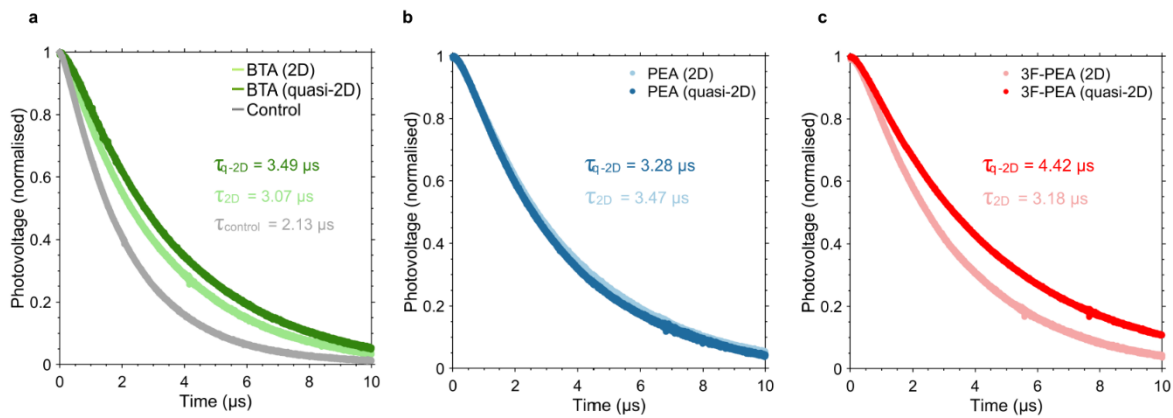
307

Figure S24 | Transient PL and photocurrent measurements of 2D treated and quasi-2D treated films using BTA and PEA. Transient PL of (a,d) pristine films, (b,e) films quenched with PCBM. (c,f) transient photocurrent measurements of 2D and quasi 2D treated films. The times in μs represent the exponential lifetime for the current to decay after excitation.

308

309

310



311

312 **Figure S25 | Transient photovoltage measurements** of control, 2D treated and quasi-2D treated
 313 films using (a) BTA, (b) PEA and (c) 3F-PEA. The times in μs represent the exponential lifetime for
 314 the voltage decay after excitation.

315

		τ_1 (ns)	τ_2 (ns)
Control	-	681	2267
	+ PCBM	4.6	581
PEA	2D	958	3385
	2D + PCBM	12.1	196
	quasi-2D	1117	4800
	quasi-2D + PCBM	6.2	317
3F-PEA	2D	2309	2309
	2D + PCBM	9.2	17.9
	quasi-2D	3398	3398
	quasi-2D + PCBM	4.9	8.2
BTA	2D	118.3	1802
	2D + PCBM	33.3	176
	quasi-2D	146.5	2563
	quasi-2D + PCBM	16.3	177

316 **Table S7 | Summary of calculated photoluminescent lifetimes**

317

318 **Supplementary text 6 | One dimensional diffusion/recombination model**

319 In order to unravel the effect of our surface treatments, we employed a one-dimensional carrier
 320 diffusion/recombination model to fit power dependent transient absorption decay curves. This model
 321 has been successfully used in both inorganic semiconductors^{31,32} and perovskites.^{33,34} It is briefly
 322 introduced as follows:

323
$$\frac{\partial N(x, t)}{\partial t} = D \frac{\partial^2 N(x, t)}{\partial x^2} - (k_1 N(x, t) + k_2 N(x, t)^2 + k_3 N(x, t)^3) \quad (1)$$

324 Initial carrier distribution: $N(x, 0) = N(0, 0) \times \exp(-\alpha x) \quad (2)$

325 Boundary conditions (front and back interface recombination velocities):

326
$$\left. \frac{\partial N(x, t)}{\partial x} \right|_{x=0} = \frac{S_f}{D} N(0, t) \quad (3)$$

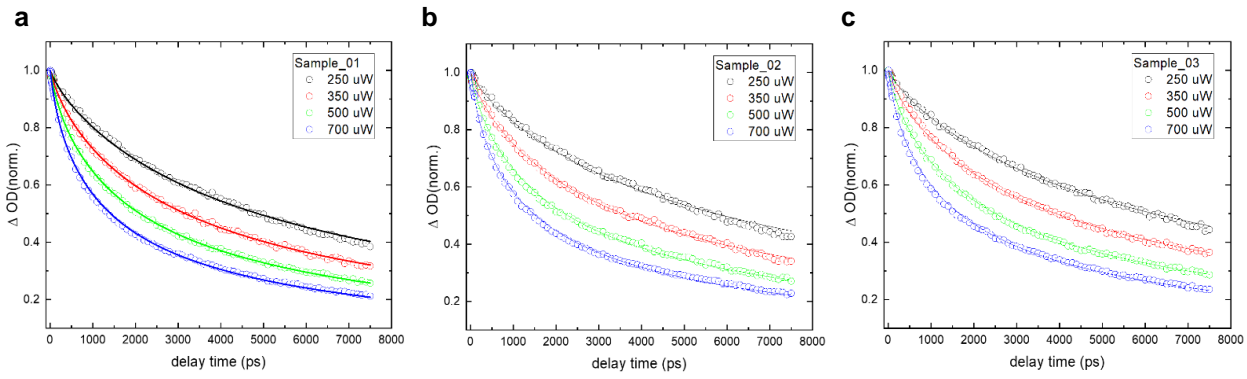
327
$$\left. \frac{\partial N(x, t)}{\partial x} \right|_{x=d} = -\frac{S_b}{D} N(d, t) \quad (4)$$

328 Herein, $N(x, t)$ denotes the carrier density which is a function of both space (x) and time (t); S_f and S_b
 329 denote surface/interface recombination velocities at the front (f) and back (b) surfaces/interfaces,
 330 respectively; bulk-specific parameters are the diffusion coefficient (D) and the 1st (k_1), 2nd (k_2), and 3rd
 331 (k_3) order recombination coefficients; α is the absorption coefficient; d represents the film thickness. A
 332 useful feature of this model is that it not only takes into account of bulk recombination (k_1, k_2, k_3) and
 333 diffusion, but also takes into account of what is happening on the surface/interface.

334 To unravel the bulk recombination/diffusion and passivating effect of the 2D and quasi-2D treatments,
 335 we performed global fitting on control, 2D treated and quasi-2D treated samples (Fig. S26). These three
 336 samples share the same bulk properties and only differ on the surface. Fitting results are presented in
 337 S26 as well as Table S8. The 1st, 2nd, and 3rd-order recombination coefficients were all evaluated
 338 accordingly. And the S_f is a good indication of surface trap state density. It can be clearly observed that
 339 both 2D and quasi-2D treatments reduce the surface recombination velocity by half.

Sample	Adj. R-square	D, cm ² s ⁻¹	S _f , cms ⁻¹ ,	k ₁ , s ⁻¹ ,	k ₂ , cm ⁻³ s ⁻¹ ,	k ₃ , cm ⁶ s ⁻¹ ,	μ, cm ² V ⁻¹ s ⁻¹ ,	Diff length (nm)
Control	0.99832	0.154 ± 0.015	577 ± 85	(1.86 ± 0.01) × 10 ⁶	(6.27 ± 4.09) × 10 ⁻¹¹	(6.96 ± 8.81) × 10 ⁻²⁹	6.006 ± 0.585	(2.877 ± 0.148) × 10 ³
Control/2D			303 ± 82					
Control/quasi-2D			308 ± 85					

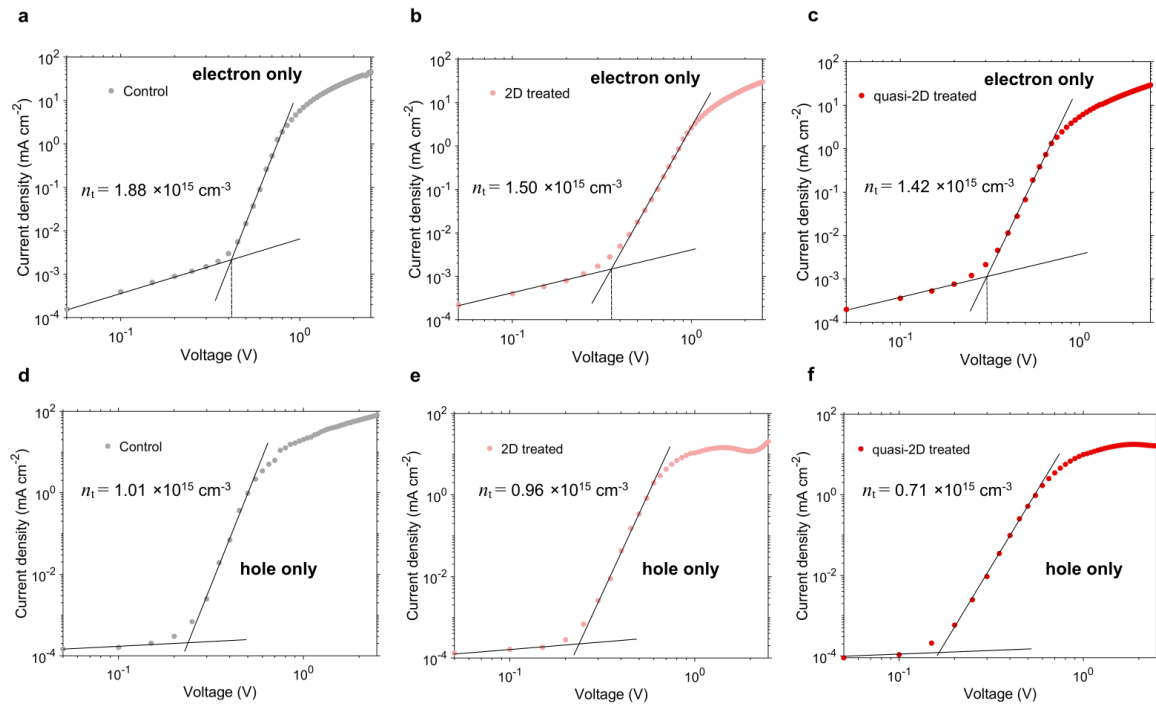
340
 341 **Table S8 | Coefficients calculated from the one-dimensional carrier diffusion/recombination**
 342 **model** S_f denotes the surface/interface recombination velocity at the front (f) surface/interface; bulk-
 343 specific parameters are the diffusion coefficient (D) and the 1st (k_1), 2nd (k_2), and 3rd (k_3) order
 344 recombination coefficients. We also calculated the mobility μ and the diffusion length.



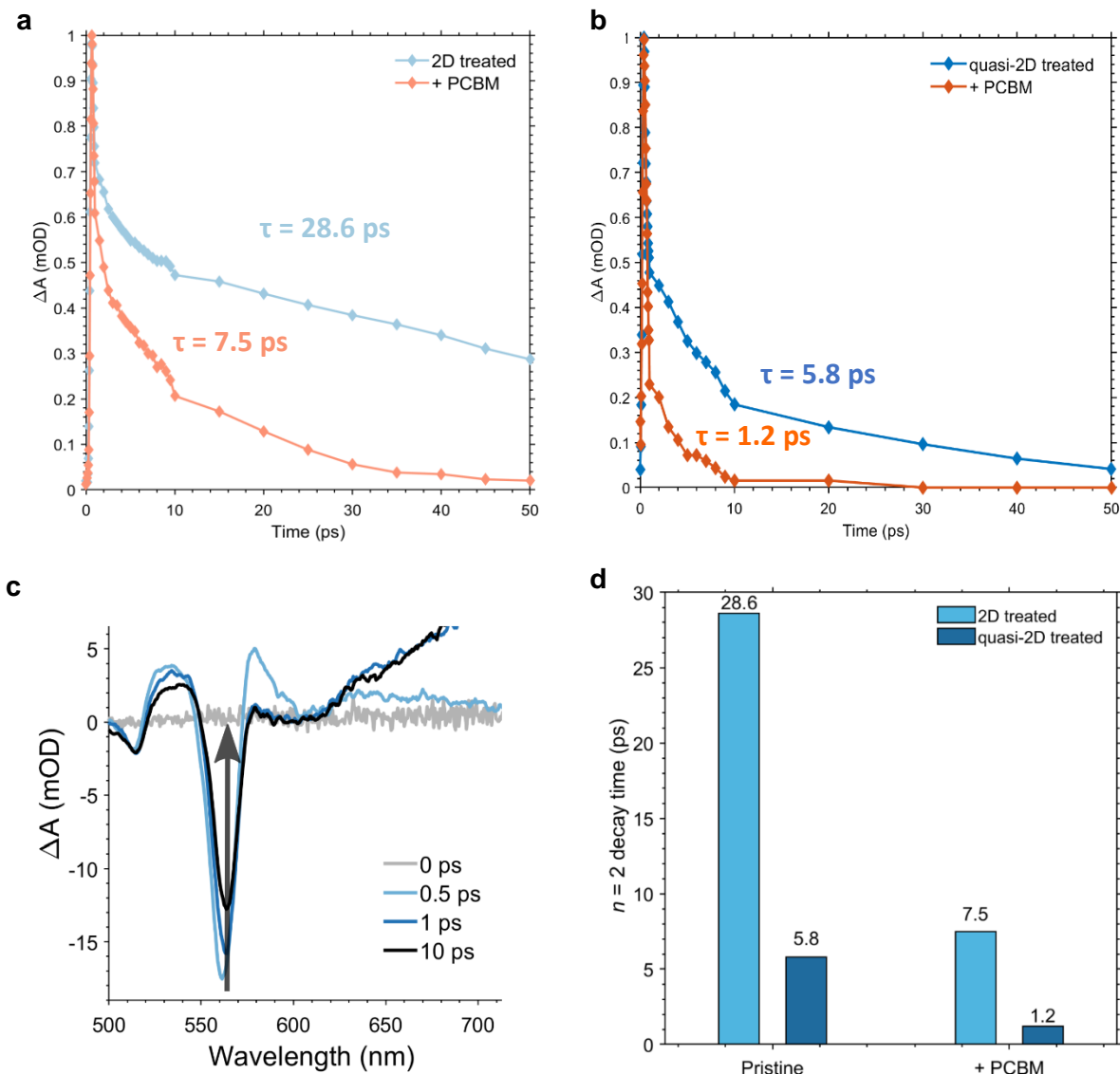
345

346 **Figure S26 | Global fitting** of a) control, b) 2D treated and c) quasi-2D treated samples.

347



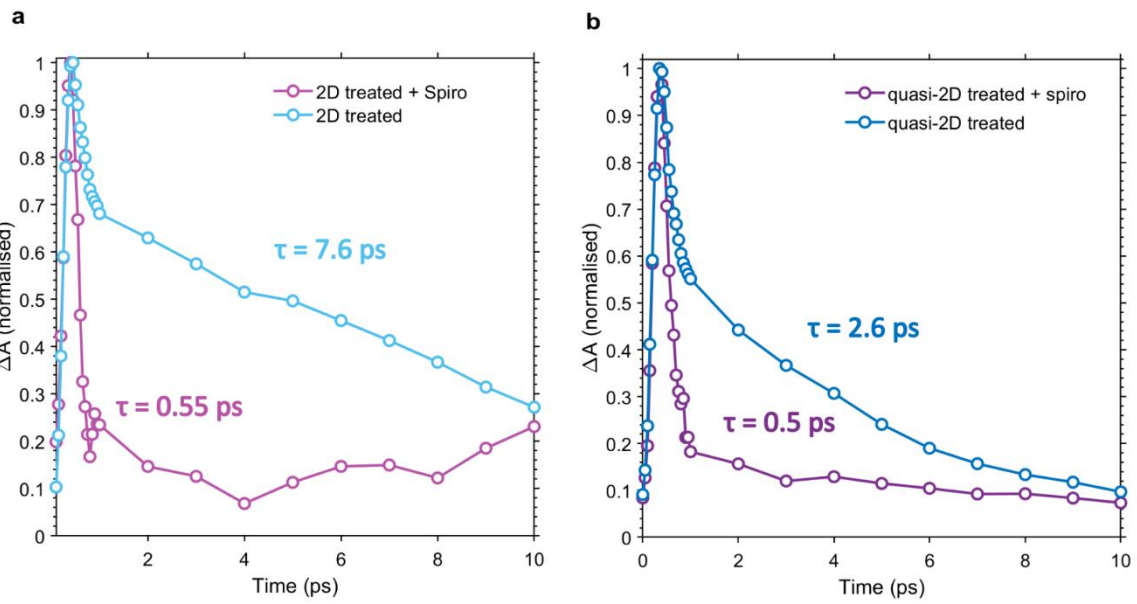
350 **Figure S27 | SCLC measurements for Control, 2D and quasi-2D treated films** a-c) electron only
 351 devices, d-f) hole only.



353

354 **Figure S28 | Transient absorption traces of the $n = 2$ bleach (~ 570 nm) for 2D and quasi-2D**
 355 **treated films (using PEAI) with and without a PCBM extraction layer.** The films were excited by
 356 a 450 nm ($5 \mu\text{Jcm}^{-2}$) pump pulse. When a PCBM layer was added, the absorption from the 2D decays
 357 more quickly for both the 2D and quasi-2D treated films indicating that charge extraction into the
 358 PCBM is favoured over charge tunnelling to $n > 2$ 2D species in the quasi-2D treated films.
 359 Monoexponential fitting was used to calculate the lifetime (τ). Time traces for (a) a 2D treated film,
 360 and (b) a quasi-2D treated film. (c) Illustration of $n = 2$ bleach decay. (d) Summary of decay times.
 361 Note that the rapid decrease in decay time using PCBM for both treatments suggests that carrier
 362 extraction into $n > 2$ RDP is does not limit charge extraction.

363

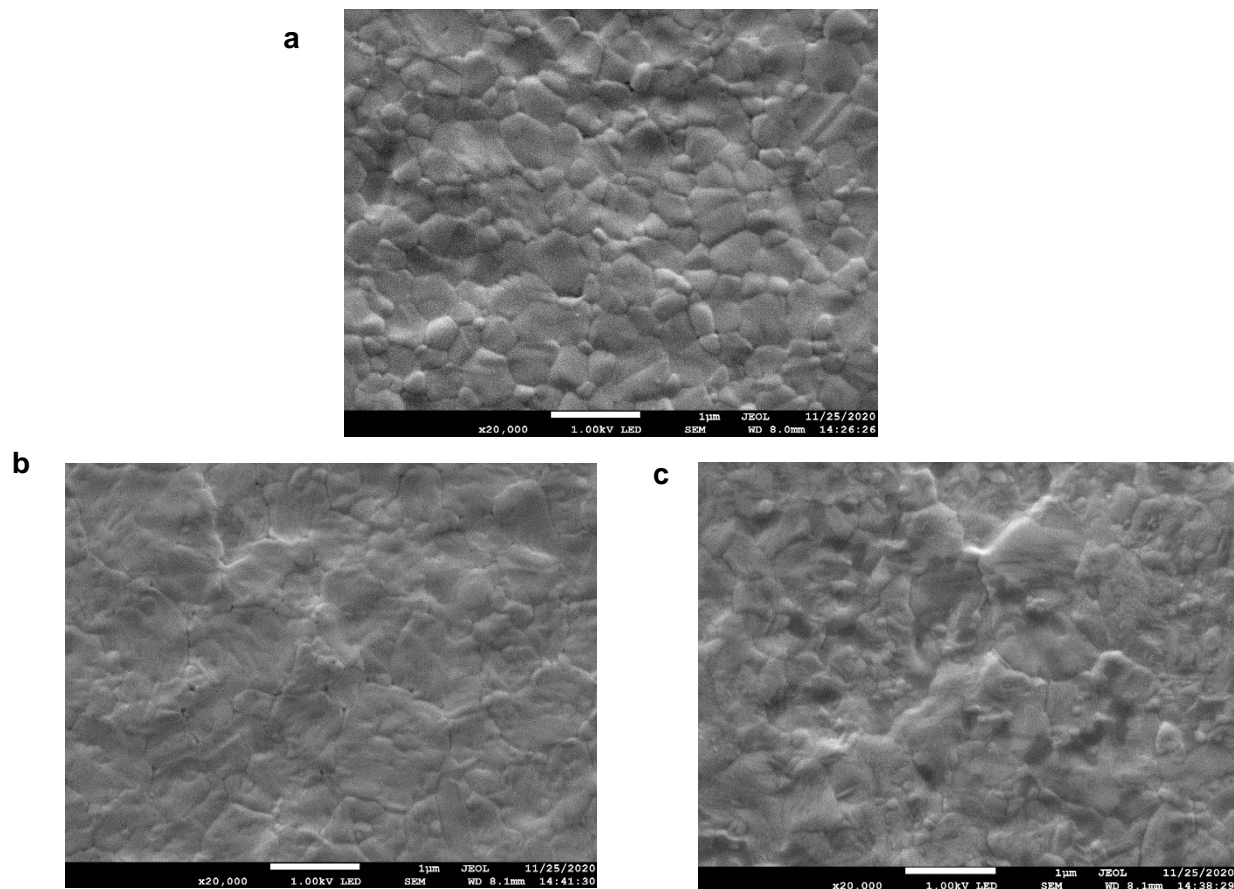


364

365 **Figure S29 | Transient absorption traces of the $n = 2$ bleach (~ 570 nm) for 2D and quasi-2D**
 366 **treated films (using PEA1) with and without a Spiro-OMeTAD extraction layer.** The films were
 367 excited by a 450 nm ($5 \mu\text{J cm}^{-2}$) pump pulse. Results are similar to Figure S28 above, though the
 368 extraction from Spiro seems to be more effective as the signal decays in < 1 ps.

369

370



371

372

373 **Figure S30 | SEM images** of the surface of (a) Control, (b) 2D treated and (c) quasi-2D treated films

374

375

376

377

378

379

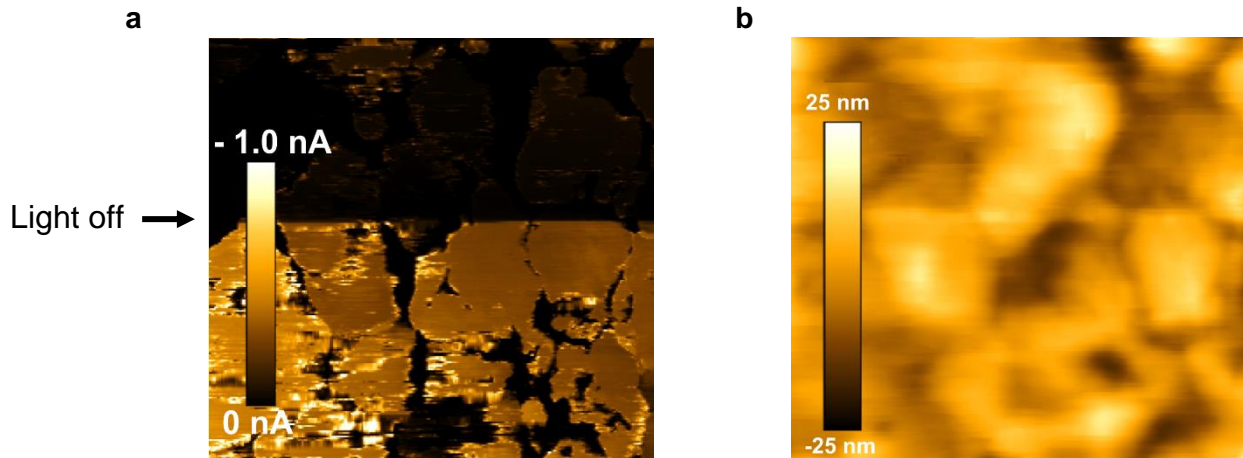
380

381

382

383

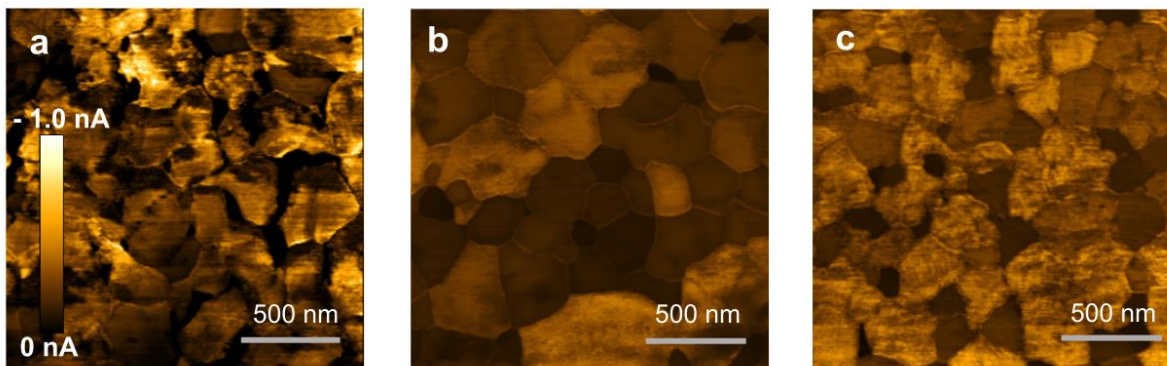
384



385

386 **Figure S31 | Effect of illumination on C-AFM.** Untreated perovskite film on NiO_x/ITO substrate
387 under illumination for the first half of a scan. (a) conductive AFM scan, (b) height trace.

388



389

390 **Figure S32 | C-AFM of different samples.** Perovskite films on NiO_x/ITO substrate under illumination.
391 (a) control, (b) 2D treated, (c) quasi-2D treated.

392

393

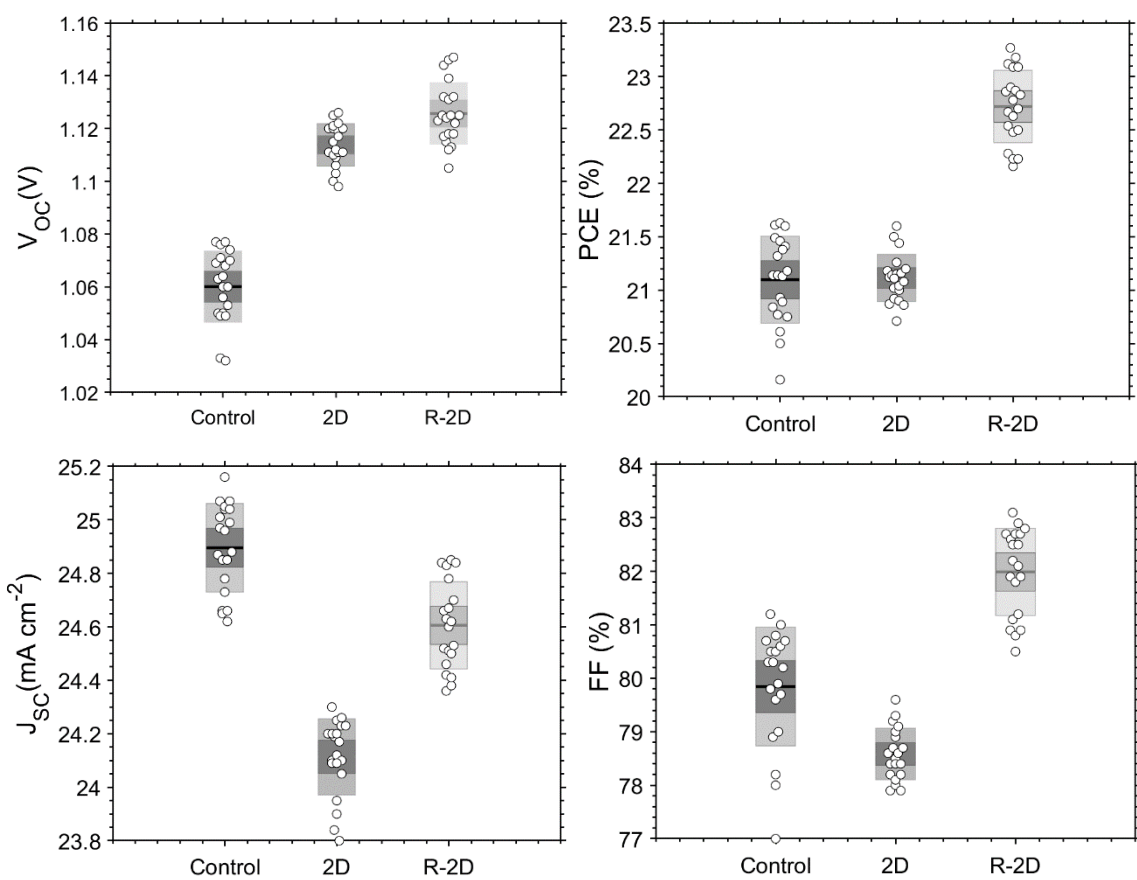
394

395

396

397

398



399

400

401 **Figure S33 | Performance statistics** for PEA treated devices. Taken from 20 devices of each control,
402 2D treated and quasi-2D treated.

403

404

405

406

407

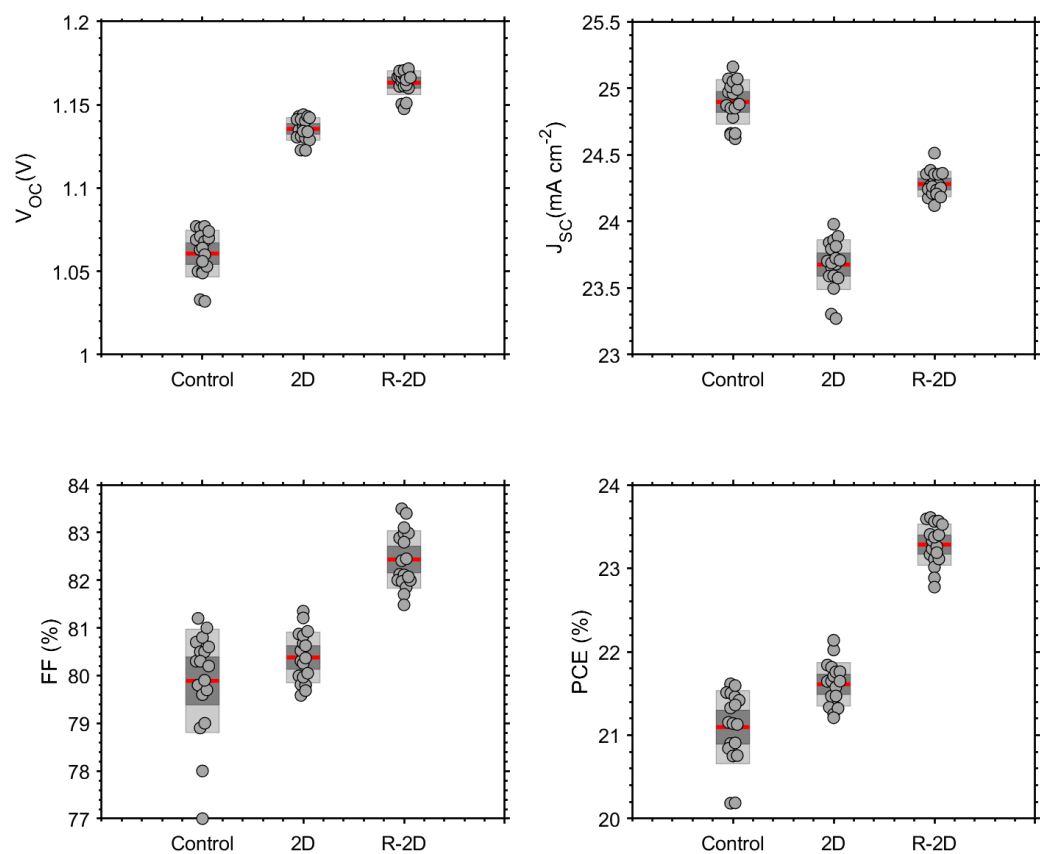
408

409

410

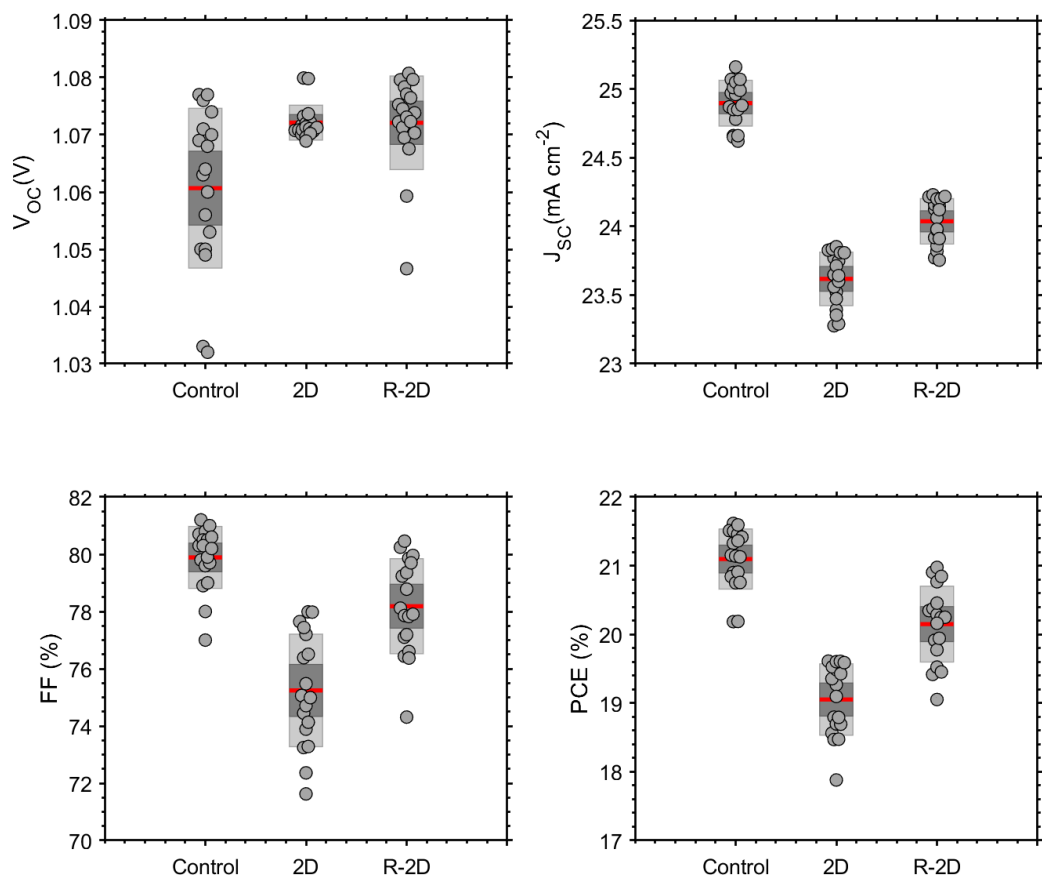
411

412



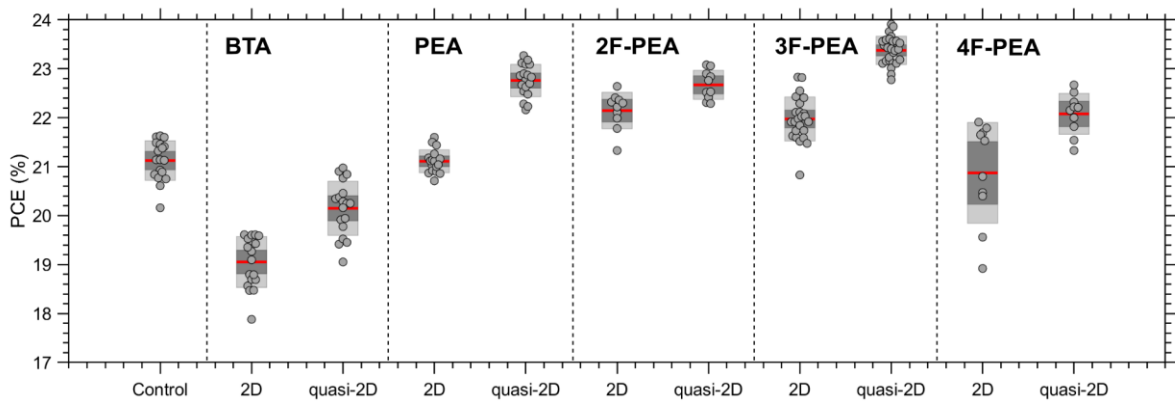
413 **Figure S34 | Performance statistics** for 3F-PEA treated devices. Taken from 20 devices of each
 414 control, 2D treated and quasi-2D treated.

415



416

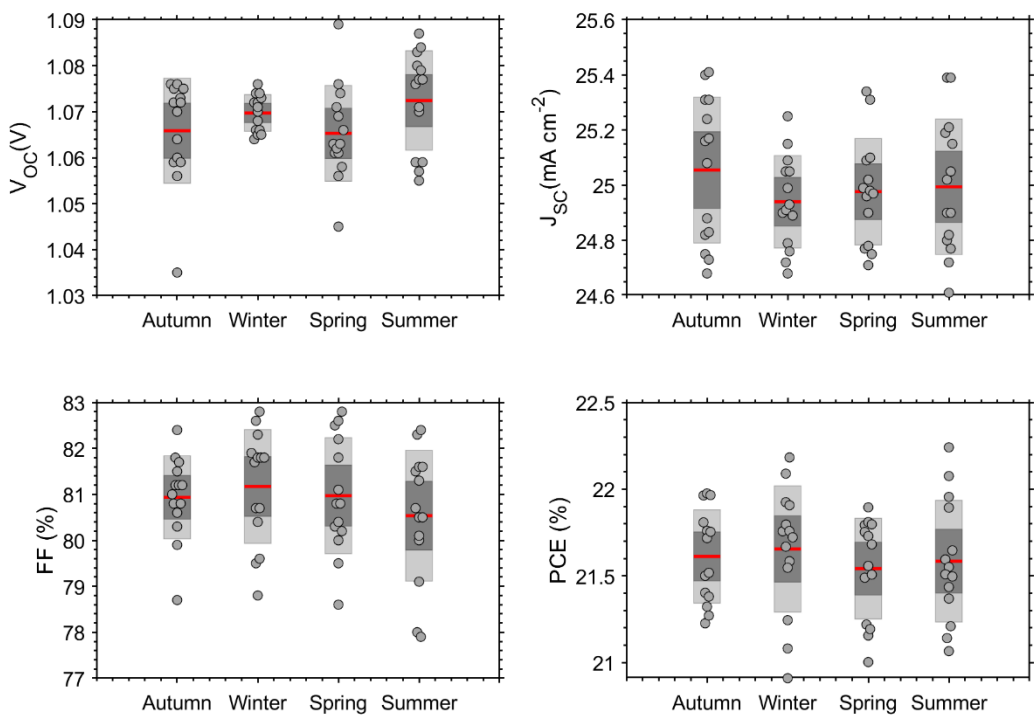
417 **Figure S35 | Performance statistics** for BTA treated devices. Taken from 20 devices of each control,
418 2D treated and quasi-2D treated.



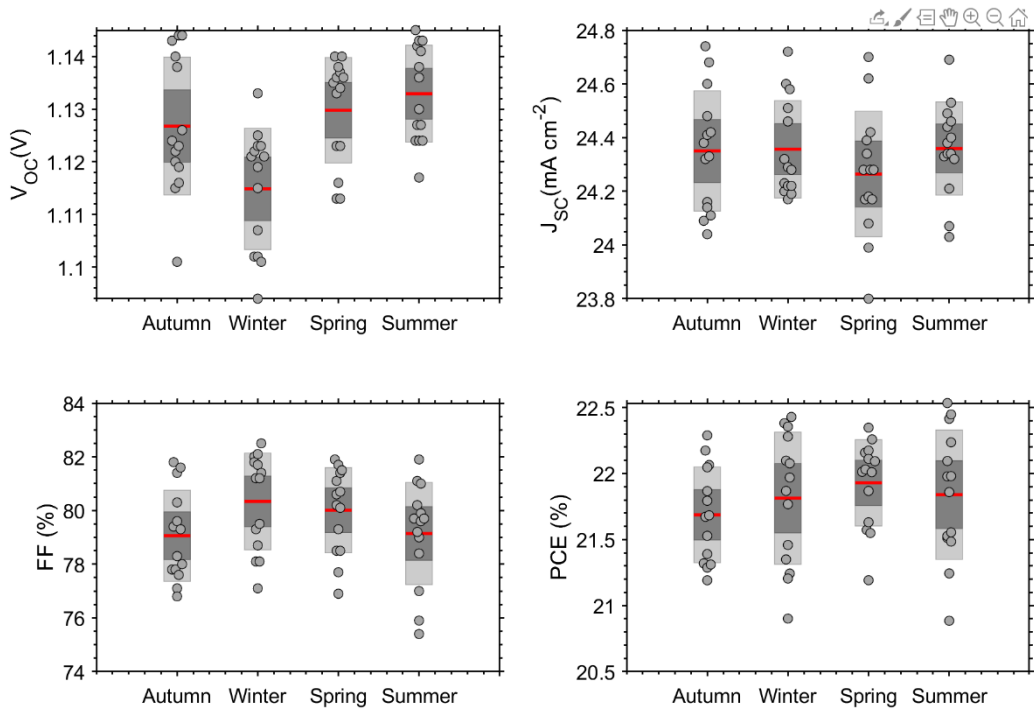
419

420 **Figure S36 | Performance statistics** for all ligands, 2D and quasi-2D treated. Taken from 10-20 devices
421 for each condition.

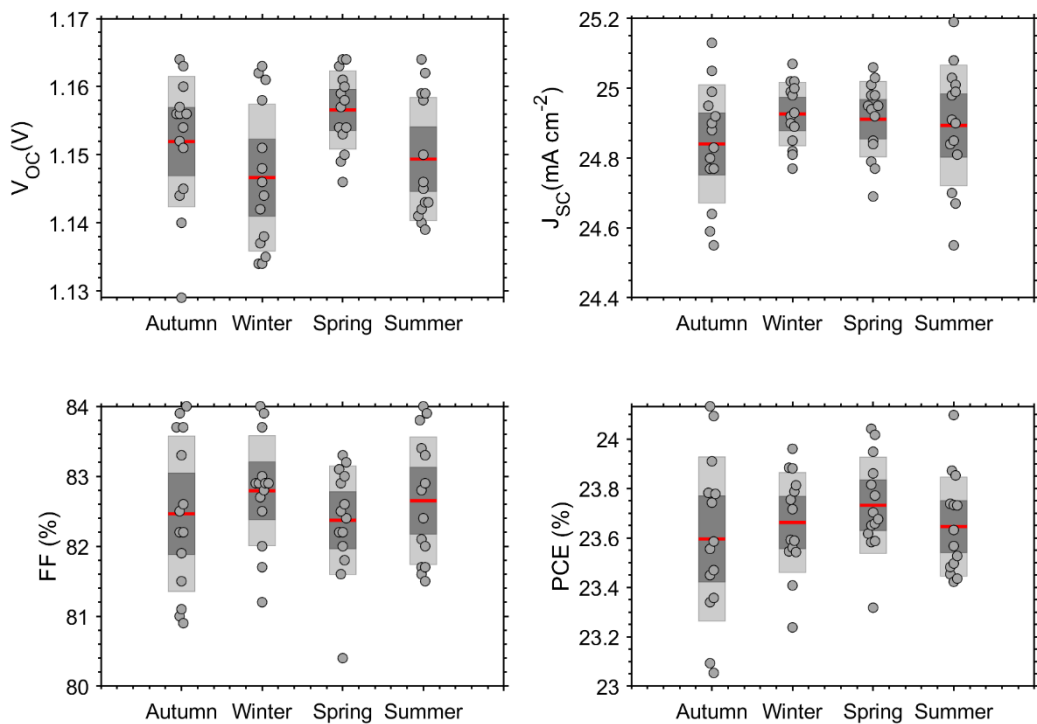
422



423 **Figure S37 | Season dependant performance statistics for control devices** across all four seasons,
 424 14 devices per batch



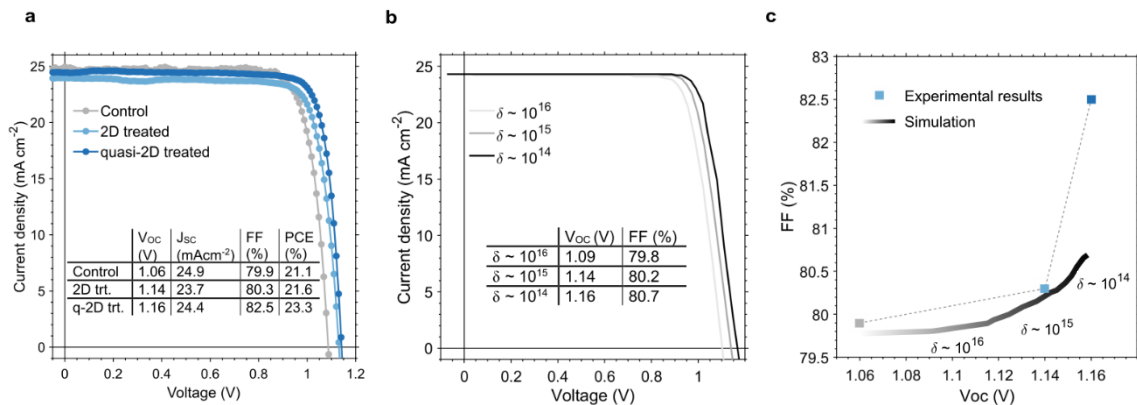
425
 426 **Figure S38 | Season dependant performance statistics for 2D treated (3F-PEA)** devices across all
 427 four seasons, 14 devices per batch.



428 **Figure S39 | Season dependant performance statistics for q-2D treated (3F-PEA) devices across**
429 **all four seasons, 14 devices per batch.**

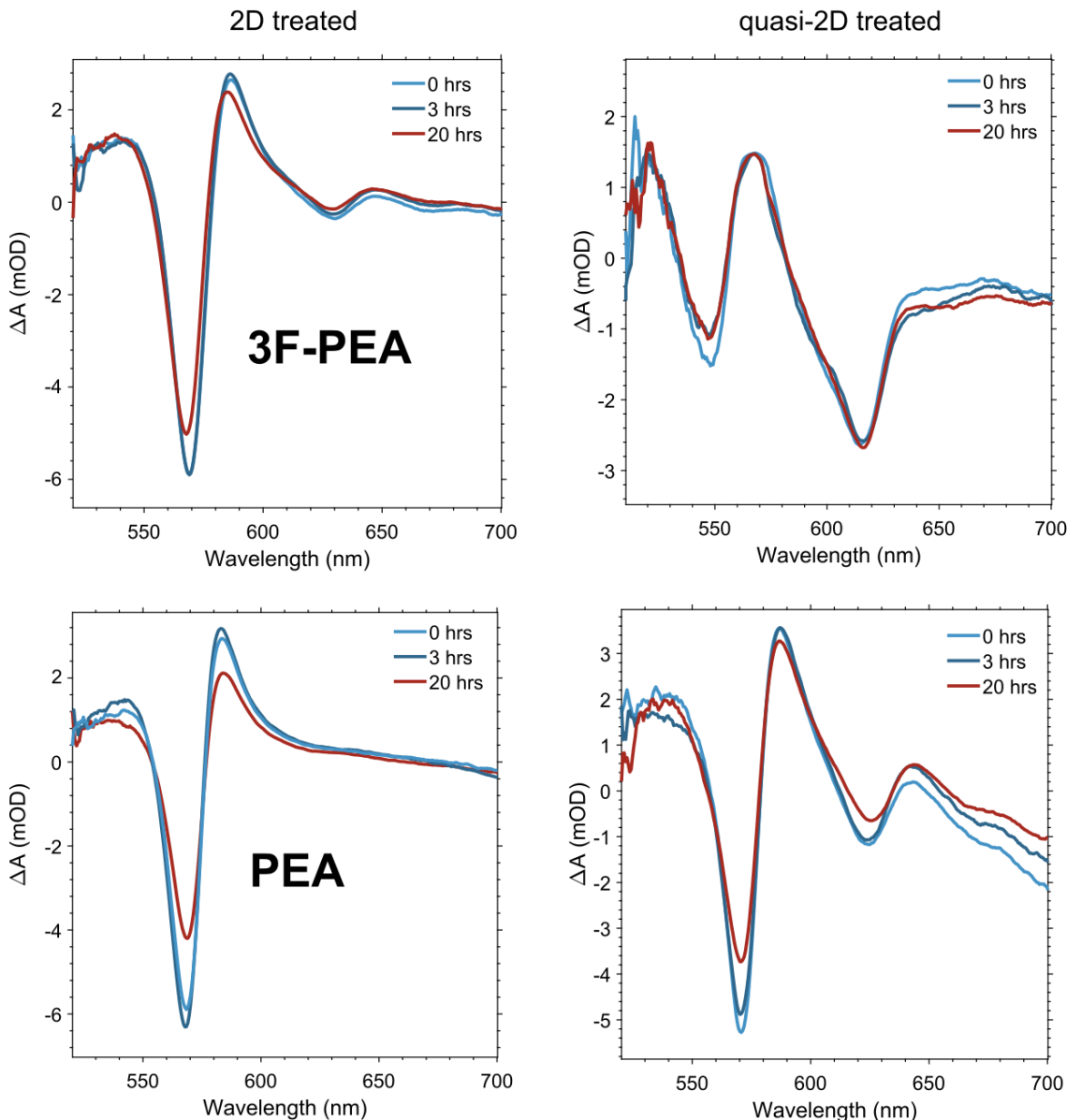
430

431



432 **Figure S40 | Comparison of experimental results and simulations.** (a) Experimental results Taken
433 from Fig 4 d). (b) Simulated $J-V$ curves varying the surface trap density (δ), (c) Comparison
434 demonstrating that the FF increase from the experimental data is unlikely to be a result of reducing δ
435 alone.

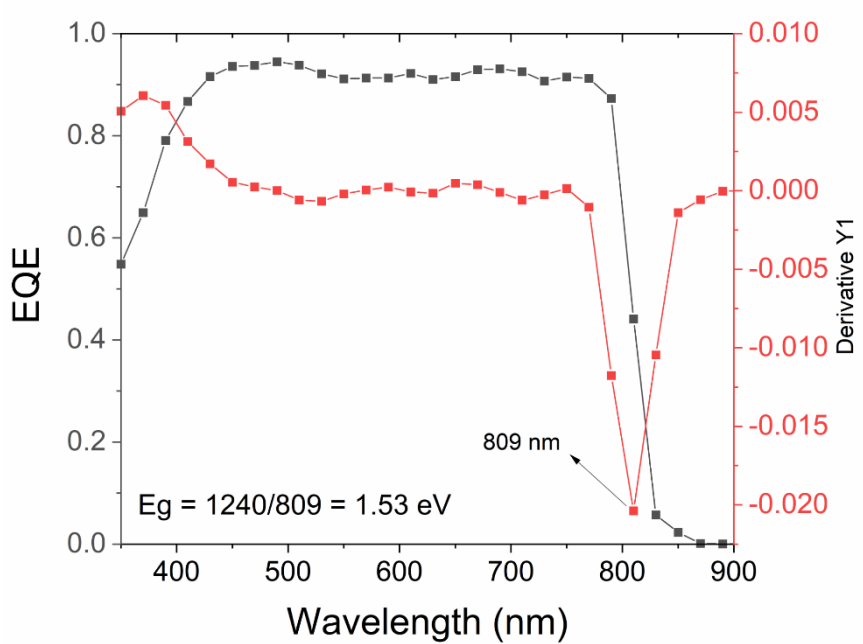
436



437

438 **Figure S41 | Stability test on 2D and quasi-2D treated films.** Each film was treated with a 2D or
 439 quasi-2D solution and then a layer of PMMA was applied atop to better simulate device conditions. A
 440 TA measurement of each film was acquired before putting the film on a hot plate in a N₂ environment
 441 at 65 °C. Additional TA spectra were recorded at 3 hrs and after 20 hours at 65 °C. Each spectra
 442 shown is at a 1 ps delay. The *n* distribution is unchanged after 20 hours for all devices and only a
 443 small change in absorption is visible, which is less obvious in the 3F-PEA treated films.

444

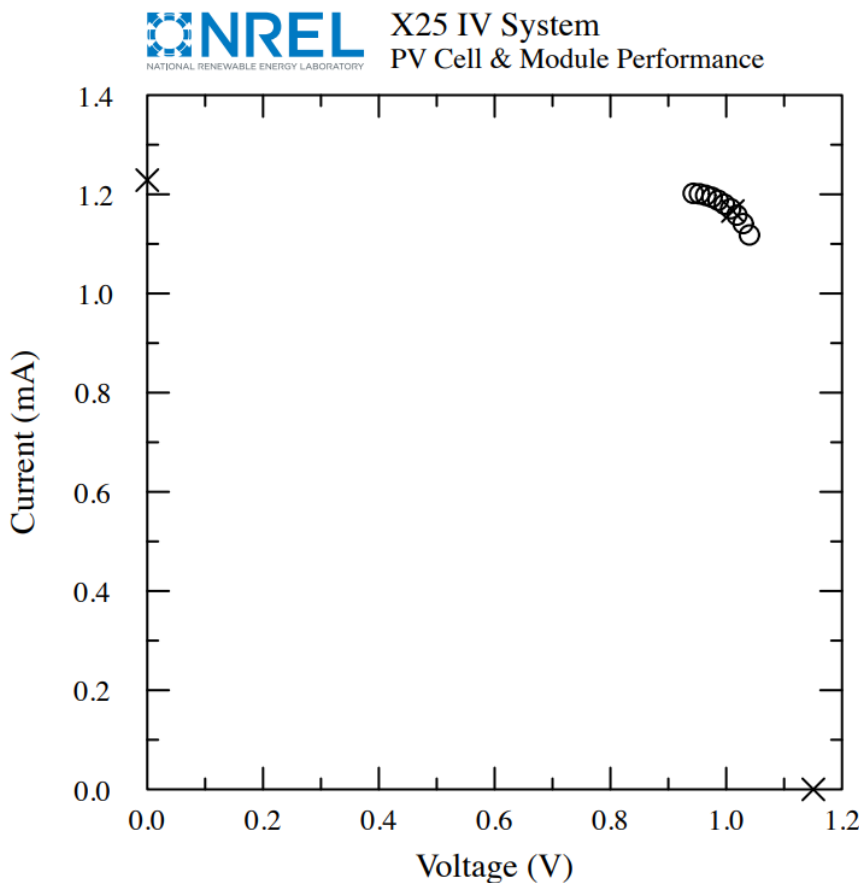


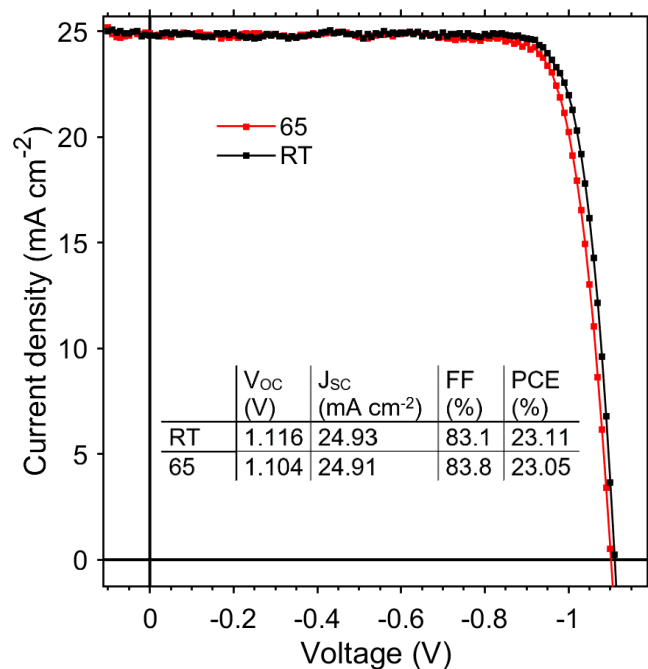
445

446 **Figure S42 | Bandgap from EQE of champion device** using the method from ³⁵ the bandgap was
 447 calculated to be 1.53 eV.

Device ID: 6
1:54 PM 7/15/2021
Spectrum: ASTM G173 global

Device temperature: 24.4 ± 0.2 °C
Device area: $0.049 \text{ cm}^2 \pm 0.4\%$
Irradiance: 1000.0 W/m^2





453

454 **Figure S44 | J-V curves and figures of merit for devices used in stability testing.** RT =
455 unencapsulated device used for room temperature MPP tracking (using the ITO/ NiO_x /Perovskite/quasi-
456 2D/PCBM/BCP structure). 65 = encapsulated device used for 65°C elevated temperature testing (using
457 the ITO/ NiO_x /Perovskite/quasi-2D/C₆₀/SnO₂ structure).

458

459

460

461

462

463

464

465

466

467

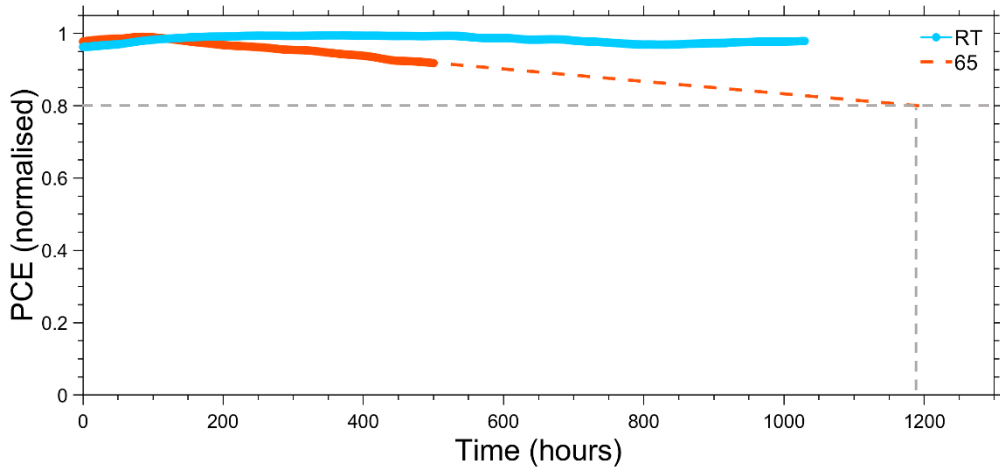
468

469

470

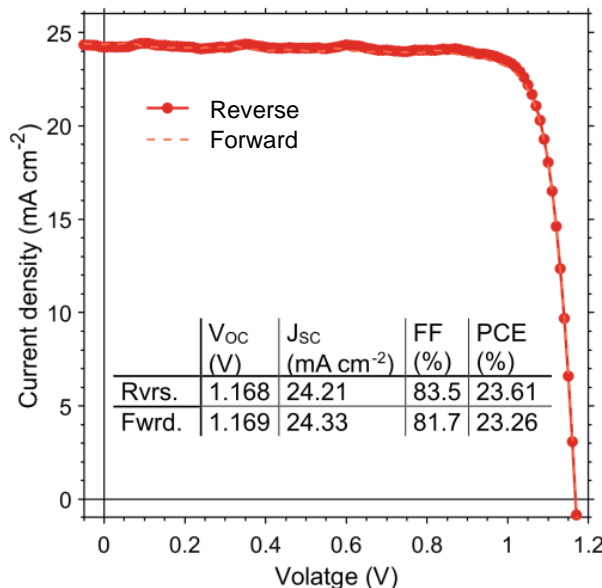
471

472



473

474 **Figure S45 | Linear extrapolation of stability testing.** Using linear extrapolation, we estimate the T₈₀
475 lifetime of our quasi-2D treated device to be ~1190hrs.



476 **Figure S46 | Forward and reverse scans of a 3F-PEAI treated device** with associated figures of
477 merit. Hysteresis is ~ 1%.

478

479 **Table S9 | Summary of reported device efficiency and stability corresponding to Figure S1.** The
 480 reported efficiency is the best certified or best reported in the paper. The stability corresponds to the
 481 most rigorous stability test undertaken. It should be noted that names with a * beside them use a different
 482 ETL and/or HTL for their stability experiments. The entries in **bold font** represent stability
 483 measurements at elevated temperature under illumination. No other report uses the full ISOS-L3
 484 protocol (controlled 65°C testing, under illuminations MPP- tracking, ~ 50% RH).

485

Name on Figure S1	Efficiency (%)	Stability	Ref.
M. Degani, Sci. Adv.	23.7	No drop in PCE after 0.5 hrs	³⁶
S. Wu, Joule (2020)	22.31	T ₉₈ = 10hrs (RT)	³⁷
F. Li, JACS (2020)	22.7 (certified)	T ₉₀ = 200hrs (RT)	³⁸
J. Xue, Science (2021)	23.0	T ₈₅ = 2000hrs (RT)	³⁹
H. Lu, Science (2020)	23.1	T ₉₀ = 500hrs (RT)	⁴⁰
J. Yoo, Nature (2021)	25.2 (certified)	T ₈₀ = 500 hrs (RT)	⁴¹
J. Jeong, Nature (2021)	25.2 (certified)	T ₈₅ = 450 hrs (RT)	⁴²
H. Min, Nature (2021)	25.5 (certified)	T ₉₀ = 500 hrs (RT)	⁴³
M. Kim, Science (2022)	25.4 (certified)	T ₈₀ = 350 hrs (RT)	⁴⁴
Y. Jeong, Science (2020)	24.64	T ₈₇ = 500hrs (RT)	⁴⁵
H. Zhu, Adv. Mat. (2020)	23.5	T ₉₅ = 1000hrs (RT)	⁴⁶
B. Park, Nature Energy (2021)	23.9	No degradation, 2000hr (RT)	⁴⁷
Z. Dai, Science (2021)	21.4	T ₉₀ = 1200hrs (RT)	⁴⁸
E.H. Jung, Nature (2019)	22.7 (certified)	T ₉₅ = 1370hrs (RT)	⁴⁹
N. Li, Science (2021)	22.3 (certified)	T ₉₅ ~ 2000 hrs (RT)	⁵⁰
H. Min, Science (2019)*	23.7 (certified)	T ₉₀ = 20hrs (150°C)	⁵¹
Q. Jiang, Nat. Photon. (2019)*	23.32 (certified)	T ₈₀ = 500hrs (85°C)	⁵²
G. Kim, Science (2020)*	24.37 (certified)	T ₈₀ = 1300hrs (85°C)	⁵³
Y. Jang, Nat. Energy (2021)*	24.35 (certified)	T ₉₄ = 1000 hrs (85°C)	⁵⁴
J. Peng, Science (2021)	23.17	T ₉₂ = 1000 hrs (85°C)	⁵⁵
X. Zheng, Nat. Energy (2020)	22.34	T ₉₀ = 1020 hrs (85°C)	⁵⁶
Q. Hu, Joule (2020)	21.0	T ₉₅ = 1000 hrs (85°C)	⁵⁷
F. Zhang, Science (2021)	24.7	T ₉₅ = 1000 hrs (RT)	⁵⁸
T. Bu, Science (2021)	23.35	T ₈₀ = 500 hrs (85°C)	⁵⁹
C. Boyd, Joule (2020)	19.67	T₈₀ = 400hrs (55°C)	⁶⁰
Y-H. Lin, Science (2020)	18.4	T₉₅ = 1200 hrs (85°C, extrapolated, post-burn in)	⁶¹
S. Bai, Nature (2019)	19.8	T₈₅ = 1885 hrs (85°C)	⁶²
Y. Wang, Science (2019)	21.08	T₉₀ = 1000 hrs (60°C)	⁶³
S. Yang, Science (2019)	21.1	T₉₇ = 1200 hrs (~65°C)	⁶⁴
S. We, Nat. Nano (2019)	21.3 (certified)	T₉₂ = 1000hrs (85°C)	⁶⁵
S. Chen, Sci Adv. (2021)	22.62 (certified)	No degradation, 1000 hrs (~65°C)	⁶⁶
X. Li, Science (2022)	23.5 (certified)	T₉₀ ~ 100 hrs (55°C)	⁶⁷
G. Yang, Nat. Photon (2021)	PIN: ~ 20%	T₉₁ = 516 hrs (60°C)	⁶⁸
This work	23.91(certified)	T₉₂ = 500 hrs (65°C)	

486

487

488

489 References

490

- 491 1. Teale, S. *et al.* Dimensional Mixing Increases the Efficiency of 2D/3D Perovskite Solar Cells.
492 *J. Phys. Chem. Lett.* 5115–5119 (2020) doi:10.1021/acs.jpclett.0c01444.
- 493 2. Stolterfoht, M. *et al.* Visualization and suppression of interfacial recombination for high-
494 efficiency large-area pin perovskite solar cells. *Nat. Energy* **3**, 847–854 (2018).
- 495 3. Burgelman, M., Nollet, P. & Degrave, S. *Modelling polycrystalline semiconductor solar cells.*
496 *Thin Solid Films* vol. 361 527–532 (Elsevier Sequoia SA, 2000).
- 497 4. Ni, Z. *et al.* Resolving spatial and energetic distributions of trap states in metal halide
498 perovskite solar cells. *Science* (80-.). **367**, 1352–1358 (2020).
- 499 5. Islam, M. N. & Hakim, M. O. Electron affinity and work function of polycrystalline SnO₂ thin
500 film. *J. Mater. Sci. Lett.* **5**, 63–65 (1986).
- 501 6. Ma, F. *et al.* Nickel oxide for inverted structure perovskite solar cells. *Journal of Energy
502 Chemistry* vol. 52 393–411 (2020).
- 503 7. Noh, J. H., Im, S. H., Heo, J. H., Mandal, T. N. & Seok, S. Il. Chemical management for
504 colorful, efficient, and stable inorganic-organic hybrid nanostructured solar cells. *Nano Lett.*
505 **13**, 1764–1769 (2013).
- 506 8. Yildirim, M. A., Yildirim, S. T., Sakar, E. F. & Ateş, A. Synthesis, characterization and
507 dielectric properties of SnO₂ thin films. *Spectrochim. Acta - Part A Mol. Biomol. Spectrosc.*
508 **133**, 60–65 (2014).
- 509 9. Brivio, F., Butler, K. T., Walsh, A. & Van Schilfgaarde, M. Relativistic quasiparticle self-
510 consistent electronic structure of hybrid halide perovskite photovoltaic absorbers. *Phys. Rev. B*
511 **89**, 155204 (2014).
- 512 10. Rao, K. V. & Smakula, A. Dielectric properties of cobalt oxide, nickel oxide, and their mixed
513 crystals. *J. Appl. Phys.* **36**, 2031–2038 (1965).
- 514 11. Button, K. J., Fonstad~, C. G. & Gang Dreybrodt, W. *PHYSICAL REVIEW B VOLUME 4,
515 NUMBER 12 15 DECEMBER 1971 Determination of the Electron Masses in Stannic Oxide
516 by Submillimeter Cyclotron Resonance.*
- 517 12. Galkowski, K. *et al.* Determination of the exciton binding energy and effective masses for
518 methylammonium and formamidinium lead tri-halide perovskite semiconductors †. *Energy
519 Environ. Sci.* **9**, 962 (2016).
- 520 13. Das, A. *et al.* Orbital hybridization-induced band offset phenomena in Ni: XCd_{1-x}O thin
521 films. *Nanoscale* **12**, 669–686 (2020).
- 522 14. Jiang, Q., Zhang, X. & You, J. SnO₂: A Wonderful Electron Transport Layer for Perovskite
523 Solar Cells. *Small* **14**, 1801154 (2018).
- 524 15. Herz, L. M. Charge-Carrier Mobilities in Metal Halide Perovskites: Fundamental Mechanisms
525 and Limits. (2017) doi:10.1021/acsenergylett.7b00276.
- 526 16. Osorio-Guillén, J., Lany, S. & Zunger, A. Nonstoichiometry and hole doping in NiO. **1199**,
527 128 (2010).
- 528 17. Sanon, G., Rup, R. & Mansingh, A. *Band-gap narrowing and band structure in degenerate tin
529 oxide (SnO₂) films. PHYSICAL REVIEW* vol. 8.
- 530 18. Madhavan, V. E. *et al.* CuSCN as Hole Transport Material with 3D/2D Perovskite Solar Cells.
531 *ACS Appl. Energy Mater.* **3**, 114–121 (2020).
- 532 19. Ravishankar, S., Unold, T. & Kirchartz, T. Comment on “Resolving spatial and energetic
533 distributions of trap states in metal halide perovskite solar cells”. *arXiv* vol. 367 97–100

- 534 (2020).
- 535 20. He, T. *et al.* Reduced-dimensional perovskite photovoltaics with homogeneous energy
536 landscape. *Nat. Commun.* **11**, 1–11 (2020).
- 537 21. Yoshida, H. Near-ultraviolet inverse photoemission spectroscopy using ultra-low energy
538 electrons. *Chem. Phys. Lett.* **539–540**, 180–185 (2012).
- 539 22. Boehm, A. M., Wieser, J., Butrouna, K. & Graham, K. R. A new photon source for ultraviolet
540 photoelectron spectroscopy of organic and other damage-prone materials. *Org. Electron.* **41**,
541 9–16 (2017).
- 542 23. Endres, J. *et al.* Valence and Conduction Band Densities of States of Metal Halide Perovskites:
543 A Combined Experimental-Theoretical Study. *J. Phys. Chem. Lett.* **7**, 2722–2729 (2016).
- 544 24. Blum, V. *et al.* Ab initio molecular simulations with numeric atom-centered orbitals. *Comput.
545 Phys. Commun.* **180**, 2175–2196 (2009).
- 546 25. Havu, V., Blum, V., Havu, P. & Scheffler, M. Efficient O δ NP integration for all-electron
547 electronic structure calculation using numeric basis functions. *J. Comput. Phys.* **228**, 8367–
548 8379 (2009).
- 549 26. Ren, X. *et al.* Resolution-of-identity approach to Hartree–Fock, hybrid density functionals,
550 RPA, MP2 and GW with numeric atom-centered orbital basis functions. *New J. Phys.* **14**,
551 053020 (2012).
- 552 27. Perdew, J. P., Burke, K. & Ernzerhof, M. Generalized Gradient Approximation Made Simple.
553 *Phys. Rev. Lett.* **77**, 3865 (1996).
- 554 28. A, T. & M, S. Accurate molecular van der Waals interactions from ground-state electron
555 density and free-atom reference data. *Phys. Rev. Lett.* **102**, (2009).
- 556 29. Stoumpos, C. C. *et al.* Ruddlesden–Popper Hybrid Lead Iodide Perovskite 2D Homologous
557 Semiconductors. *Chem. Mater.* **28**, 2852–2867 (2016).
- 558 30. Hu, J. *et al.* Synthetic control over orientational degeneracy of spacer cations enhances solar
559 cell efficiency in two-dimensional perovskites. *Nat. Commun.* **10**, 1–11 (2019).
- 560 31. Hoffman, C. A., Jarašiūnas, K., Gerritsen, H. J. & Nurmikko, A. V. Measurement of surface
561 recombination velocity in semiconductors by diffraction from picosecond transient free-carrier
562 gratings. *Appl. Phys. Lett.* **33**, 536 (2008).
- 563 32. Tanaka, T., Harata, A. & Sawada, T. Subpicosecond surface-restricted carrier and thermal
564 dynamics by transient reflectivity measurements. *J. Appl. Phys.* **82**, 4033 (1998).
- 565 33. Yang, Y. *et al.* Top and bottom surfaces limit carrier lifetime in lead iodide perovskite films.
566 *Nat. Energy* **2**, (2017).
- 567 34. Y, Y. *et al.* Low surface recombination velocity in solution-grown CH₃NH₃PbBr₃ perovskite
568 single crystal. *Nat. Commun.* **6**, (2015).
- 569 35. Nayak, P. K., Mahesh, S., Snaith, H. J. & Cahen, D. Photovoltaic solar cell technologies:
570 analysing the state of the art. *Nat. Rev. Mater.* **2019 44** **4**, 269–285 (2019).
- 571 36. Degani, M. *et al.* 23.7% Efficient inverted perovskite solar cells by dual interfacial
572 modification. *Sci. Adv.* **7**, 7930 (2021).
- 573 37. Wu, S. *et al.* Modulation of Defects and Interfaces through Alkylammonium Interlayer for
574 Efficient Inverted Perovskite Solar Cells. *Joule* **4**, 1248–1262 (2020).
- 575 38. Li, F. *et al.* Regulating Surface Termination for Efficient Inverted Perovskite Solar Cells with
576 Greater Than 23% Efficiency. *J. Am. Chem. Soc.* **142**, 20134–20142 (2020).

- 577 39. Xue, J. *et al.* Reconfiguring the band-edge states of photovoltaic perovskites by conjugated
578 organic cations. *Science* (80-.). **371**, 636–640 (2021).
- 579 40. Lu, H. *et al.* Vapor-assisted deposition of highly efficient, stable black-phase FAPbI₃
580 perovskite solar cells. *Science* (80-.). **370**, (2020).
- 581 41. Yoo, J. J. *et al.* Efficient perovskite solar cells via improved carrier management. *Nature* **590**,
582 587–593 (2021).
- 583 42. Jeong, J. *et al.* Pseudo-halide anion engineering for α -FAPbI₃ perovskite solar cells. *Nature*
584 **592**, 381 (2021).
- 585 43. Min, H. *et al.* Perovskite solar cells with atomically coherent interlayers on SnO₂ electrodes.
586 *Nature* **598**, 444–450 (2021).
- 587 44. Kim, M. *et al.* Conformal quantum dot-SnO₂ layers as electron transporters for efficient
588 perovskite solar cells. *Science* (80-.). **375**, 302–306 (2022).
- 589 45. Jeong, M. *et al.* Stable perovskite solar cells with efficiency exceeding 24.8% and 0.3-V
590 voltage loss. *Science* (80-.). **369**, 1615–1620 (2020).
- 591 46. Zhu, H. *et al.* Tailored Amphiphilic Molecular Mitigators for Stable Perovskite Solar Cells
592 with 23.5% Efficiency. *Adv. Mater.* **32**, 1907757 (2020).
- 593 47. Park, B. *et al.* Stabilization of formamidinium lead triiodide α -phase with isopropylammonium
594 chloride for perovskite solar cells. *Nat. Energy* **6**, 419–428 (2021).
- 595 48. Dai, Z. *et al.* Interfacial toughening with self-assembled monolayers enhances perovskite solar
596 cell reliability. *Science* (80-.). **372**, 618–622 (2021).
- 597 49. Jung, E. H. *et al.* Efficient, stable and scalable perovskite solar cells using poly(3-
598 hexylthiophene). *Nature* **567**, 511–515 (2019).
- 599 50. Li, N. *et al.* Liquid medium annealing for fabricating durable perovskite solar cells with
600 improved reproducibility. *Science* (80-.). **373**, 561–567 (2021).
- 601 51. Min, H. *et al.* Efficient, stable solar cells by using inherent bandgap of a-phase formamidinium
602 lead iodide. *Science* (80-.). **366**, 749–753 (2019).
- 603 52. Jiang, Q. *et al.* Surface passivation of perovskite film for efficient solar cells. *Nat. Photonics*
604 **13**, 460–466 (2019).
- 605 53. Kim, G. *et al.* Impact of strain relaxation on performance of a-formamidinium lead iodide
606 perovskite solar cells. *Science* (80-.). **370**, 108–112 (2020).
- 607 54. Jang, Y. W. *et al.* Intact 2D/3D halide junction perovskite solar cells via solid-phase in-plane
608 growth. *Nat. Energy* **6**, 63–71 (2021).
- 609 55. Peng, J. *et al.* Nanoscale localized contacts for high fill factors in polymer-passivated
610 perovskite solar cells. *Science* (80-.). **371**, 390–395 (2021).
- 611 56. Zheng, X. *et al.* Managing grains and interfaces via ligand anchoring enables 22.3%-efficiency
612 inverted perovskite solar cells. *Nat. Energy* **5**, 131–140 (2020).
- 613 57. Hu, Q. *et al.* Improving Efficiency and Stability of Perovskite Solar Cells Enabled by A Near-
614 Infrared-Absorbing Moisture Barrier. *Joule* **4**, 1575–1593 (2020).
- 615 58. Zhang, F. *et al.* Metastable Dion-Jacobson 2D structure enables efficient and stable perovskite
616 solar cells. *Science* (80-.). **375**, 71–76 (2022).
- 617 59. Bu, T. *et al.* Lead halide-templated crystallization of methylamine-free perovskite for efficient
618 photovoltaic modules. *Science* (80-.). **372**, 1327–1332 (2021).

- 619 60. Boyd, C. C. *et al.* Overcoming Redox Reactions at Perovskite-Nickel Oxide Interfaces to
620 Boost Voltages in Perovskite Solar Cells. *Joule* **4**, 1759–1775 (2020).
- 621 61. Lin, Y. H. *et al.* A piperidinium salt stabilizes efficient metal-halide perovskite solar cells.
622 *Science (80-)*. **369**, 96–102 (2020).
- 623 62. Bai, S. *et al.* Planar perovskite solar cells with long-term stability using ionic liquid additives.
624 *Nature* **571**, 245–250 (2019).
- 625 63. Wang, Y. *et al.* Stabilizing heterostructures of soft perovskite semiconductors. *Science (80-)*.
626 **365**, 687–691 (2019).
- 627 64. Yang, S. *et al.* Stabilizing halide perovskite surfaces for solar cell operation with wide-
628 bandgap lead oxysalts. *Science (80-)*. **365**, 473–478 (2019).
- 629 65. Wu, S. *et al.* 2D metal–organic framework for stable perovskite solar cells with minimized
630 lead leakage. *Nat. Nanotechnol.* **15**, 934–940 (2020).
- 631 66. Chen, S., Xiao, X., Gu, H. & Huang, J. Iodine reduction for reproducible and high-
632 performance perovskite solar cells and modules. *Sci. Adv.* **7**, eabe8130 (2021).
- 633 67. Li, X. *et al.* Constructing heterojunctions by surface sulfidation for efficient inverted
634 perovskite solar cells. *Science (80-)*. **375**, 434–437 (2022).
- 635 68. Yang, G. *et al.* Stable and low-photovoltage-loss perovskite solar cells by multifunctional
636 passivation. *Nat. Photonics* **2021** 1–9 (2021) doi:10.1038/s41566-021-00829-4.

637



Quantum-size-tuned heterostructures enable efficient and stable inverted perovskite solar cells

Hao Chen^{1,2,7}, Sam Teale^{1,7}, Bin Chen^{1,7}, Yi Hou^{1,6,7}, Luke Grater¹, Tong Zhu¹, Koen Bertens¹, So Min Park^{1,3}, Harindi R. Atapattu³, Yajun Gao⁴, Mingyang Wei¹, Andrew K. Johnston^{1,7}, Qilin Zhou^{1,2}, Kaimin Xu², Danni Yu², Congcong Han², Teng Cui⁵, Eui Hyuk Jung^{1,7}, Chun Zhou^{1,7}, Wenjia Zhou^{1,2}, Andrew H. Proppe¹, Sjoerd Hoogland¹, Frédéric Laquai^{1,4}, Tobin Fillete⁵, Kenneth R. Graham³, Zhijun Ning^{1,2,✉} and Edward H. Sargent^{1,7}

The energy landscape of reduced-dimensional perovskites (RDPs) can be tailored by adjusting their layer width (n). Recently, two/three-dimensional (2D/3D) heterostructures containing $n=1$ and 2 RDPs have produced perovskite solar cells (PSCs) with >25% power conversion efficiency (PCE). Unfortunately, this method does not translate to inverted PSCs due to electron blocking at the 2D/3D interface. Here we report a method to increase the layer width of RDPs in 2D/3D heterostructures to address this problem. We discover that bulkier organics form 2D heterostructures more slowly, resulting in wider RDPs; and that small modifications to ligand design induce preferential growth of $n \geq 3$ RDPs. Leveraging these insights, we developed efficient inverted PSCs (with a certified quasi-steady-state PCE of 23.91%). Unencapsulated devices operate at room temperature and around 50% relative humidity for over 1,000 h without loss of PCE; and, when subjected to ISOS-L3 accelerated ageing, encapsulated devices retain 92% of initial PCE after 500 h.

Reduced-dimensional perovskites are perovskite quantum well (QW) layers confined between large organic ligands. The number of stacked lead (Pb) octahedra between the organic spacers determines the width of the RDP layer: $n = 1, 2, 3$ and so on (Fig. 1a). Changing the RDP layer width (n) within bulk RDP films alters the energy landscape of the resulting material, hence narrow RDP films ($n \leq 5$) produce excellent light-emitting diodes (LEDs) and luminescent solar concentrators^{1,2}. Although films containing wider RDPs ($n \geq 10$) have been used to produce highly stable PSCs, these devices suffer from an inferior performance due to poor carrier mobility^{3,4}. More recently, record-performing PSCs have used a 2D/3D heterostructure, fabricated via spin coating RDP (or 2D) ligands onto the surface of a 3D perovskite^{5–12}. A comparison of PSC efficiency/stability from recent reports is shown in Supplementary Fig. 1 and demonstrates that all of the most efficient devices reported have used this structure. Studies have revealed that this heterostructure consists of a thin layer of $n=1$ and/or $n=2$ RDPs atop a bulk 3D perovskite^{13–16}, which increases performance via passivation and increased electron blocking^{17,18}. Electron blocking is beneficial for devices built in the negative–intrinsic–positive (NIP) architecture, in which the 2D-treated perovskite surface is coated with a hole transport layer (HTL); however, when used in the generally more stable^{19–22} inverted (that is, positive–intrinsic–negative, or PIN) structure, this strategy achieves mixed results. Chen et al. found that a 2D treatment applied to inverted cells improved the open-circuit voltage (V_{OC}) but reduced the fill factor (FF)²³, and Bai et al. found that introducing a small amount of 2D ligand into the

antisolvent improved the device performance, opening the door to further study of the width of RDPs and indeed their presence²⁴. On the other hand, Park et al., La-Placa et al. and Zhao et al. all found that using a 2D layer in a PIN device reduced the PCE due to a lower current and fill factor^{25–27}. We speculated that reducing the confinement in the 2D layer could reduce electron blocking and produce inverted PSCs with an exceptional performance.

A quasi-2D surface treatment

Using ultraviolet photoelectron spectroscopy (UPS) and absorption spectroscopy, we estimated the band alignment of RDP films of differing QW widths ($n = 1–4$; Fig. 1b) and compared them with the bulk 3D perovskite $\text{Cs}_{0.05}\text{MA}_{0.1}\text{FA}_{0.85}\text{PbI}_3$ (MA, methylammonium; FA, formamidinium). Consistent with earlier reports, we found little dependence between the valence band maximum (VBM) and n (RDP width)^{18,28,29}. Instead, quantum confinement upshifts the conduction band minimum (CBM), which induces electron blocking in the devices. We confirmed this detrimental effect by comparing NIP and PIN PSCs treated using standard 2D treatments (Supplementary Text 1). Encouragingly, simulations using the solar cell simulation tool SCAPS-1D³⁰ suggested that, due to their deeper CBM, a capping layer of $n \geq 3$ RDPs would be beneficial for PIN solar cell performance via surface passivation with reduced resistance to carrier transport (Supplementary Text 2).

In bulk RDP films, the average layer thickness is modulated by changing the ratio of the 2D ligands to the 3D perovskite precursors in solution^{1,4}. We explored several options to reproduce this

¹The Edward S. Rogers Department of Electrical and Computer Engineering, University of Toronto, Toronto, Ontario, Canada. ²School of Physical Science and Technology, ShanghaiTech University, Shanghai, China. ³Department of Chemistry, University of Kentucky, Lexington, KY, USA. ⁴KAUST Solar Center, Physical Sciences and Engineering Division (PSE), Materials Science and Engineering Program (MSE), King Abdullah University of Science and Technology (KAUST), Thuwal, Kingdom of Saudi Arabia. ⁵Department of Mechanical and Industrial Engineering, University of Toronto, Toronto, Ontario, Canada. ⁶Present address: Department of Chemical and Biomolecular Engineering, National University of Singapore, Singapore, Singapore. ⁷These authors contributed equally: Hao Chen, Sam Teale, Bin Chen, Yi Hou. ✉e-mail: ningzhj@shanghaitech.edu.cn; ted.sargent@utoronto.ca

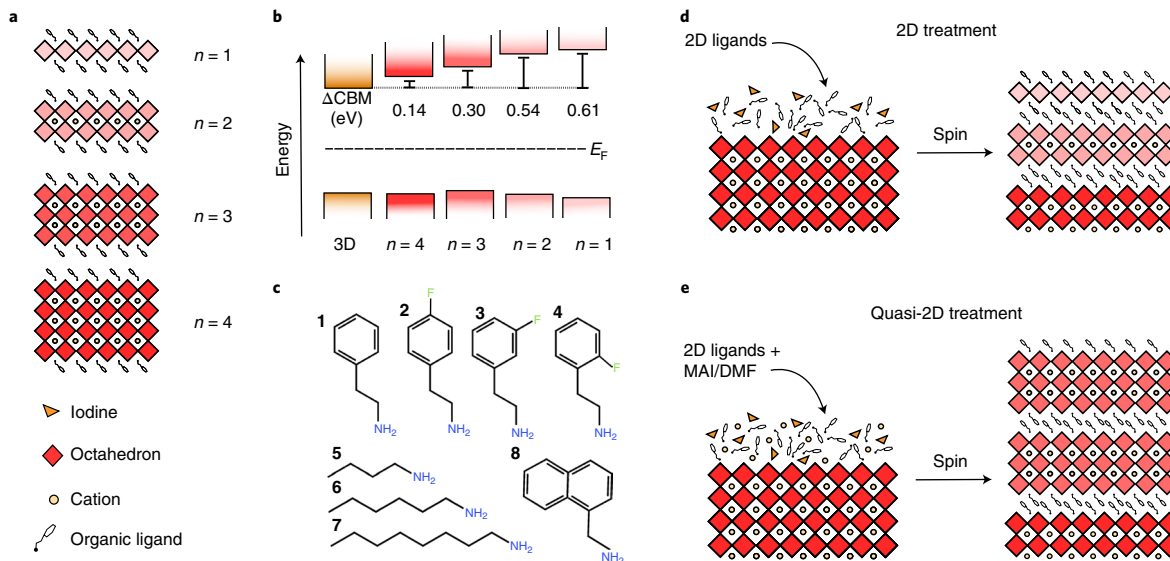


Fig. 1 | Quasi-2D treatment and its effect on RDP distribution. **a**, Schematic of $n=1, 2, 3$ and 4 RDPs. **b**, Band alignment of 3D and RDP films with increasing confinement calculated from UPS and the optical bandgap of quasi-2D perovskite films. **c**, The eight ligands used in the study: **1**, phenethylammonium; **2**, 4-fluoro-phenethylammonium; **3**, 3-fluoro-phenethylammonium; **4**, 2-fluoro-phenethylammonium; **5**, butylammonium; **6**, hexylammonium; **7**, octylammonium; and **8**, 1-naphthylmethylammonium. **d,e**, Schematics of the standard 2D treatment (**d**) and the quasi-2D treatment (**e**) producing $n \leq 2$ RDPs and $n \geq 2$ RDPs, respectively.

for a 2D post-treatment (Supplementary Text 3). Our most distinctive results came from introducing a small amount of dimethylformamide (DMF) (at 1:200 by volume in isopropanol (IPA)) and methylammonium iodide (MAI) (1:2 by weight) to the 2D ligands in solution. We posit that MAI is needed to reduce the ratio of the 2D ligand to the A-site cation and that DMF introduces Pb directly from the 3D perovskite surface (Supplementary Fig. 9). Using this strategy, we were able to produce 2D perovskite capping layers containing $n \geq 3$ RDP layers (Fig. 1e). For convenience, we henceforth refer to our altered 2D ligand treatment as a quasi-2D treatment.

Notably, Zhou et al. demonstrated that adding MAI and DMF to a phenethylammonium iodide (PEAI) surface treatment improves the performance of PIN solar cells³¹. This earlier study is limited in scope, however, discussing only the effect of DMF on the penetration depth of the 2D treatment. Using time-of-flight secondary-ion mass spectrometry, we estimated the penetration depth of phenethylammonium (PEA) from solutions using different DMF concentrations (Supplementary Fig. 11) and found no correlation in our sample size (from 1:200 to 1:50 DMF:IPA by volume). We instead expect that the origin of improved performance is the production of wider RDPs at the interface between the 3D perovskite and the electron transporting layer (ETL). Considering this new observation, we sought a treatment that would optimize this effect.

Characterizing the quantum well width in 2D/3D heterojunctions

A strong dependence between QW width and bandgap exists in 2D perovskites^{32,33}. Hence, ultrafast transient absorption (TA) spectroscopy is able to accurately identify the distribution of different 2D species in perovskite films^{34–36}. We first acquired the TA spectra of 2D- and quasi-2D-treated films using the most common 2D perovskite ligands: butylammonium (BTA) (Fig. 2a,d) and PEA (Fig. 2b,e). Although the majority absorption from each film is from the 3D perovskite (780 nm, Supplementary Fig. 12), each film displays bleach peaks in the 500–700 nm range, characteristic of RDPs. Similar to spectra acquired by Niu et al., the standard 2D-treated films display bleach signals from $n=1$ and/or 2 RDPs³⁶.

Quasi-2D-treated films, however, contain $n \geq 3$ RDPs, with the PEA treatment producing more $n \geq 3$ RDPs than BTA. Grazing incidence wide-angle X-ray scattering (GIWAXS) confirmed that these 2D layers lie horizontal to the substrate (Supplementary Fig. 13), as in other reports^{5,13,15}. Recently, it was documented that bulk quasi-2D perovskite films made using fluorinated PEA ligands form different QW structures compared to unfluorinated PEA³⁵. To this end, we tested PEA-based ligands with a fluorine at each node (Fig. 1c) and found that this has a dramatic effect on the QW distribution (Supplementary Fig. 16). Mostly notably, we found that using our quasi-2D surface strategy, 3-fluoro-phenethylammonium (3F-PEA) produces a 2D/3D heterojunction containing majority $n=3$ RDP (Fig. 2f). The structures of all 2D ligands mentioned are shown in Fig. 1c.

To better understand why different ligands produce different RDP distributions, we measured TA spectra *in situ* while spin coating quasi-2D treatments (Fig. 2g–i). With a pump–probe delay of 1 ps and a time resolution of 0.3 s, we spun films at 1,500 revolutions per minute (r.p.m.) and deposited the 2D treatment dynamically. A reduction in the 3D perovskite absorption is apparent ~2.4 s after solution deposition for all samples. For the BTA treatment, this reduction in 3D bleach is concurrent with the arrival of a strong $n=2$ bleach. For the PEA-based treatments, the 2D signal does not appear until ~1.2 s after the 3D bleach reduction. It has been suggested that bulkier organics intercalate more slowly, which induces them to form wider RDPs³⁴. Our results agree, indicating that π - π stacking ligands form wider RDPs due to slower crystallization, which suppresses narrower RDP formation. This is corroborated by films treated using hexylammonium (HA) and octylammonium (OTA) ligands, which demonstrate an increased presence of $n \geq 3$ RDP with increasing ligand length (Supplementary Fig. 14). To investigate the effect of increased π - π stacking, we treated samples with 1-naphthylmethylammonium (Fig. 1c) but found that the quasi-2D treatment substantially reduced the RDP absorption in the TA spectra (Supplementary Fig. 15). We also gained insight into why 3F-PEA forms wider RDPs. Standard PEA produces $n=2$ and 3 simultaneously, whereas 3F-PEA forms $n=3$

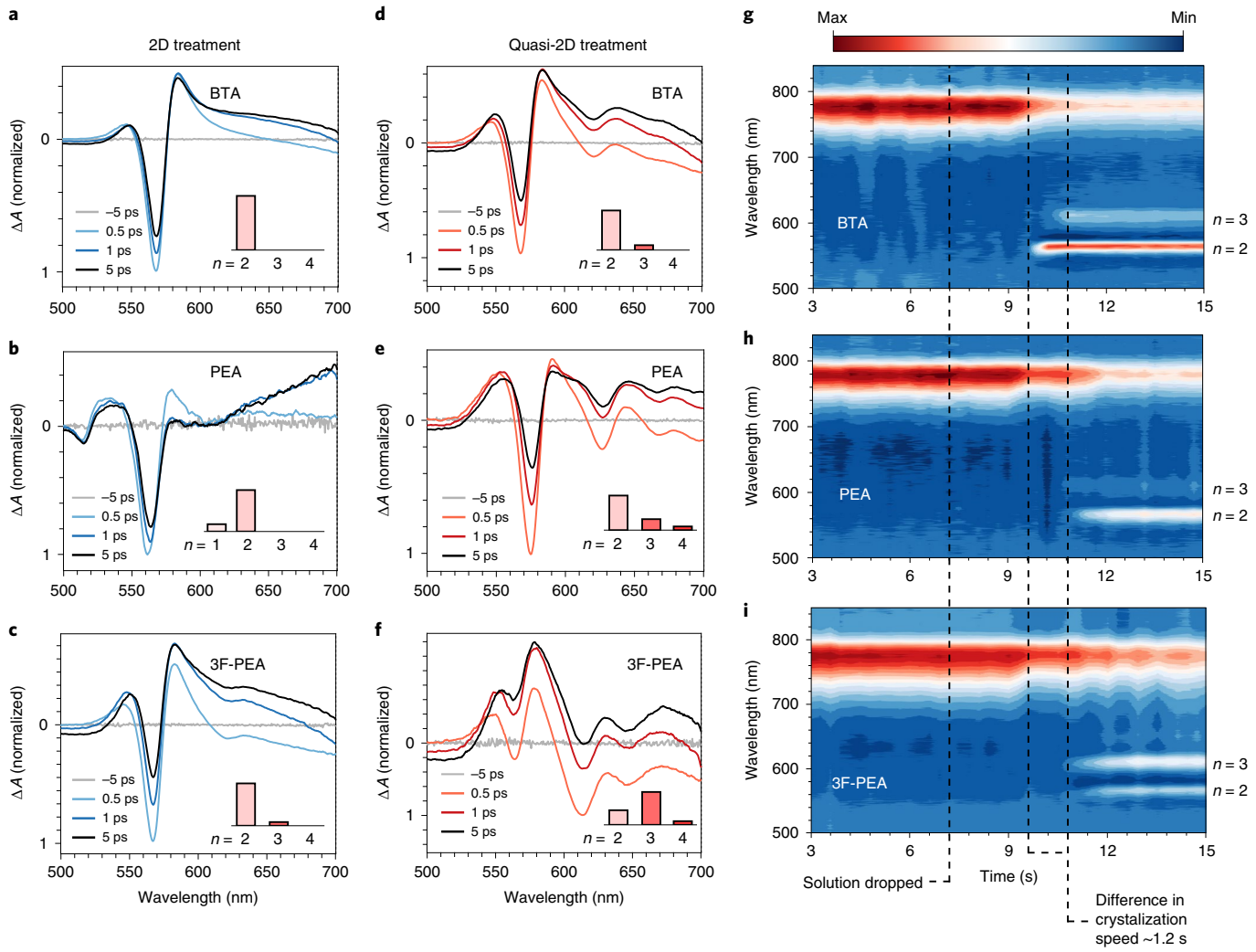


Fig. 2 | Comparison of 2D and quasi-2D treatments using different 2D ligands. **a–c**, TA spectra of films treated with BTA (**a**), PEA (**b**) and 3F-PEA (**c**) using the standard 2D treatment. **d–f**, TA spectra of films treated with BTA (**d**), PEA (**e**) and 3F-PEA (**f**) using the quasi-2D treatment. The majority absorption in each case is from the 3D perovskite (780 nm) but this has been excluded for clarity. Absorption peaks are assigned in order, and a comparison with single-cation quasi-2D films is shown in Supplementary Table 4. The inset bar in **a–f** represents the relative absorption from each RDP species. **g–h**, Absorption maps from in situ TA spectroscopy obtained during spin coating. $\text{Cs}_{0.05}\text{MA}_{0.1}\text{FA}_{0.85}\text{PbI}_3$ 3D perovskite films were spun at 1,500 r.p.m. and a constant 1 ps pump-probe delay time was used. The quasi-2D treatments for BTA (**g**), PEA (**h**) and 3F-PEA (**i**) were all dropped at 7.2 s.

one frame (0.3 s) before the appearance of $n=2$, suggesting that $n=3$ is preferentially formed from the precursor complex.

Density functional theory (DFT) calculations were used to compute the formation energy of $n=1, 2, 3$ and 4 RDPs for each ligand (details in Supplementary Text 5). As previously reported⁴, the formation energy of the $n=1$ RDP was found to be the lowest for all ligands; however, this was not supported by our experimental findings or results from other studies^{36,37}. Nonetheless, considering that forming single layers of lead iodide (PbI_2) is considerably more energy intensive than larger slabs (Fig. 3a) it seems reasonable that $n=1$ layers are less likely to form, especially when excess cations are available as within the quasi-2D treatment. Hence, we compared the formation energy of $n \geq 2$ RDPs. Generally, we found that formation energy increases with increasing width, however, we also found that bonding different ligands onto 2D perovskite flakes ($\text{FA}_{n-1}\text{Pb}_n\text{I}_{3n-1}$) introduces different types of strain into the system which is released through different distortions of the perovskite (Supplementary Fig. 22). The specific orientation and arrangement of the ligands caused by the fluorine atom in 3F-PEA (structure taken from³⁵) introduces larger strain compared to PEA or BTA, manifesting as

larger distortions, and therefore larger perovskite flakes are needed to fully release the additional strain. As a result, a sweet spot for $n=3$ is found in the formation energy of 3F-PEA (Fig. 3b), which results in the preferential formation of $n=3$ revealed in the TA data. We calculated the formation energies for each of the ligands 1–7 in Fig. 1c (Supplementary Fig. 21, Supplementary Text 5), but only 3F-PEA possessed a preference for $n \geq 3$.

Band alignment of 2D/3D heterostructures

We proposed to modulate the n distribution of 2D/3D heterojunctions with the aim of reducing the electron barrier at the perovskite/ETL interface. To verify this, we used surface-sensitive inverse photoelectron spectroscopy (IPES), which directly measures the conduction band of the first few nanometres of film^{29,38–41}. Following work from Endres et al.⁴² we used gaussian fittings to extract the CBM and found that, as expected, the CBM values of 2D-treated surfaces are upshifted compared with the controls (Fig. 4a–c). Using the quasi-2D treatment the 2D/3D CBM offset is reduced substantially for PEA- and 3F-PEA-treated films relative to their $n=1$ (and/or 2) analogues (0.42–0.14 eV and 0.49–0.08 eV, respectively)

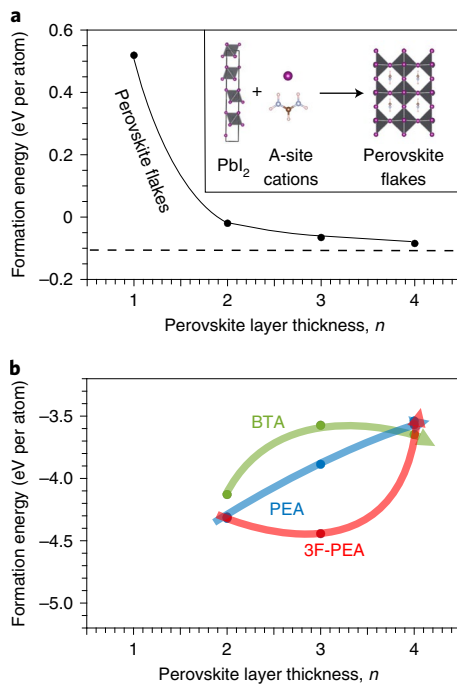


Fig. 3 | Formation of quasi-2D perovskite capping layers from density functional theory. **a**, The PBE+TS calculated formation energy of perovskite flakes ($(FA)_{n-1}Pb_nI_{3n-1}$, see inset). The formation energy of $FAPb_3$ is shown as a dashed line. Note that the energy required to form a single-layer (PbI_2) flake ($n=1$ RDP) is much higher than for other layer widths. PBE+TS, Perdew-Burke-Ernzerhof functional with the Tkatchenko-Scheffler dispersion correction. **b**, The formation energy of different RDPs dependent on the layer width n and the ligand (BTA, PEA and 3F-PEA). The same calculations were performed on HA, OTA, 2F-PEA and 4F-PEA and can be found in Supplementary Fig. 21.

but less so for BTA (0.41–0.31 eV). We measured the potential of our film surfaces using Kelvin probe force microscopy (KPFM) and found a similar trend (Supplementary Fig. 17). This complements the results in the previous section which suggest that the quasi-2D treatment using BTA produces fewer $n \geq 3$ RDPs than PEA or 3F-PEA. We also performed surface-sensitive UPS on control, 2D- and quasi-2D-treated films (Supplementary Fig. 18) to produce the schematics in Fig. 4e,f. Similar to the plot in Fig. 1b and several previous reports^{18,28,29}, altering the RDP width has little effect on the VBM, and reducing confinement simply shifts the conduction band deeper, closer to the 3D perovskite. More details on these UPS and IPES measurements can be found in Supplementary Text 4.

Carrier extraction and photovoltaic performance

To explore the device implications, we investigated the charge transport in BTA-, PEA- and 3F-PEA-treated films using the 2D and quasi-2D treatments. The photoluminescence quantum yield (PLQY) increases after the standard 2D treatment for each ligand (Supplementary Table 6), suggesting a reduced density of non-radiative recombination centres⁸. This effect is enhanced slightly by the quasi-2D treatment, indicating improved passivation. A similar trend is visible in transient photoluminescence (TRPL) spectroscopy results (Fig. 5a and Supplementary Fig. 24), where longer lifetimes are recorded for 2D- and quasi-2D-treated films (a summary of lifetimes is found in Supplementary Table 3). The modestly improved passivation of the quasi-2D treatment may be due to the addition of MAI, which has also been reported to passivate perovskite surfaces⁴³.

Following the work of Kirchartz et al., we deposited [6,6]-phenyl-C₆₁-butyric acid methyl ester (PCBM) atop the perovskite as an ETL and used the quenched τ_i lifetimes to compare charge extraction (Fig. 5b)⁴⁴. The quenched τ_i lifetime of the control film was 4.6 ns. After deposition of 3F-PEA this doubled to 9.2 ns, suggesting that the standard 2D treatment impedes the flow of electrons from the perovskite to the ETL. Using the quasi-2D treatment this was reduced to 4.9 ns, implying a considerably improved extraction compared with the standard 2D treatment. A similar trend is seen using BTA and PEA (Supplementary Fig. 24). For quantitative values we repeated these observations using power-dependent TA (Supplementary Text 6 and Supplementary Table 8) and space-charge-limited current (SCLC) measurements. From the TA data we found that both 2D and quasi-2D treatments reduced the surface recombination velocity (from $\sim 600\text{ cm s}^{-1}$ to $\sim 300\text{ cm s}^{-1}$). The SCLC measurements show a similar trend (Supplementary Fig. 27) but the overall effect is less obvious as we are examining the entire film and not simply the interfaces.

In PSCs using bulk RDPs, films that contain mixed-dimensional phases have reduced mobility due to charge trapping in the higher n species³. To understand why this is not necessarily the case in 2D/3D heterostructure films, we used TA spectroscopy to measure the charge dynamics. Using a 450 nm pump at a low power ($5\text{ }\mu\text{J cm}^{-2}$) to avoid Auger recombination⁴⁵, we excited the 2D and 3D layers of 2D- and quasi-2D-treated films. Measuring the $n=2$ bleach decay ($\sim 570\text{ nm}$) using monoexponential fits, we calculated the carrier funnelling rates for both treatments; a summary of the results is shown in Supplementary Fig. 28. For a standard 2D-treated film, there are no peaks present for $n > 2$ (Fig. 2a), thus we expect the charges to funnel directly from $n=2$ to the 3D perovskite^{1,46}, for which we observed a 28.6 ps decay time. When we generate a favourable pathway for electrons by adding a layer of PCBM, we observed a faster decay (7.5 ps). Repeating these measurements with a quasi-2D-treated film, we observed a decay without PCBM of 5.8 ps, suggesting that the charges are funnelled to the now present $n > 2$ species^{1,46}. However, adding a layer of PCBM resulted in an even faster decay (1.2 ps), indicating that charge trapping does not play a limiting role in charge extraction.

To gauge the effect of the 2D and quasi-2D treatments in full device stacks, we conducted transient photovoltage (Supplementary Fig. 25) and transient photocurrent measurements (Fig. 5c). Following ref. ⁴⁷, devices were biased with the same white-light intensity to reach near- V_{OC} conditions and were photoexcited with low-power laser pulses to generate small photovoltage perturbations (ΔV , kept to lower than 20 mV). Monoexponential fits were used to estimate the carrier lifetime under V_{OC} and short-circuit current density (J_{SC}) conditions. We observed a slower decay in photovoltage for the quasi-2D-treated films compared with the standard 2D treatment (Supplementary Fig. 25), which is consistent with the TRPL results and indicates a reduction in trap states in the absorber. More importantly, we observed a faster decay in the photocurrent for the quasi-2D-treated films ($\tau_{\text{quasi-2D}} = 0.82\text{ }\mu\text{s}$ compared with $\tau_{2D} = 1.28\text{ }\mu\text{s}$ for 3F-PEA-treated films), which suggests a substantial improvement in carrier extraction⁴⁸. In addition, we performed conductive atomic force microscopy (c-AFM) on these films, revealing increased conductivity in quasi-2D-treated films (Supplementary Figs. 31 and 32).

We fabricated devices with an ITO/NiO_x nanoparticles/perovskite/PCBM/BCP/Ag structure using different surface treatments (BTA, PEA, 2F-PEA, 4F-PEA and 3F-PEA; standard 2D and quasi-2D treatments) for statistical analysis (Supplementary Figs. 33–36). In agreement with our finding that increased $n \geq 3$ RDPs result in more efficient charge extraction, 3F-PEA outperformed the PEA- and BTA-treated devices. Improved performance of the quasi-2D-treated over the standard 2D-treated devices is derived mainly from FF and J_{SC} improvements; a typical set of

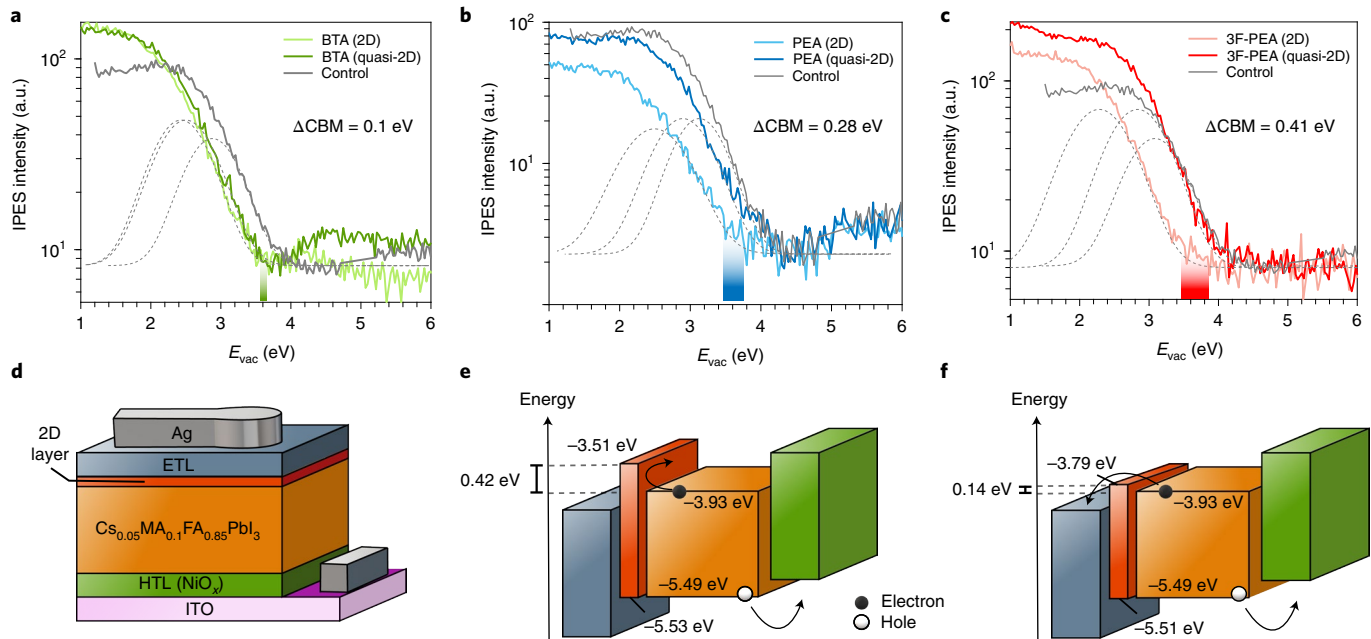


Fig. 4 | Quantifying the conduction band offset of 2D and quasi-2D surface treatments. **a–c**, IPES spectra of BTA- (a), PEA- (b) and 3F-PEA-treated (c) films using 2D and quasi-2D treatments. The dashed lines represent the gaussians used to fit the data. The shaded region represents the change in conduction band edge. IPES measurements were taken using a bandpass filter of 254 nm (4.88 eV) for the control and PEA-treated films and 280 nm (4.42 eV) for BTA- and 3F-PEA-treated films. E_{vac} , vacuum level. **d**, Cross-section of a typical 2D/3D heterostructure in the PIN configuration. **e,f**, The band alignment of the resulting cell using the 2D treatment (e) or the quasi-2D treatment (f). Values in e,f were calculated for a PEA treatment using combined UPS and IPES.

current density–voltage (J – V) curves are shown in Fig. 5d along with their figures of merit. To check the reproducibility, we provide statistics for devices fabricated over a one-year period (September 2020 until September 2021) in Supplementary Figs. 37–39. To confirm that improved passivation alone was not the cause of the increased FF, we simulated the effect of reducing only the surface trap density using the SCAPS-1D simulation tool (Supplementary Fig. 40) and found that a 20 mV difference in V_{OC} would correspond to an increase in FF of approximately 0.5% rather than the 2.2% increase manifested.

A quasi-2D-treated device was certified at the National Renewable Energy Laboratory (NREL). The C₆₀/BCP-based device produced a quasi-steady-state certified PCE for inverted PSCs of 23.91% (with FF = 83.46, $J_{\text{SC}} = 24.90 \text{ mA cm}^{-2}$ and $V_{\text{OC}} = 1.15 \text{ V}$; Supplementary Fig. 43). A voltage loss of 0.38 V is the lowest documented for a NiO_x-based PSC (bandgap from the external quantum efficiency, Supplementary Fig. 42)⁴⁹.

We focused on improving the performance of the NiO_x-HTL inverted PSCs because they have shown high stability at elevated temperatures^{19,49,50}. However, 2D treatments have been shown to be unstable above 50 °C, degrading in a matter of hours⁵¹; thus it was crucial to ascertain whether or not any new 2D treatment could withstand high temperatures. We prepared 2D- and quasi-2D-treated films and heated them at 65 °C for 20 h, periodically measuring their characteristics via TA spectroscopy (Supplementary Fig. 41). We found that the n distribution of both treatments was robust under heating, suggesting that the quasi-2D treatment could be used to produce extremely stable devices.

We evaluated the stability of the devices under accelerated-ageing conditions according to International Summit on Organic Photovoltaic Stability (ISOS) protocols⁵². We tracked the maximum power point (MPP) of two quasi-2D-treated devices under illumination at ~50% relative humidity. An unencapsulated device was monitored at room temperature for 1,000 h (ISOS-L-1I) and an encapsulated device on a temperature-controllable stage was

monitored at 65 °C for 500 h (ISOS-L-3), and the results are shown in Fig. 5e,f, respectively. The unencapsulated room-temperature devices showed no degradation after 1,000 h of MPP tracking (4.9% increase in PCE), whereas the device baked at 65 °C lost around 8% of its maximum PCE after 500 h. On the basis of a linear extrapolation from these data, we estimate the T_{80} lifetime of this device (that is, the time required to drop to 80% of the initial efficiency) to be 1,190 h (Supplementary Fig. 45)^{20,52}. After 500 h the MPP tracking for the heated device was paused but the cell remained under illumination at 65 °C, and after 12 h the MPP tracking was resumed. The PCE of the device recovered to 99% of the initial PCE, which is an encouraging indicator of its real-world long-term stability⁵³. We note that the device structure was not altered for stability testing and the initial efficiency of both devices was >23% (Supplementary Fig. 44). Therefore, we report an ISOS-L-3 accelerated-ageing test that corresponds directly to high-efficiency PSCs (>20% PCE).

Conclusion

We presented a simple technique that alters the QW widths in 2D/3D perovskite heterostructures. This was tailored to improve inverted PSCs, and was accomplished by reducing the confinement within the 2D capping layer to reduce the electron barrier between the 3D and 2D perovskite species. This resulted in highly stable NiO_x-based PSCs with certified efficiency values, and could be useful in other metal halide-based optoelectronics devices in which well-passivated, negative-intrinsic contacts are desirable.

Online content

Any methods, additional references, Nature Research reporting summaries, source data, extended data, supplementary information, acknowledgements, peer review information; details of author contributions and competing interests; and statements of data and code availability are available at <https://doi.org/10.1038/s41566-022-00985-1>.

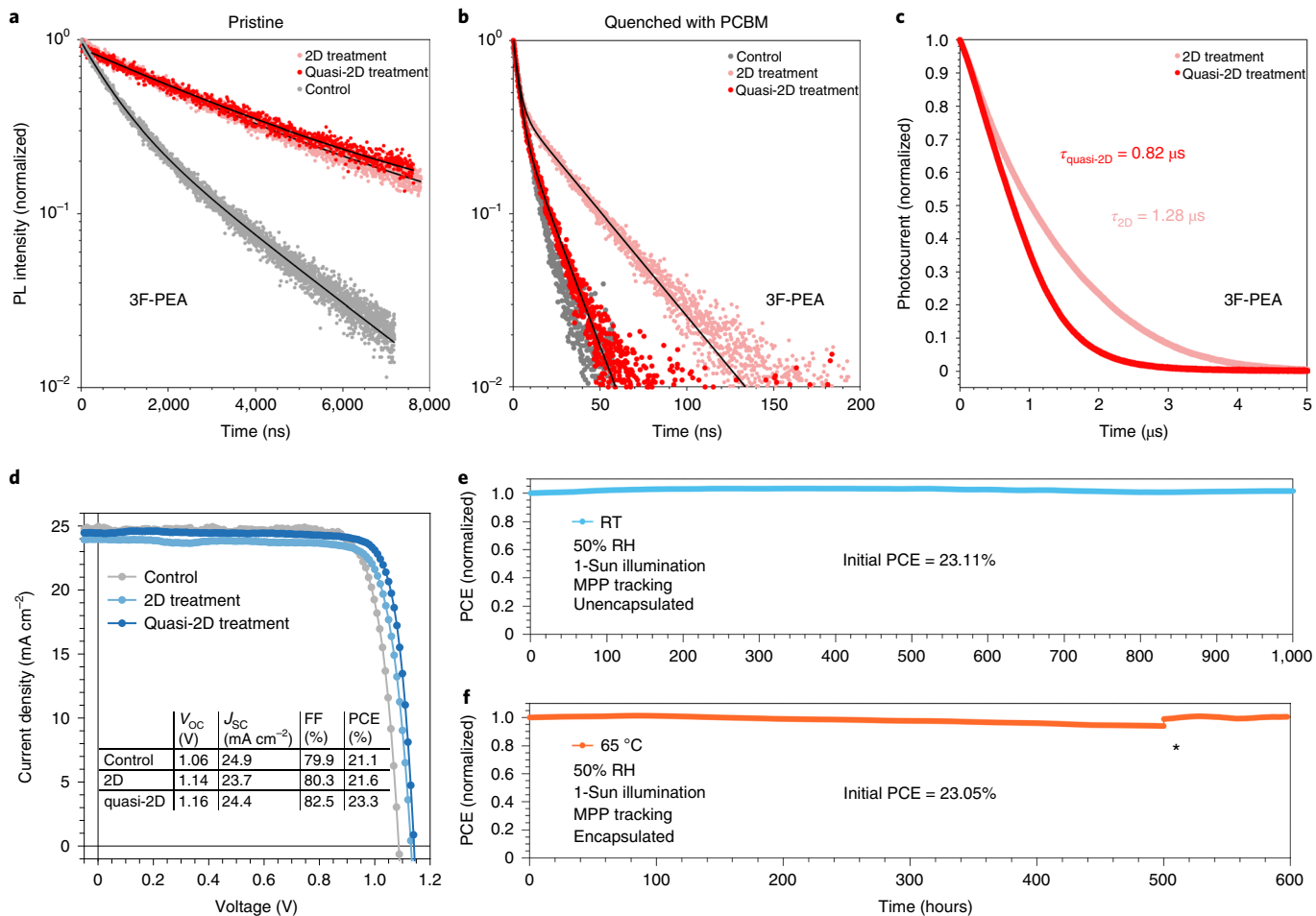


Fig. 5 | Carrier extraction and performance of quasi-2D-treated PSCs. **a**, Transient PL from bare films treated with 3F-PEA. **b**, The same films with PCBM as an electron quencher. **c**, Transient photocurrent measurements for devices using 3F-PEA-treated films. **d**, J - V curves from control, 2D- and quasi-2D-treated devices using 3F-PEA ligands. Statistics for devices using PEA and BTA ligands are also shown in Supplementary Figs. 33–36. **e**, Room-temperature (RT) MPP tracking of an unencapsulated device under 1-Sun illumination and 50% relative humidity (RH). **f**, MPP tracking of an encapsulated device held at 65 °C under 1-Sun illumination and 50% relative humidity (ISOS-L3 conditions). The asterisk indicates the point at which the MPP tracking was paused for 12 h.

Received: 13 July 2021; Accepted: 21 February 2022;
Published online: 7 April 2022

References

- Yuan, M. et al. Perovskite energy funnels for efficient light-emitting diodes. *Nat. Nanotechnol.* **11**, 872–877 (2016).
- Wei, M. et al. Ultrafast narrowband exciton routing within layered perovskite nanoplatelets enables low-loss luminescent solar concentrators. *Nat. Energy* **4**, 197–205 (2019).
- Proppe, A. H. et al. Synthetic control over quantum well width distribution and carrier migration in low-dimensional perovskite photovoltaics. *J. Am. Chem. Soc.* **140**, 2890–2896 (2018).
- Quan, L. N. et al. Ligand-stabilized reduced-dimensionality perovskites. *J. Am. Chem. Soc.* **138**, 2649–2655 (2016).
- Jung, E. H. et al. Efficient, stable and scalable perovskite solar cells using poly(3-hexylthiophene). *Nature* **567**, 511–515 (2019).
- Min, H. et al. Efficient, stable solar cells by using inherent bandgap of α -phase formamidinium lead iodide. *Science* **366**, 749–753 (2019).
- Jeong, M. et al. Stable perovskite solar cells with efficiency exceeding 24.8% and 0.3-V voltage loss. *Science* **369**, 1615–1620 (2020).
- Jiang, Q. et al. Surface passivation of perovskite film for efficient solar cells. *Nat. Photonics* **13**, 460–466 (2019).
- Zhu, H. et al. Tailored amphiphilic molecular mitigators for stable perovskite solar cells with 23.5% efficiency. *Adv. Mater.* **32**, 1907757 (2020).
- Liu, Y. et al. Ultrahydrophobic 3D/2D fluoroarene bilayer-based water-resistant perovskite solar cells with efficiencies exceeding 22%. *Sci. Adv.* **5**, eaaw2543 (2019).
- Kim, G. et al. Impact of strain relaxation on performance of α -formamidinium lead iodide perovskite solar cells. *Science* **370**, 108–112 (2020).
- Jeong, J. et al. Pseudo-halide anion engineering for α -FAPbI₃ perovskite solar cells. *Nature* **592**, 381–385 (2021).
- Teale, S. et al. Dimensional mixing increases the efficiency of 2D/3D perovskite solar cells. *J. Phys. Chem. Lett.* **11**, 5115–5119 (2020).
- Yoo, J. J. et al. An interface stabilized perovskite solar cell with high stabilized efficiency and low voltage loss. *Energy Environ. Sci.* **12**, 2192–2199 (2019).
- Hu, Y. et al. Hybrid perovskite/perovskite heterojunction solar cells. *ACS Nano* **10**, 5999–6007 (2016).
- Proppe, A. H. et al. Multication perovskite 2D/3D interfaces form via progressive dimensional reduction. *Nat. Commun.* **12**, 3472 (2021).
- Jang, Y. W. et al. Intact 2D/3D halide junction perovskite solar cells via solid-phase in-plane growth. *Nat. Energy* **6**, 63–71 (2021).
- Zhang, T. et al. Stable and efficient 3D-2D perovskite-perovskite planar heterojunction solar cell without organic hole transport layer. *Joule* **2**, 2706–2721 (2018).
- Bai, S. et al. Planar perovskite solar cells with long-term stability using ionic liquid additives. *Nature* **571**, 245–250 (2019).
- Lin, Y. H. et al. A piperidinium salt stabilizes efficient metal-halide perovskite solar cells. *Science* **369**, 96–102 (2020).
- Zheng, X. et al. Managing grains and interfaces via ligand anchoring enables 22.3%-efficiency inverted perovskite solar cells. *Nat. Energy* **5**, 131–140 (2020).
- Chen, S., Xiao, X., Gu, H. & Huang, J. Iodine reduction for reproducible and high-performance perovskite solar cells and modules. *Sci. Adv.* **7**, eabe8130 (2021).

23. Chen, C. et al. Arylammonium-assisted reduction of the open-circuit voltage deficit in wide-bandgap perovskite solar cells: the role of suppressed ion migration. *ACS Energy Lett.* **5**, 2560–2568 (2020).
24. Bai, Y. et al. Dimensional engineering of a graded 3D–2D halide perovskite interface enables ultrahigh V_{oc} enhanced stability in the p-i-n photovoltaics. *Adv. Energy Mater.* **7**, 1701038 (2017).
25. Park, S. M., Abtahi, A., Boehm, A. M. & Graham, K. R. Surface ligands for methylammonium lead iodide films: surface coverage, energetics, and photovoltaic performance. *ACS Energy Lett.* **5**, 799–806 (2020).
26. La-Placa, M. G. et al. Vacuum-deposited 2D/3D perovskite heterojunctions. *ACS Energy Lett.* **4**, 2893–2901 (2019).
27. Zhao, T., Chueh, C.-C., Chen, Q., Rajagopal, A. & Jen, A. K.-Y. Defect passivation of organic–inorganic hybrid perovskites by diammonium iodide toward high-performance photovoltaic devices. *ACS Energy Lett.* **1**, 757–763 (2016).
28. Proppe, A. H. et al. Photochemically cross-linked quantum well ligands for 2D/3D perovskite photovoltaics with improved photovoltage and stability. *J. Am. Chem. Soc.* **141**, 14180–14189 (2019).
29. Mahmud, M. A. et al. Double-sided surface passivation of 3D perovskite film for high-efficiency mixed-dimensional perovskite solar cells. *Adv. Funct. Mater.* **30**, 1907962 (2020).
30. Burgelman, M., Nollet, P. & Degrave, S. Modelling polycrystalline semiconductor solar cells. *Thin Solid Films* **361–362**, 527–532 (2000).
31. Zhou, L. et al. Highly efficient and stable planar perovskite solar cells with modulated diffusion passivation toward high power conversion efficiency and ultrahigh fill factor. *Sol. RRL* **3**, 1900293 (2019).
32. Cao, D. H., Stoumpos, C. C., Farha, O. K., Hupp, J. T. & Kanatzidis, M. G. 2D homologous perovskites as light-absorbing materials for solar cell applications. *J. Am. Chem. Soc.* **137**, 7843–7850 (2015).
33. Ma, J. & Wang, L. W. Nanoscale charge localization induced by random orientations of organic molecules in hybrid perovskite $\text{CH}_3\text{NH}_3\text{PbI}_3$. *Nano Lett.* **15**, 248–253 (2015).
34. Quintero-Bermudez, R. et al. Compositional and orientational control in metal halide perovskites of reduced dimensionality. *Nat. Mater.* **17**, 900–907 (2018).
35. Hu, J. et al. Synthetic control over orientational degeneracy of spacer cations enhances solar cell efficiency in two-dimensional perovskites. *Nat. Commun.* **10**, 1276 (2019).
36. Niu, T. et al. Interfacial engineering at the 2D/3D heterojunction for high-performance perovskite solar cells. *Nano Lett.* **19**, 7181–7190 (2019).
37. Gharibzadeh, S. et al. Record open-circuit voltage wide-bandgap perovskite solar cells utilizing 2D/3D perovskite heterostructure. *Adv. Energy Mater.* **9**, 1803699 (2019).
38. Briggs, D. & Seah, M. P. (eds) *Practical Surface Analysis. Auger and X-ray Photoelectron Spectroscopy* 2nd edn, Vol. 1 (Wiley, 1990).
39. Boehm, A. M., Liu, T., Park, S. M., Abtahi, A. & Graham, K. R. Influence of surface ligands on energetics at $\text{FASnI}_3/\text{C}_{60}$ interfaces and their impact on photovoltaic performance. *ACS Appl. Mater. Interfaces* **12**, 5209–5218 (2020).
40. Yoshida, H. Near-ultraviolet inverse photoemission spectroscopy using ultra-low energy electrons. *Chem. Phys. Lett.* **539–540**, 180–185 (2012).
41. Boehm, A. M., Wieser, J., Butrouna, K. & Graham, K. R. A new photon source for ultraviolet photoelectron spectroscopy of organic and other damage-prone materials. *Org. Electron.* **41**, 9–16 (2017).
42. Endres, J. et al. Valence and conduction band densities of states of metal halide perovskites: a combined experimental–theoretical study. *J. Phys. Chem. Lett.* **7**, 2722–2729 (2016).
43. She, X. J. et al. A solvent-based surface cleaning and passivation technique for suppressing ionic defects in high-mobility perovskite field-effect transistors. *Nat. Electron.* **3**, 694–703 (2020).
44. Kirchartz, T., Márquez, J. A., Stolterfoht, M. & Unold, T. Photoluminescence-based characterization of halide perovskites for photovoltaics. *Adv. Energy Mater.* **10**, 1904134 (2020).
45. Zhou, M., Sarmiento, J. S., Fei, C. & Wang, H. Charge transfer and diffusion at the perovskite/PCBM interface probed by transient absorption and reflection. *J. Phys. Chem. C* **123**, 22095–22103 (2019).
46. Proppe, A. H. et al. Spectrally resolved ultrafast exciton transfer in mixed perovskite quantum wells. *J. Phys. Chem. Lett.* **10**, 419–426 (2019).
47. Shao, Y., Yuan, Y. & Huang, J. Correlation of energy disorder and open-circuit voltage in hybrid perovskite solar cells. *Nat. Energy* **1**, 15001 (2016).
48. Chen, W. et al. Efficient and stable large-area perovskite solar cells with inorganic charge extraction layers. *Science* **350**, 944–948 (2015).
49. Ma, F. et al. Nickel oxide for inverted structure perovskite solar cells. *J. Energy Chem.* **52**, 393–411 (2020).
50. Boyd, C. C. et al. Overcoming redox reactions at perovskite–nickel oxide interfaces to boost voltages in perovskite solar cells. *Joule* **4**, 1759–1775 (2020).
51. Sutanto, A. A. et al. Dynamical evolution of the 2D/3D interface: a hidden driver behind perovskite solar cell instability. *J. Mater. Chem. A* **8**, 2343–2348 (2020).
52. Khenkin, M. V. et al. Consensus statement for stability assessment and reporting for perovskite photovoltaics based on ISOS procedures. *Nat. Energy* **5**, 35–49 (2020).
53. Lu, H. et al. Vapor-assisted deposition of highly efficient, stable black-phase FAPbI_3 perovskite solar cells. *Science* **370**, eabb8985 (2020).

Publisher's note Springer Nature remains neutral with regard to jurisdictional claims in published maps and institutional affiliations.

© The Author(s), under exclusive licence to Springer Nature Limited 2022

Methods

Materials. All the materials were used as received without purification. Commercial indium tin oxide (ITO) substrates (20Ω per square) with dimensions of 25×25 mm were purchased from TFD. PbI_2 and bathocuproine (BCP) were purchased from TCI. Caesium iodide (CsI) (99.999%) and fullerene (C_{60}) (99.5%) were purchased from Sigma-Aldrich. PEAI, FAI (formamidinium iodide) and MAI were purchased from GreatCell Solar. 2F-PEAI (2-fluoro-phenethylammonium iodide), 3F-PEAI, 4F-PEAI (4-fluoro-phenethylammonium iodide) and 1-naphthylmethylammonium iodide were purchased from Xi'an Polymer Light Technology. PCBM was purchased from Nano-C. All the solvents used in the process were anhydrous and purchased from Sigma-Aldrich.

Nickel oxide nanoparticle synthesis. The NiO_x nanoparticles were prepared via the hydrolysis of nickel nitrate following previous work^{4,5}. Briefly, $\text{Ni}(\text{NO}_3)_2 \cdot 6\text{H}_2\text{O}$ (20 mmol) was dissolved in deionized water (20 ml) to obtain a dark-green solution. Then, NaOH aqueous solution (4 ml, 10 mol l⁻¹) was slowly added to the dark-green solution with stirring. After being stirred for 20 min, the colloidal precipitate was washed thoroughly using deionized water three times and dried at 80°C for 6 h. The obtained green powder was then calcined at 270°C for 2 h to obtain a black powder. The NiO_x nanoparticle ink was prepared by dispersing the obtained NiO_x nanoparticles in a mixed solution of deionized water and IPA (3:1, v/v) for a concentration of 10 mg ml⁻¹.

Solar cell fabrication. ITO glass was cleaned through sequential washing with detergent, deionized water, acetone and IPA. Before use, the ITO was cleaned with ultraviolet ozone for 20 min.

For the inverted solar cells, the substrate was spin-coated with a thin layer of NiO_x nanoparticle film using the NiO_x nanoparticle ink at 2,000 r.p.m. for 30 s. The perovskite absorber layers were deposited inside a nitrogen-filled glovebox with a controlled water and oxygen level of less than 1 ppm. The temperature inside was monitored to be $25\text{--}30^\circ\text{C}$. The precursors for the $\text{Cs}_{0.05}\text{FA}_{0.85}\text{MA}_{0.1}\text{PbI}_3$ perovskites were prepared by dissolving the PbI_2 , MAI, CsI and FAI in a mixed solvent (4:1 in volume) of DMF and dimethyl sulfoxide (DMSO), respectively. This was done by adding the powders to a vial (20 ml size) and then adding the mixed solvent (1 ml) before leaving the vial on a stirring hotplate set to 60°C for 30 min; all steps were undertaken in a glovebox. For fabrication of the perovskite film, the substrate was spun at 2,000 r.p.m. for 30 s with an initial acceleration of 1,000 r.p.m., and then at 6,000 r.p.m. for 10 s with an acceleration of 6,000 r.p.m. per second. In the second step, anisole (150 μl) was added dropwise onto the substrate during the last 5 s of spinning. The substrate was immediately placed on a hotplate and annealed at 100°C for 10 min. For the surface treatment, the 2D solutions were prepared by dissolving the 2D ligand salts (that is, PEAI, BTAI, 3F-PEAI, HAI and OTAI) with or without MAI and DMF in IPA. The ligand salt (1 mg ml⁻¹), MAI (0.5 mg ml⁻¹) and an IPA:DMF v/v ratio of 1:200 was used, unless stated otherwise. The 2D layer was fabricated by depositing the 2D ligand solution (150 μl) onto the perovskite film surface, and immediately after deposition the film was spun at a rate of 4,000 r.p.m. for 30 s with a 4,000 r.p.m. per second acceleration. The film was then annealed at 100°C for 5 min.

For the ETL, either C_{60} /ALD-SnO₂ or PCBM/BCP were used. C_{60} was formed via evaporation, and deposition of the ALD-SnO₂ (atomic-layer-deposited tin(IV) oxide) was carried out using a PICOSUN R-200 Advanced ALD system. Water and tetrakis(dimethylamino)tin(IV) (TDMASn) were used as the oxygen and tin precursors, respectively. The precursor and substrate temperature was set to 75°C and 85°C , respectively. Nitrogen gas (90 sccm) was used as carrier gas. Pulse and purge times for water were 1 s and 5 s, respectively, and 1.6 s and 5 s, respectively, for TDMASn. The total deposition cycle is 134 s, corresponding to 20 nm of SnO₂.

PCBM was formed by spin coating the PCBM solution (20 mg ml⁻¹ in chlorobenzene) at 1,000 r.p.m. for 30 s and then annealing at 100°C for 5 min. Then a thin and uniform BCP layer was deposited via drop-casting 2–3 drops of BCP dissolved in IPA while spinning the substrate at 5,000 r.p.m. Finally, a 120-nm-thick silver contact was deposited on top of the BCP using thermal evaporation under high vacuum ($<5 \times 10^{-7}$ torr) using an Angstrom Engineering deposition system to produce a cell with an active area of 0.053 cm².

For non-inverted solar cells, the substrate was spin-coated with a thin layer of SnO₂ nanoparticle solution (1:3:3, SnO₂ (15% in water):IPA:water) at 3,000 r.p.m. for 20 s and annealed in ambient air at 150°C for 1 h. The perovskite solution was prepared by dissolving FAPbI₃ (889 mg ml⁻¹), MAPbBr₃ (33 mg ml⁻¹) and MAI (33 mg ml⁻¹) in DMF/DMSO (8:1 v/v) mixed solvent. Then, the solution was coated onto the ITO/SnO₂ substrate through two consecutive spin-coating steps, at 1,000 r.p.m. for 5 s and 2,500 r.p.m. for 20 s. During the second spin-coating (2,500 r.p.m.) step, diethyl ether (1 ml) was poured onto the substrate after 15 s. The intermediate phase substrate was then put on a hotplate at 150°C for 10 min. After the fabrication of the 3D perovskite film, the 2D layer was fabricated by depositing a solution (5 mg ml⁻¹) of PEAI in IPA onto the perovskite film and then spinning the substrate at 4,000 r.p.m. for 30 s. Then, the substrate was heat-treated at 100°C for 5 min. For deposition of the hole transport material, a spiro-OMeTAD solution in chlorobenzene (90.9 mg mL⁻¹) was prepared, and lithium-bis(trifluoromethanesulfonyl) imide solution in acetonitrile (23 μl , 540 mg mL⁻¹) and pure 4-*tert*-butylpyridine (39 μl) were added to an aliquot of the solution (1.1 ml). The

spiro-OMeTAD solution including additives was spin-coated onto the perovskite surface at 1,750 r.p.m. for 30 s. Finally, a gold electrode was deposited via thermal evaporation to produce a cell with an active area of 0.053 cm².

Reduced-dimensional film fabrication. Reduced-dimensional (PEA)₂(MA/FA/Cs)_{n-1}Pb_nI_{3n+1} perovskite solutions were prepared by dissolving the appropriate stoichiometric quantities of PbI_2 , MAI (or FAI or CsI) with PEAI in DMF/DMSO (4:1 v/v). The resulting solution was filtered using a polytetrafluoroethylene syringe filter (0.2 μm) before deposition. Then, the solution was coated onto the glass substrate through two consecutive spin-coating steps, at 1,000 r.p.m. for 5 s and 2,500 r.p.m. for 20 s. During the second spin-coating (2,500 r.p.m.) step, diethyl ether (1 ml) was poured onto the substrate after 15 s. The intermediate phase substrate was then put on a hotplate at 150°C for 10 min.

Device testing. The current density–voltage (*J*–*V*) characteristics were measured using a Keithley 2400 source meter under illumination from a solar simulator (Class A, Newport) with a light intensity of 100 mW cm^{-2} (checked using a calibrated reference solar cell from Newport). The *J*–*V* curves were measured in a nitrogen atmosphere with a scanning rate of 100 mV s^{-1} (a voltage step of 10 mV and a delay time of 200 ms). The active area was determined by the aperture shade mask (0.049 cm² for small-area devices) placed in front of the solar cell. A spectral mismatch factor of unity was used for all *J*–*V* measurements. For stabilized output measurements at the MPP, the device testing chamber was left under ambient conditions. Solar cells were fixed at the MPP voltage, (determined from *J*–*V* sweeps in both scanning directions) and the current output was tracked over time.

Stability testing. Devices were placed in a homemade stability-tracking station. The illumination source is a white-light LED with its intensity calibrated to match 1-Sun conditions. For room-temperature tests (ISOS-L-II), the device chamber was sealed and supplied with continuous nitrogen purging. For the ISOS-L-3 ageing test, the device chamber was left open in a room with $50 \pm 10\%$ relative humidity, and the solar cell was mounted on a metal plate kept at 65°C using a heating element. A thermal couple attached to the metal plate was used to monitor and provide feedback control to the heating element to ensure temperature consistency. The MPP was tracked using a perturb-and-observe algorithm that updates the MPP value every 10 s. Encapsulation was done by capping the device with a glass slide, using UV-adhesive (LT-U001, Lumtec) as the sealant.

X-ray diffraction. X-ray diffraction patterns were collected using a Rigaku D/Max-2500 diffractometer equipped with Cu K α 1 radiation ($\lambda = 1.54056\text{ \AA}$).

Grazing incidence wide-angle X-ray scattering. GIWAXS measurements were conducted at the BL14B1 beamline of the Shanghai Synchrotron Radiation Facility using X-rays with a wavelength of $\lambda = 1.24\text{ \AA}$ at a grazing incidence angle of 0.3° and an exposure time of 80 s. The GIXRD patterns were collected using a MarCCD 225 detector with a sample–detector distance of 280 mm and were presented in *q* coordinates using the equation $q = 4\pi \sin \theta / \lambda$, where θ is half of the diffraction angle. In the present GIXRD data, *q* has been calibrated by measuring the X-ray diffraction from a lanthanum hexaboride reference sample. Images were calibrated using lanthanum hexaboride and processed using the *Nika* software package⁵⁶ and the GIXSGUI MATLAB plug-in⁵⁷.

Simulations. Simulations of PSCs were conducted using the heterojunction solar cell simulator SCAPS-1D, version 3.3.07³⁰. Full simulation details can be found in Supplementary Text 2.

Conductive atomic force microscopy. Scanning probe microscopy experiments were carried out under ambient conditions using an Asylum Research Cypher S AFM instrument with low-force-constant ($k = 2.8\text{ N m}^{-1}$), Ti/Ir-coated, silicon cantilevers (ASYELEC.01-R2). Contact-mode AFM was used to simultaneously produce surface and current maps applying a fixed bias voltage of -0.6 V . Measurements were obtained under top illumination from a 3 W white LED.

Transient absorption spectroscopy. Femtosecond laser pulses of 1,030 nm generated using a Yb:KGW laser at a 5 kHz repetition rate (Pharos, Light Conversion) were passed through an optical parametric amplifier (Orpheus, Light Conversion) to select 450 nm light. This served as the pump pulse, whereas the probe pulse was generated by focusing the initial 1,030 nm pulse into a sapphire crystal, which resulted in a white-light continuum (Helios, Ultrafast). With a temporal resolution of the system of ~ 350 fs, each time step meant delaying the probe pulse with respect to the pump, with time steps that increased exponentially. Every other pump pulse was blocked using a chopper to determine the change in optical density. After going through a grating spectrograph, the pulses were measured using a charge-coupled device (CCD) (Helios, Ultrafast).

Spinning *in situ* TA spectroscopy was performed using a purpose-built spinner, designed such that the incident probe light could pass through the spinning substrate and be directed into the CCD. The pump–probe delay was set to 1 ps. The time resolution of the system was 0.3 s. The measurements were taken in an ambient atmosphere with 35% relative humidity.

Photoluminescence quantum yield measurements. The excitation source was an unfocused beam from a 442 nm continuous-wave diode laser. Photoluminescence was collected using an integrating sphere with a pre-calibrated fibre coupled to a spectrometer (QE Pro, Ocean Optics) with an intensity of $\sim 100 \text{ mW cm}^{-2}$. PLQY values were calculated using $\text{PLQY} = \frac{P_s}{P_{\text{ex}} \times A}$, where $A = 1 - P_l/P_{\text{Ex}}$, P_s is the integrated photon count of the sample emission on laser excitation, P_{ex} is the integrated photon count of the excitation laser when the sample is removed from the integrating sphere and P_l is the integrated photon count of excitation laser when sample is mounted in the integrating sphere and hit by the beam.

Space-charge-limited current measurements. SCLC measurements were obtained using electron-only (ITO/SnO_x/perovskite/PCBM/Ag) devices and hole-only (ITO/NiO_x/perovskite/poly(triaryl amine)/Au) devices separately. A Keithley 2400 source meter was used to measure the relevant $J-V$ curves. We calculated the trap density (n_t) by SCLC measurement in the hole-only and electron-only devices. The trap-state density n_t can be calculated using the following relation:

$$n_t = \frac{V_{\text{TFI}} \epsilon \epsilon_0}{eL^2}$$

where e is the elementary charge, L is the perovskite film thickness ($\sim 650 \text{ nm}$), ϵ_0 is the vacuum permittivity, ϵ is the relative dielectric constant and V_{TFI} is the onset voltage of trap-filled limit region.

Transient photoluminescence spectroscopy. TRPL measurements were carried out using a Horiba Fluorolog time-correlated single photon counting system with photomultiplier tube detectors. A pulsed laser diode (634 nm, 110–140 ps pulse width) was used as the excitation source for steady-state and transient measurements. For transient measurements, a 7,200 ns period for unquenched films and an 800 ns period for quenched films (0.28 nJ per pulse) was used to capture accurate carrier lifetimes.

Inverse photoelectron spectroscopy and ultraviolet photoelectron spectroscopy. For combined UPS and IPES measurements, an Excitech H Lyman- α photon source (10.2 eV) with an oxygen-filled beam path was used for excitation, coupled with a PHI 5600 ultrahigh vacuum system with a hemispherical electron energy analyser. A sample bias of -5 V and a pass energy of 5.85 eV were used for UPS acquisition. IPES measurements were performed in the Bremsstrahlung isochromat mode with electron kinetic energies below 5 eV and an emission current of $2 \mu\text{A}$ to minimize sample damage. A Kimball Physics ELG-2 electron gun with a barium oxide cathode was used to generate the electron beam; the emitted photons were collected using a bandpass photon detector that included an optical bandpass filter (280 nm for 3F-PEA- and BTA-treated films, and 254 nm for the control and PEA-treated films) and a photomultiplier tube (R585, Hamamatsu Photonics). Samples were held at a -20 V bias during all IPES measurements and the ultrahigh vacuum chamber was blacked-out to exclude external light.

Perovskite films sent for combined UPS/IPES were fabricated on ITO/NiO_x substrates.

UPS measurements of quasi-2D perovskite films were carried out using a Thermo Fisher ESCALAB 250XL instrument; a -10 V bias was applied for UPS measurements.

Transient photovoltage/photocurrent measurements. These measurements were carried out according to ref. ⁴⁷.

Kelvin probe force microscopy. KPFM was conducted using an MFP-3D AFM (Asylum Research, Oxford Instruments) with conductive Ti/Ir-coated tips (ASYELEC.01-R2 probe, $f = 71.72 \text{ kHz}$, $k = 2.8 \text{ N m}^{-1}$). The tips were calibrated using Sader's method^{58,59}. The KPFM measurement was implemented using a two-path method at a scan rate of 0.5 Hz, where the first pass in every scan line was used to determine the topography and the following second pass was used to measure the contact potential difference between the tip and the sample. The second pass was scanned by raising the tip at a fixed 20 nm height above the sample following the topography. Each set of samples was arranged in proximity on a common substrate and were measured using the same tip and scanning parameters. We also adopted different scanning sequences of the samples in each set to ensure that the obtained potential trend is reliable and the global drift (if any) is not dominating. The two sets of samples (PEA- and 3F-PEA-treated) were measured using different probes, thus a shift in the overall potential is observed.

Reporting Summary. Further information on research design is available in the Nature Research Reporting Summary linked to this article.

Data availability

Source data are provided with this paper. All the data supporting the findings of this study are available within this article and its Supplementary Information. Any additional information can be obtained from corresponding authors upon request.

References

54. Chen, H. et al. Efficient and stable inverted perovskite solar cells incorporating secondary amines. *Adv. Mater.* **31**, 1903559 (2019).
55. Chen, H. et al. Band alignment towards high-efficiency NiO_x-based Sn-Pb mixed perovskite solar cells. *Sci. China Mater.* **64**, 537–546 (2021).
56. Ilavsky, J. *Nika*: software for two-dimensional data reduction. *J. Appl. Crystallogr.* **45**, 324–328 (2012).
57. Jiang, Z. *GIXSGUI*: a MATLAB toolbox for grazing-incidence X-ray scattering data visualization and reduction, and indexing of buried three-dimensional periodic nanostructured films. *J. Appl. Crystallogr.* **48**, 917–926 (2015).
58. Sader, J. E. et al. Spring constant calibration of atomic force microscope cantilevers of arbitrary shape. *Rev. Sci. Instrum.* **83**, 103705 (2012).
59. Sader, J. E., Lu, J. & Mulvaney, P. Effect of cantilever geometry on the optical lever sensitivities and thermal noise method of the atomic force microscope. *Rev. Sci. Instrum.* **85**, 113702 (2014).

Acknowledgements

This research was made possible by the US Department of the Navy, Office of Naval Research Grant (N00014-20-1-2572). This work was supported in part by the Ontario Research Fund-Research Excellence program (ORF7-Ministry of Research and Innovation, Ontario Research Fund-Research Excellence Round 7). We appreciate the Shanghai Synchrotron Radiation Facility (beamline 14B and 16B) and X. Gao and Z. Su for their help with GIWAXS characterization. Z.N. is grateful for support by the National Key Research Program (2021YFA0715502, 2016YFA0204000) and the National Science Fund of China (61935016). S.M.P., H.R.A. and K.R.G. acknowledge the US Department of Energy under Grant DE-SC0018208 for supporting the UPS and IPES measurements. T.F. and T.C. acknowledge the Canadian Foundation for Innovation and the Natural Science and Engineering Council of Canada (NSERC) for KPFM measurements. F.L and Y.G. were funded by the King Abdullah University of Science and Technology (KAUST) Office of Sponsored Research (OSR) under Award No: OSR-CARF/CCF-3079 and OSR-2018-CRG7-3737.

Author contributions

H.C., S.T., B.C. and Y.H. conceived the idea. H.C., K.B., L.G. and S.T. prepared samples for characterization. S.M.P. and H.R.A. performed UPS and IPES measurements, and S.M.P., H.R.A., S.T. and K.R.G. analysed the data. S.T. performed the TA experiments and analysed the data with Y.G. and F.L. The *in situ* TA system for use in this paper was developed by S.T., A.K.J. and A.H.P. The *in situ* measurements were performed by S.T. who also analysed the data. T.Z. performed the DFT calculations and analysed the data. B.C. performed PLQY measurements and H.C. measured the PL lifetimes. M.W. carried out the transient photocurrent and photovoltage measurements and S.T. analysed the data. S.T. performed SCAPS simulations. S.T. collected the thin-film X-ray diffraction patterns. C.H. and D.Y. performed the GIWAXS experiments and obtained the SEM images. S.T. and B.C. analysed the data. The KPFM measurements were performed by T.C., and T.F. analysed the data. H.C. and W.Z. carried out the SCLC measurements and S.T. analysed the data. S.T. conducted the c-AFM measurements. H.C. fabricated all the devices for performance and certification. B.C. and S.H. helped with device certification. B.C. built the heated MPP-tracking station. Q.Z., K.X. and C.Z. carried out the UPS on bulk 2D films. Z.N. and E.H.S. supervised and funded the work. S.T. wrote the draft manuscript with input from B.C. and E.H.S. All authors contributed to the revision of the final paper.

Competing interests

The authors declare no competing interests.

Additional information

Supplementary information The online version contains supplementary material available at <https://doi.org/10.1038/s41566-022-00985-1>.

Correspondence and requests for materials should be addressed to Zhijun Ning or Edward H. Sargent.

Peer review information *Nature Photonics* thanks Mohammad Khaja Nazeeruddin, Ling Xu the other, anonymous, reviewer(s) for their contribution to the peer review of this work.

Reprints and permissions information is available at www.nature.com/reprints.

Solar Cells Reporting Summary

Nature Research wishes to improve the reproducibility of the work that we publish. This form is intended for publication with all accepted papers reporting the characterization of photovoltaic devices and provides structure for consistency and transparency in reporting. Some list items might not apply to an individual manuscript, but all fields must be completed for clarity.

For further information on Nature Research policies, including our [data availability policy](#), see [Authors & Referees](#).

► Experimental design

Please check: are the following details reported in the manuscript?

1. Dimensions

Area of the tested solar cells

Yes
 No

The small area of solar cells is 0.053 cm² (Methods - Solar Cell fabrication)

Method used to determine the device area

Yes
 No

The active area is 0.049 cm² (Methods - Device testing)

2. Current-voltage characterization

Current density-voltage (J-V) plots in both forward and backward direction

Yes
 No

Figure S46

Voltage scan conditions

For instance: scan direction, speed, dwell times

Yes
 No

JV curves were measured with a scanning rate of 100 mV/s (voltage step of 10mV and delay time of 200ms) (Methods - Device testing)

Test environment

For instance: characterization temperature, in air or in glove box

Yes
 No

Unencapsulated devices were tested in a nitrogen environment. Encapsulated devices were tested at 65 degrees Celsius in 50% relative humidity. (Figure 5e,f, Methods - Stability testing)

Protocol for preconditioning of the device before its characterization

Yes
 No

No preconditioning was used

Stability of the J-V characteristic

Verified with time evolution of the maximum power point or with the photocurrent at maximum power point; see ref. 7 for details.

Yes
 No

Maximum power point tracking (Figure 5 e,f)

3. Hysteresis or any other unusual behaviour

Description of the unusual behaviour observed during the characterization

Yes
 No

Cells saw negligible hysteresis (~ 1%) (Fig. S46)

Related experimental data

Yes
 No

Fig. S46

4. Efficiency

External quantum efficiency (EQE) or incident photons to current efficiency (IPCE)

Yes
 No

Figure S42

A comparison between the integrated response under the standard reference spectrum and the response measure under the simulator

Yes
 No

Figure S42

For tandem solar cells, the bias illumination and bias voltage used for each subcell

Yes
 No

This report does not include tandem solar cells

5. Calibration

Light source and reference cell or sensor used for the characterization

Yes
 No

Newport, Class A simulator is used for the measurements (Methods, Device testing)

Confirmation that the reference cell was calibrated and certified

Yes
 No

The light intensity was calibrated by reference solar cell by Newport (Methods - Device testing)

<p>Calculation of spectral mismatch between the reference cell and the devices under test</p> <p>6. Mask/aperture</p> <p>Size of the mask/aperture used during testing</p> <p>Variation of the measured short-circuit current density with the mask/aperture area</p> <p>7. Performance certification</p> <p>Identity of the independent certification laboratory that confirmed the photovoltaic performance</p> <p>A copy of any certificate(s) <i>Provide in Supplementary Information</i></p> <p>8. Statistics</p> <p>Number of solar cells tested</p> <p>Statistical analysis of the device performance</p> <p>9. Long-term stability analysis</p> <p>Type of analysis, bias conditions and environmental conditions <i>For instance: illumination type, temperature, atmosphere humidity, encapsulation method, preconditioning temperature</i></p>	<input type="checkbox"/> Yes We rely on certified efficiency results. <input checked="" type="checkbox"/> No
	<input checked="" type="checkbox"/> Yes 0.049 cm ² (Methods - Device testing) <input type="checkbox"/> No
	<input type="checkbox"/> Yes We did not evaluate multiple testing apertures <input checked="" type="checkbox"/> No
	<input checked="" type="checkbox"/> Yes NREL (Figure S43) <input type="checkbox"/> No
	<input checked="" type="checkbox"/> Yes Figure S43 <input type="checkbox"/> No
	<input checked="" type="checkbox"/> Yes Statistical analysis was performed on 10-20 devices of each architecture (Figure S33 - S39) <input type="checkbox"/> No
	<input checked="" type="checkbox"/> Yes Figure S33 - S39 <input type="checkbox"/> No
	<input checked="" type="checkbox"/> Yes Stability tests were performed under 1-sun illumination from a white LED and MPP-tracked conditions. Unencapsulated devices were tested in a nitrogen environment. Encapsulated devices were tested at 65 degrees Celsius in 50% relative humidity. (Figure 5 e,f, Methods - Stability testing) <input type="checkbox"/> No

Solar Cells Reporting Summary

Nature Research wishes to improve the reproducibility of the work that we publish. This form is intended for publication with all accepted papers reporting the characterization of photovoltaic devices and provides structure for consistency and transparency in reporting. Some list items might not apply to an individual manuscript, but all fields must be completed for clarity.

For further information on Nature Research policies, including our [data availability policy](#), see [Authors & Referees](#).

► Experimental design

Please check: are the following details reported in the manuscript?

1. Dimensions

Area of the tested solar cells

Yes
 No

The small area of solar cells is 0.053 cm² (Methods - Solar Cell fabrication)

Method used to determine the device area

Yes
 No

The active area is 0.049 cm² (Methods - Device testing)

2. Current-voltage characterization

Current density-voltage (J-V) plots in both forward and backward direction

Yes
 No

Figure S46

Voltage scan conditions

For instance: scan direction, speed, dwell times

Yes
 No

JV curves were measured with a scanning rate of 100 mV/s (voltage step of 10mV and delay time of 200ms) (Methods - Device testing)

Test environment

For instance: characterization temperature, in air or in glove box

Yes
 No

Unencapsulated devices were tested in a nitrogen environment. Encapsulated devices were tested at 65 degrees Celsius in 50% relative humidity. (Figure 5e,f, Methods - Stability testing)

Protocol for preconditioning of the device before its characterization

Yes
 No

No preconditioning was used

Stability of the J-V characteristic

Verified with time evolution of the maximum power point or with the photocurrent at maximum power point; see ref. 7 for details.

Yes
 No

Maximum power point tracking (Figure 5 e,f)

3. Hysteresis or any other unusual behaviour

Description of the unusual behaviour observed during the characterization

Yes
 No

Cells saw negligible hysteresis (~ 1%) (Fig. S46)

Related experimental data

Yes
 No

Fig. S46

4. Efficiency

External quantum efficiency (EQE) or incident photons to current efficiency (IPCE)

Yes
 No

Figure S42

A comparison between the integrated response under the standard reference spectrum and the response measure under the simulator

Yes
 No

Figure S42

For tandem solar cells, the bias illumination and bias voltage used for each subcell

Yes
 No

This report does not include tandem solar cells

5. Calibration

Light source and reference cell or sensor used for the characterization

Yes
 No

Newport, Class A simulator is used for the measurements (Methods, Device testing)

Confirmation that the reference cell was calibrated and certified

Yes
 No

The light intensity was calibrated by reference solar cell by Newport (Methods - Device testing)

Calculation of spectral mismatch between the reference cell and the devices under test

Yes
 No

We rely on certified efficiency results.

6. Mask/aperture

Size of the mask/aperture used during testing

Yes
 No

0.049 cm² (Methods - Device testing)

Variation of the measured short-circuit current density with the mask/aperture area

Yes
 No

We did not evaluate multiple testing apertures

7. Performance certification

Identity of the independent certification laboratory that confirmed the photovoltaic performance

Yes
 No

NREL (Figure S43)

A copy of any certificate(s)
Provide in Supplementary Information

Yes
 No

Figure S43

8. Statistics

Number of solar cells tested

Yes
 No

Statistical analysis was performed on 10-20 devices of each architecture (Figure S33 - S39)

Statistical analysis of the device performance

Yes
 No

Figure S33 - S39

9. Long-term stability analysis

Type of analysis, bias conditions and environmental conditions

For instance: illumination type, temperature, atmosphere humidity, encapsulation method, preconditioning temperature

Yes
 No

Stability tests were performed under 1-sun illumination from a white LED and MPP-tracked conditions. Unencapsulated devices were tested in a nitrogen environment. Encapsulated devices were tested at 65 degrees Celsius in 50% relative humidity. (Figure 5 e,f, Methods - Stability testing)